Title

Exploring the hydromorphology of arctic river deltas for process understanding and for projecting their response to climate change

Author

Vulis, Lawrence

Publication Date

2023

UNIVERSITY OF CALIFORNIA,
IRVINE

Exploring the hydromorphology of arctic river deltas for process understanding and for projecting their response to climate change

DISSERTATION

submitted in partial satisfaction of the requirements
for the degree of

DOCTOR OF PHILOSOPHY

in Civil and Environmental Engineering

by

Lawrence M. Vulis

Dissertation Committee:
Professor Efi Foufoula-Georgiou, Chair
Professor Alejandro Tejedor
Doctor Joel C. Rowland
Professor Tirtha Banerjee
Professor James T. Randerson

2023

DEDICATION

To Aga, Basia, Szyszka, Marina, and Dimitri

TABLE OF CONTENTS

LIST OF FIGURES

LIST OF TABLES

ACKNOWLEDGMENTS

I would like to thank

Efi, who took me in as a young student and worked tirelessly to train me to think like a scientist, to question everything, to drill down into a problem, and to extract the most relevant parts. Your unwavering support through my time at UCI has formed me as a scientist, and your insight into problems will never cease to amaze me.

Alex, who has worked across three continents and four timezones to teach me how to ask the right questions, how to turn a pile of data into a comprehensible narrative, and how to communicate across disciplines. Your mentorship has been critical in this dissertation.

Joel, who took in a young engineering student interested in carving out an understanding of fascinating and remote landscapes and fundamentally helped to guide the research in this dissertation. I hope that our work together has made a dent in the scientific understanding of arctic river deltas.

the many collaborators I have had the honor of working with including Connor Broaddus, Jack Brown, Tian Dong, Doug Edmonds, Tryphon Georgiou, Clement Guilloteau, Jay Hariharan, Danny Kahl, Phong Le, Hongbo Ma, Antonios Mamalakis, Jaap Nienhuis, Irina Overeem, Anastasia Piliouras, Brett Sanders, Jon Schwenk, and Ilya Zaliapin.

friends made here in Irvine who are to numerous to name, including those from Efi's group past and present, from the communities we've collectively formed across the university, and in the neighborhoods we've lived in. The countless discussions, dinners, barbeques, celebrations, and memories we have together will be forever cherished. I would like to especially thank Clement, who has been a close friend and collaborator, who weathered long meetings and errant discussions, and has provided steadfast intellectual and emotional support through the dissertation.

the administrative support of Jerry, April, and Angie who kept things running while the research was done.

and finally, most importantly, my fiancee Aga, who has stood with me through this dissertation as it was conducted and written in innumerable apartments and trips. Your support, company, and love while here in Irvine has been fundamental to completing this dissertation. Thank you.

This dissertation was supported by funding from the University of California Lab Fees In-Residence Graduate Fellowship Grant L21GF3569, the NASA Earth and Space Science Fellowship Grant 80NSSC18K1409. the United Kingdom Research & Innovation Living Deltas Hub NES0089261, and the National Science Foundation through the Collaborative Research program Grant EAR1811909.

The text of chapter 2 in this dissertation is a reprint of the material adapted from "River delta

morphotypes emerge from multiscale characterization of shorelines." accepted for publication in Geophysical Research Letters, 2023, used with permission from Wiley. The co-authors listed in this publication are Alejandro Tejedor, Jaap H. Nienhuis, Hongbo Ma, Connor M. Broaddus, Jack C. Brown, Joel C. Rowland, and Efi Foufoula-Georgiou

The text of chapter 3 in this dissertation is a reprint of the material adapted from "Channel network control on seasonal lake area dynamics in arctic deltas." Geophysical Research Letters, 47, e2019GL086710, 2020, used with permission from Wiley. The co-authors listed in this publication are Alejandro Tejedor, Jon Schwenk, Anastasia Piliouras, Joel C. Rowland, and Efi Foufoula-Georgiou.

The text of chapter 4 in this dissertation is a reprint of the material adapted from "Climate signatures on lake and wetland size distributions in arctic deltas." Geophysical Research Letters, 48, e2021GL094437, 2021, used with permission from Wiley. The co-authors listed in this publication are Alejandro Tejedor, Ilya Zaliapin, Joel Rowland, Efi Foufoula-Georgiou.

The texts of chapter 5 in this dissertation are unpublished material used with the permission of co-authors Alejandro Tejedor, Joel C. Rowland, Ilya Zaliapin, and Efi Foufoula-Georgiou.

VITA

Lawrence M. Vulis

EDUCATION

Doctor of Philosophy in Civil and Environmental Engineering **2023**
University of California, Irvine *Irvine, CA*

Masters of Science in Civil Engineering **2018**
University of California, Irvine *Irvine, CA*

Bachelor of Engineering in Environmental Engineering **2017**
City College of New York *New York, NY*

RESEARCH EXPERIENCE

Graduate Research Fellow **2021–2023**
Los Alamos National Laboratory *Los Alamos, NM*

Graduate Research Assistant **2017–2023**
University of California, Irvine *Irvine, CA*

Research Intern **2016**
NOAA Earth Systems Research Laboratory *Boulder, CO*

Research Intern **2015**
NOAA National Ice Center *Suitland, MD*

Student Researcher **2014–2017**
Civil Engineering Dept., City College of New York *New York, NY*

PEER-REVIEWED PUBLICATIONS

PUBLISHED

7. Rowland, J. C., J. Schwenk, E. Shelef, J. Muss, D. Ahrens, S. Stauffer, A. Piliouras, B. Crosby, A. Chadwick, M. Douglas, P. Kemeny, M. Lamb, G. Li, and **L. Vulis**, Scale-dependent influence of permafrost on riverbank erosion rates, under review in *Journal of Geophysical Research: Earth Surface*, 2023.

6. **Vulis, L.**, A. Tejedor, H. Ma, J. Nienhuis, C. Broaddus, J. Brown, D. Edmonds, J. C. Rowland, and E. Foufoula-Georgiou, River delta morphotypes emerge from multiscale characterization of shorelines, accepted in *Geophysical Research Letters*, doi:10.1029/2022GL102684, 2023.

5. Broaddus, C., **L. M. Vulis**, J. H. Nienhuis, A. Tejedor, J. Brown, E. Foufoula-Georgiou, and D. A. Edmonds, First order controls on sediment balance determine delta morphology, *Geophysical Research Letters*, 49, e2022GL100355, doi:10.1029/2022GL100355, 2022.

4. Tejedor, A., J. Schwenk, M. Kleinhans, A. Limaye, **L. Vulis**, P. Carling, H. Kantz, E. Foufoula-Georgiou. The Entropic Braiding Index (eBI): a robust metric to account for the diversity of channel scales in multi-thread rivers, *Geophysical Research Letters*, 49, e2022GL099681, doi:10.1029/2022GL099681, 2022

3. **Vulis, L.**, A. Tejedor, I. Zaliapin, J. C. Rowland, and E. Foufoula-Georgiou, Lakes and wetlands in arctic deltas reveal distinct process controls and climate signatures, *Geophysical Research Letters*, 48, e2021GL094437, doi:10.1029/2021GL094437, 2021

2. Guilloteau, C., A. Mamalakis, **L. Vulis**, P. Le, T. T. Georgiou, E. Foufoula-Georgiou, Rotated spectral principal component analysis (rsPCA) for identifying dynamical modes of variability in climate systems, *Journal of Climate*, 34:2, 715 – 736, doi:10.1175/JCLI-D-20-0266.1, 2020.

1. **Vulis, L.**, A. Tejedor, J. Schwenk, A. Piliouras, J. C. Rowland, and E. Foufoula-Georgiou, Channel network control on seasonal lake area dynamics in arctic deltas, *Geophysical Research Letters*, 46, doi:10.1029/2019GL086710, 2020.

SOFTWARE

ROAM `https://github.com/lvulis/ROAM`

A fast R implementation of the Opening Angle Method (ROAM) for defining delta shorelines from optical imagery

ABSTRACT OF THE DISSERTATION

Exploring the hydromorphology of arctic river deltas for process understanding and for projecting their response to climate change

By

Lawrence M. Vulis

Doctor of Philosophy in Civil and Environmental Engineering

University of California, Irvine, 2023

Professor Efi Foufoula-Georgiou, Chair

River deltas are fascinating, ecogemorphologically complex landscapes at the river-coastal interface which are rich in biodiversity, are economic hotspots due to their major food production and ports, and are home to more than 340 million people, although composing only 0.57% of the global land surface. They are vulnerable to sea level rise, human actions from upstream, and increased erosion from more severe storm activity. Arctic river deltas are especially at high risk from climate change induced impacts, in part due to their unique permafrost features. In particular, thermokarst lakes, which are formed by the thaw of ice-rich permafrost, are expected to both expand and drain under future warming, reconfiguring deltaic hydrology and impacting the arctic carbon cycle. Yet studies focusing on thermokarst lake dynamics and trends in deltaic environments are limited.

In this dissertation we first place arctic river delta morphologic variability in a global context through a multiscale characterization of river delta shoreline structure (Chapter 2). Then, we interrogated thermokarst lake processes in arctic river deltas through analysis of summertime surface water dynamics to infer permafrost presence (Chapter 3), development of a methodology for the extraction of perennially inundated lakes from a long remote sensing record to explore relationships of thermokarst lake size distributions with climate (Chap-

ter 4), and characterization of thermokarst lake patterns towards inferring permafrost and geomorphic processes on arctic deltas (Chapter 5).

The results of this dissertation advance our understanding of the link between observed delta morphology and the dominant forcings which have formed deltas, provide the first quantitative framework for studying the spatial distribution of thermokarst lakes in terms of their size and location for delta comparison and for tracking their temporal changes, as well as for constraining and evaluating physics-based models. Some open questions are posed that require future study and targeted field observations to connect processes to their expression on the landscape and increase our confidence for future projections of the hydrogeomorphology of arctic deltas in response to global warming.

CHAPTER 1

Introduction

River deltas are ecogeomorphically critical landscapes that form the interface of rivers and standing waterbodies (Overeem et al., 2005). Their nutrient rich and fertile soils have contributed to deltas hosting up to 340 million people across the world (Edmonds et al., 2020). A number of global megacities and major entry ports are located on river deltas, e.g. the Hanoi on the Hong, Shanghai on the Yangtze, New Orleans on the Mississippi, Bangkok on the Chao Phraya, Vancouver on the Fraser, and the majority of the nation of Bangladesh lies on the Ganges Brahmaputra delta. The complex distributary channel networks of deltas are biogeochemical reactors which modulate the pathways of nutrients such as nitrogen, phosphorous, and carbon to coastal waters (Knights et al., 2020) which has ramifications for coastal ecosystems (Lique et al., 2016). The combined direct economic revenue and ecosystem services of major rivers deltas was estimated in 2015 to be in the trillions of US dollars per annum (Giosan et al., 2014). This economic and environmental importance motivates the need to understand physical processes which influence delta dynamics and the environmental risks facing deltas.

Deltas are fundamentally highly dynamic landscapes which naturally construct and lose land due to a combination of fluvial and marine processes (Passalacqua et al., 2021). Riverine deposition drives delta growth through channel-building while waves rework sediment via longshore transport parallel to the coast and tides construct and widen channels via bidirectional flow (Galloway, 1975). The interaction of riverine, wave, and tidal forcings and the multiple spatio-temporal scales at which they operate result in the stunning degree of variability in delta morphology seen globally (Bhattacharya & Giosan, 2003; Fagherazzi et al., 2015; Hoitink et al., 2017; Jerolmack & Swenson, 2007; Konkol et al., 2022; Perignon et al., 2020; Tejedor et al., 2016, 2017). Yet a robust quantitative framework to relate delta morphology to the relative influence of rivers, waves, and tides does not yet exist, hampering our ability to make projections of delta morphology under future changes in these forcings arising from sea level rise (Nienhuis et al., 2023), riverine discharge and sediment load changes (Overeem & Syvitski, 2010; Stadnyk et al., 2021), increased coastal storm activity (Emanuel, 2013), and direct anthropogenic modification (Hackney et al., 2020; Xu et al., 2019).

In the Arctic, river deltas are influenced not only by rivers, waves, and tides but by periglacial processes such as river ice formation which leads to river ice break up and erosion (Prowse et al., 2011), sea ice induced decrease in wind-fetch and therefore coastal erosion (Barnhart et al., 2014), permafrost-induced soil cohesion (Woo, 2012), and thermokarst (i.e. thaw lake) formation (French, 2017; Grosse et al., 2013). Of particular interest are thermokarst lakes which are formed by the thaw of ice-rich permafrost and supported by further hydraulically impermeable permafrost beneath and around them. A warming arctic is expected to lead to lake cover change, although satellite observations of thermokarst lakes over the remote sensing record have recorded both increasing and decreasing trends in lake cover depending on local geology, temperature, hydrology, and permafrost zonation (Arp et al., 2011; Chen et al., 2012; Jones et al., 2011; Nitze et al., 2018; Plug et al., 2008; Smith et al., 2005). Moreover, the dynamics of thermokarst lakes within the context of the complex distributary channel networks on the delta planform are not well understood. As these lakes act as sediment and nutrient reservoirs, influencing the delivery of riverine material to the arctic ocean and both atmospheric and aquatic carbon cycling (Cunada et al., 2021; Emmerton et al., 2007; Squires et al., 2009), it is critical to understand thermokarst lake processes on deltas to inform projections of future lake cover change.

This dissertation advances the understanding of the link between form and process on global and arctic river deltas through (1) development of quantitative morphologic classification of river deltas through multiscale characterization of their shorelines, (2) analysis of summertime surface water dynamics to infer permafrost presence on arctic deltas, (3) developing a methodology for extraction of thermally relevant lakes from a long remote sensing record to explore relationships of thermokarst lake size distributions to climate, and (4) characterization of thermokarst lake patterns towards inferring permafrost and geomorphic processes on arctic deltas.

In Chapter 2, we analyze river deltas through the lens of their shorelines. Delta shoreline morphology has long been hypothesized to encode information on the relative influence of fluvial, wave, and tidal forcings on delta formation and evolution. However, rigorous quantification of delta morphology and how it relates to forcing is still lacking. We introduce a new multiscale geometric framework which characterizes river delta morphology via measures of its shoreline structure, and use these measures to separate deltas into morphological classes (called morphotypes) and to infer the dominant forcing of each morphotype. We then show that the dominant forcings inferred from shoreline structure generally align with those estimated via relative sediment fluxes, while positing that misalignments arise from spatiotemporal heterogeneity in deltaic sediment fluxes not captured in the flux estimates.

In Chapter 3, we analyze summertime waterbody dynamics on arctic deltas in order to understand the spatial distribution of permafrost. We hypothesize that summertime waterbody shrinkage rates on arctic deltas are controlled by proximity to the delta channel network due to a spatially explicit pattern in active layer thickness and near surface hydrologic connectivity. We document such a pattern in two Alaskan deltas using 27 summers of remote sensing imagery from Landsat and evaluate alternative drivers of this pattern including sub-pixel resolution channels which would result in spurious high waterbody shrinkage closer to the channel network and systematically shallower waterbodies closer to the channel network. We find that a thicker and deeper active layer is the most likely explanation for the observed lake shrinkage pattern and suggest the potential of investigating waterbody dynamics, from readily available satellite data, for inferring permafrost patterns which are hard to measure directly over large spatial domains.

In Chapter 4, we characterize thermokarst lake size distributions and their relationship to climate. The significant interannual hydrologic variability of arctic deltas hampers inference on the spatial variability of lake cover, in particular when considering the short summertime window of optical spaceborne observations available for monitoring lake dynamics. We present a pan-Arctic study of 12 arctic deltas wherein we classify observed waterbodies into perennial lakes and ephemeral wetlands capitalizing on the historical record of remote sensing data. We provide evidence that thermokarst lake sizes are universally lognormally distributed and that historical temperature trends are encoded in lake sizes, while wetland sizes are power law distributed and have no temperature trend.

In Chapter 5, we use the lake dataset generated in Chapter 4 to analyze lake spatial patterns on arctic deltas to mine information on permafrost and geomorphic processes. We introduce a suite of information theoretic measures to characterize lake spatial distribution and lake cover, and utilizing these along with traditional measures we document a weak relationship between lake spatial coverage and climate. We then show that lake patterns are spatially structured on all deltas and that surface hydrologic connectivity between lakes is spatially variable within and across deltas, positing that such patterns reflect geomorphic process differences that can be explored for process understanding. For example, combining these analyses with higher resolution satellite imagery and field data may improve estimates of spatially distributed permafrost cover and inform our understanding of permafrost development in deltaic environments, which is important for carbon and nutrient cycling under a changing climate.

In Chapter 6, we present concluding remarks and perspectives for future research in temperate and arctic deltas.

The above chapters are presented in stand-alone format based on peer-reviewed published articles or manuscripts under consideration in scientific journals. Collaborative research that contributed significantly to the ideas, analyses, and results presented in this dissertation includes analysis of numerically simulated deltas to link sediment flux budget and delta morphology, development of a process-based effective resolution of channel network topology and geometry, and analysis of the controls on the progradation of delta channel network tips.

CHAPTER 2

River delta morphotypes emerge from multi-scale characterization of shorelines

2.1 Introduction

River deltas are complex ecogeomorphic landscapes which are home to upwards of 300 million people due to their fertile soils and rich ecosystems (Edmonds et al., 2020). Their intricate hydromorphology controls nearshore biogeochemical function (Knights et al., 2020; Zoccarato et al., 2019), connectivity between surface and subsurface hydrogeology and reservoirs (Sawyer et al., 2015), coastal resilience (Hoitink et al., 2020; Tognin et al., 2021), and ecosystem services (Adams et al., 2018). Deltas are particularly vulnerable to climate change due to their low relief, coastal proximity, and large populations (Edmonds et al., 2020; Hoitink et al., 2020). It is therefore critical to understand how sea level rise and changing riverine sediment loads will impact these systems (Chadwick et al., 2020; Nienhuis et al., 2023) and towards this goal, developing a quantitative framework which links the driving forces forming deltas to delta morphology and function is imperative. Fifty years ago, Galloway (1975) introduced the paradigm that river deltas are shaped by the interplay of progradational riverine forcings and erosional marine (wave and tide) forcings, which has steered subsequent research on river delta evolution (e.g., Ainsworth et al., 2011; Anthony, 2015; Bhattacharya & Giosan, 2003; Nienhuis et al., 2020; Seybold et al., 2007). The relative balance of these forcings and the multiple spatio-temporal scales at which they operate result

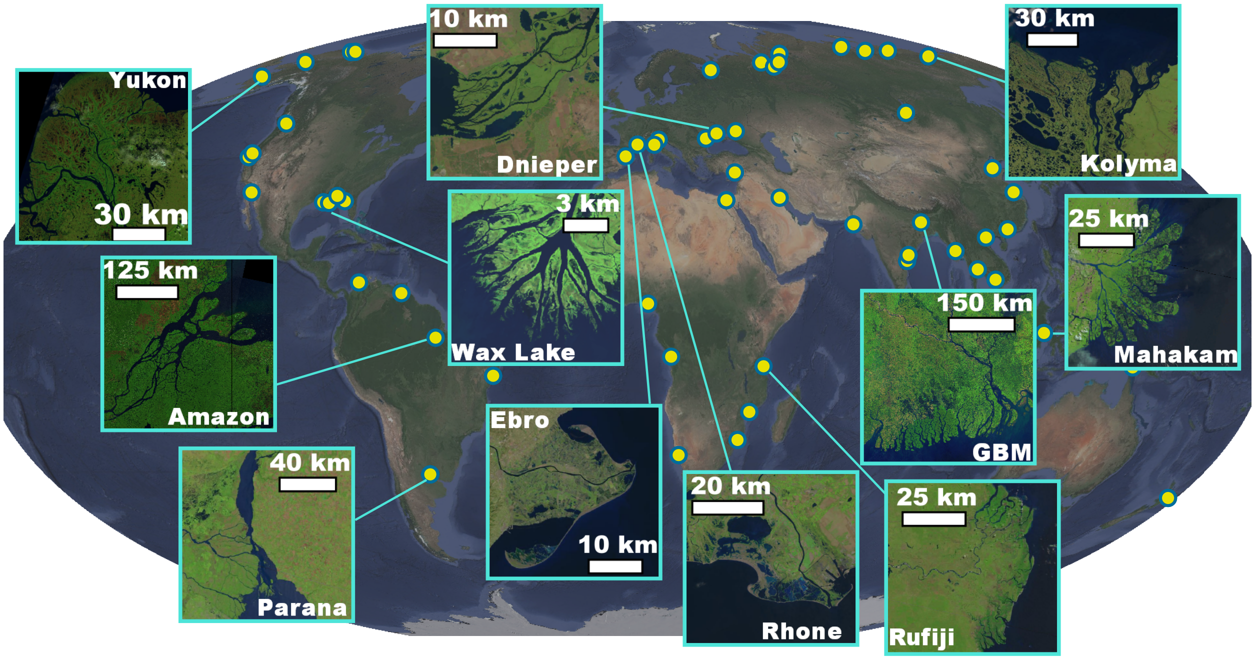

Figure 2.1: **The morphologic variability of Earth's deltas.** River deltas show differences in shoreline structure attributed to the relative balance of river, wave, and tidal sediment fluxes Galloway (1975). Yellow dots show locations of a globally distributed sample of 54 deltas analyzed in this study. Satellite imagery courtesy of Landsat and Google Earth.

in a stunning degree of variability in shoreline structure and channel network geometry and topology (Fagherazzi et al., 2015; Hoitink et al., 2017; Jerolmack & Swenson, 2007; Konkol et al., 2022; Tejedor et al., 2016, 2017). Rivers act to prograde the delta planform at the large scale and increase roughness at fine scales via the growth of mouth bars and distributary channel expansion (Fagherazzi et al., 2015; Wolinsky et al., 2010). Waves generate alongshore transport that diffuse sediment along the shoreline at fine scales but can lead to spits at coarser scales (Ashton & Giosan, 2011) and suppress mouth-bar development (Jerolmack & Swenson, 2007). Tidal forces widen distributary channels and construct headless channels which lack connections to the upstream river, roughening the shoreline at multiple scales (Hoitink et al., 2017; Nienhuis et al., 2018). Recently, the relative magnitudes of the forcings in the Galloway framework have been quantified via a sediment flux approach (Nienhuis et al., 2020). However, shoreline shape, a crucial ingredient in the qualitative morphological classification originally posed by Galloway (See Table 2 in Galloway (1975)), has not been quantified in a way to be able to bear out significant differences between visually distinct deltas, nor has been shown to have a clear relationship with forcings, e.g. (Baumgardner, 2015). This is in part because analysis of shoreline structure has typically focused on a single length scale using metrics such as shoreline variability (Straub et al., 2015), roughness or rugosity measures (Baumgardner, 2015; Caldwell & Edmonds, 2014; Geleynse et al., 2012), and shape factors (Lauzon et al., 2019; Wolinsky et al., 2010). Such metrics do not necessarily measure shoreline structure at process length scales, neither do they capture the multiscale variability caused by the interplay of the three driving forces. Here, we propose a process-informed multiscale set of river delta shoreline metrics which combine geometric and spectral measures to develop a quantitative classification of delta morphology. Our approach utilizes localized analysis of shoreline structure both in space and wavenumber domains in order to isolate features corresponding to different processes acting at multiple scales. Unsupervised clustering of the shoreline morphometrics identifies 5 classes of morphologically similar deltas, i.e. delta morphotypes. Based on the values of the process-targeted metrics, dominant forcings are attributed to each morphotype, which we then show to generally align with the dominant forcings quantitatively estimated by their relative sediment fluxes (Appendix: A; Nienhuis et al. (2020)). We hypothesize that misalignments between the two are due to spatiotemporal heterogeneity in the sediment fluxes which are not captured by their estimated values. The novel delta morphology classification and comparison to sediment fluxes informs our understanding of how the form and function of these densely populated and biogeochemically rich landscapes might respond to projected changes in sediment fluxes, relative sea level rise, and anthropogenic modification (Chadwick et al., 2020; Edmonds et al., 2020; Hariharan et al., 2022; Hoitink et al., 2020; Moodie & Nittrouer, 2021; Nienhuis et al., 2020; Syvitski & Saito, 2007). It also offers potential application in inferring paleoclimate from ancient delta deposits and interpreting extraterrestrial delta morphology.

2.2 Multiscale Characterization of Delta Shorelines

We analyzed the shorelines of 54 global river deltas across a representative range of sizes and morphologic variability, including systems with wave-influenced, river-influenced, and tide-influenced features (see Appendix A; Figure 2.1; Syvitski & Saito (2007)). River delta shorelines were defined using the Opening Angle Method (OAM) with a critical angle of 45° (Shaw et al., 2008). To define a shoreline, the OAM requires a binary water mask, which was obtained by thresholding water occurrence masks from the Landsat-derived, 30-m spatial resolution Global Surface Water dataset (Pekel et al., 2016). We defined three scales at which delta shoreline structure exhibits variability which are linked to the balance of river, tide, and wave forcings: a macroscale (overall delta planform), mesoscale (mouth width scale), and microscale (beach scale). We developed metrics to capture the variability at those scales as discussed below. At the macroscale, riverine sediment deposition leads to delta progradation and growth into the receiving basin and generates extrusional shapes (i.e. convex shoreline; Caldwell & Edmonds (2014); Galloway (1975)). When wave-driven alongshore transport removes the majority of riverine sediment flux, the delta has no protrusion, and is linear (i.e. mostly flat shoreline; Nienhuis et al. (2018)). Lastly, tidal forcings erode subaerial sediment into the nearshore and construct a subaqueous shoal (Hoitink et al., 2017). This net erosion from land leads to a funnel-shaped, concave subaerial delta, or estuary, which intrudes into the surrounding landscape (i.e. a concave shoreline). We therefore measured the curvature of the entire shoreline (Figure 2.2; Jammalamadaka & Sengupta (2001)), to classify deltas as convex (extrusional), concave (intrusional), or flat (see Appendix A).

At the mesoscale, the influence of rivers, waves, and tides on channel mouths dictates multiple intermediate scales of variability on the shoreline. Tidal forces widen mouths exponentially (Nienhuis et al., 2018) which leads to multiscale undulations in the shoreline, for example on the Amazon or Indus deltas. Rivers form mouth bars and bifurcations lead-

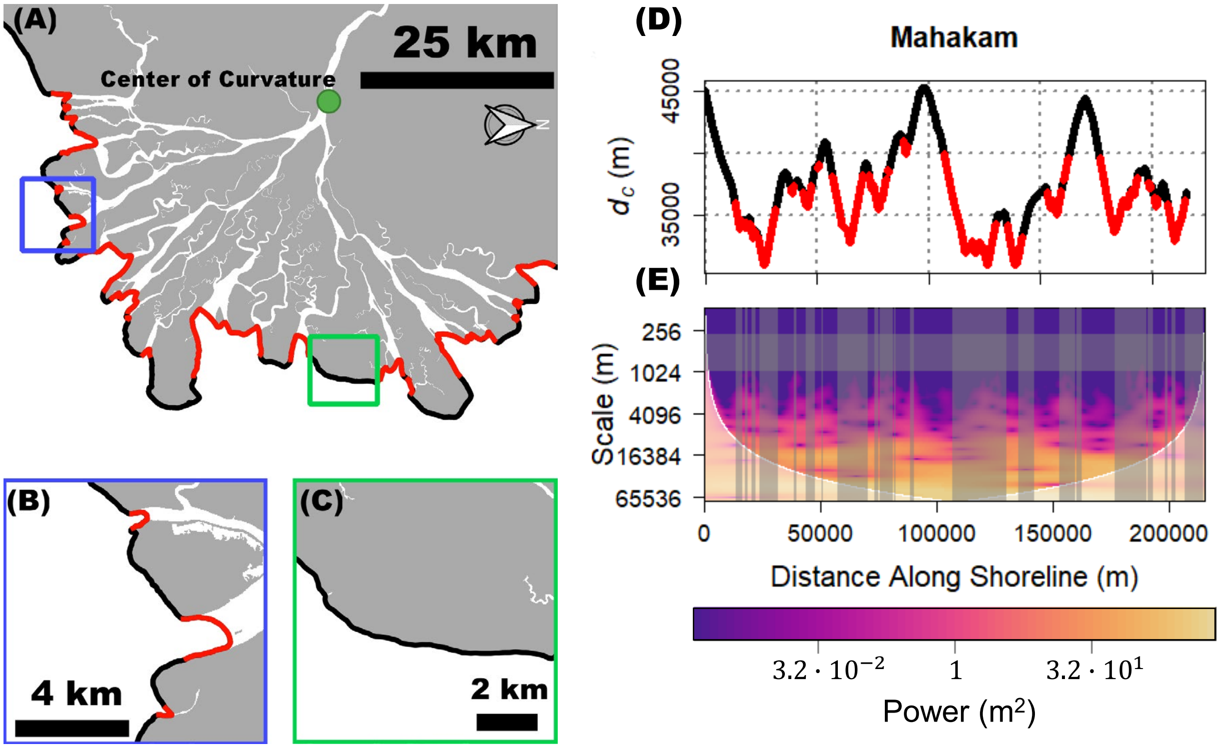

Figure 2.2: **Example of the multiscale features of shoreline structure on the Mahakam Delta, Indonesia.** The shoreline of the delta, defined using the Opening Angle Method (OAM) with a critical angle of 45°, shows multiple scales of variability. At the macroscale, a delta may be convex due to river deposition, flat due to wave-driven along shore transport, or concave due to tidal widening and estuarine conditions. This is measured here by the ratio between the radius of curvature and the length of the shoreline. (B) Mouths formed by rivers and tides lead to undulations in the shoreline at a scale determined by the relative river and tide fluxes. (C) At the microscale, waves diffuse sediment parallel to the coast and smooth the shoreline, while rivers and tides roughen it. (D) To measure meso- and microscale variability, the $2D$ shorelines are mapped to a univariate signal defined as the distance from each point along the shoreline to the center of curvature, $d_c(s)$, where s is the distance along the shoreline. (E) The wavelet transform is used to estimate the fraction of variance contributed by the mouths, fM, marked in red in the preceding panels, and the Gini-corrected Finescale Variance $gFSV$, i.e. the variance from scales (wavelengths) between 300 to 1000 m.

ing to small but numerous mouths which result in intermediate to fine scale undulations in the shoreline, for example in the Dnieper delta. Lastly, wave-driven sediment transport prevents mouth bar formation (Jerolmack & Swenson, 2007) and reduces the number of channels (Broaddus et al., n.d.), resulting in long shorelines with few, small undulations, for example in the Ebro delta. To measure the contribution of mouths to the overall variability of the shoreline structure, we first projected the shoreline into a univariate spatial-series by recording the distance from each point along the shoreline to the center of curvature of the macroscale shape of the delta. Then, we identified sections of the shoreline spatial-series corresponding to the mouths and measured via localized wavelet transforms (Kumar & Foufoula-Georgiou, 1994) the fraction of variance contributed by the mouths, fM (Appendix A; Figure 2.2).

Finally, at the microscale, wave-driven alongshore transport diffuses sediment along the coast and smooths shorelines (Ashton et al., 2001), while rivers and tides introduce variability from distributary and headless channels (Wolinsky et al., 2010). Therefore, we measured the fine scale variance (FSV), as the variance at wavelengths of 300 to $1,000$ m, to capture these differences (Figure 2.2). The lower bound is the result of the minimum reliable scale above which discretization, aliasing, and smoothing effects do not affect the spectra, while the upper bound is an approximation of the range of scales within which waves act to smooth shorelines and below which large scale features such as spits begin to emerge. The results are robust to shifting the upper bound from 800 to $1,100$ m (Appendix A). Furthermore, in order to separate shorelines that may have equal fine scale variance but relatively more power at larger wavelengths compared with shorelines that have relatively less power at those wavelengths, the FSV is adjusted by the degree of heterogeneity over the spectral range by multiplying by a spectral Gini coefficient, g, defining the $gFSV$. The spectral Gini coefficient is a measure of the deviation of the spectra from white noise, i.e. a random signal with a flat spectrum (Appendix A). With these three metrics we are able to quantitatively compare the shoreline morphology of river deltas and explore the possible emergence of distinct morphotypes.

2.3 Shoreline Morphometric Space

The proposed shoreline metrics construct a three-dimensional Shoreline Morphometric Space (**SMS**) within which deltas can be positioned and compared (Figure 2.3). To objectively and robustly identify clusters that categorically classify deltas within this space, we used an unsupervised machine learning algorithm, k-prototypes (a modification of k-means clustering that accounts for categorical predictors such as the macroscale shape; Huang (1998)). Five morphotypes, i.e., clusters of morphologically similar deltas, self-emerge from the three-dimensional SMS (Figure 2.3) and are displayed in Figure 2.4. Note that the identified clusters are robust and stable as found by randomly resampling 80% of the deltas and repeating the clustering procedure, obtaining an identical grouping of delta morphologies in 97% of simulations.

The first morphotype is denoted as the "tidal morphotype" as it contains concave and flat systems with mouth-dominated shorelines and low finescale variance, indicative of tide-domination (Figure 2.4), for example, the Fly and Amazon deltas. It also includes valley-confined systems like the Ob and Yenisei due to their wide mouths. The second morphotype is denoted as the "river morphotype" as it contains systems characterized by an intermediate fraction of variance contributed by mouths, are rough at fine scales, and have a convex planform, for example, the Selenga and Mississippi deltas. Valley-confined deltas such as the Dnieper and Don, which are concave and flat but have high fine scale variability, are also included as part of the river morphotype. The third morphotype is denoted as the "wave morphotype" as it contains systems which are flat, lacking a subaerial protrusion formed by river deposition, and smooth at fine scales, for example, the Eel and Orange deltas. The fourth morphotype is denoted as the "river-wave morphotype" as it contains

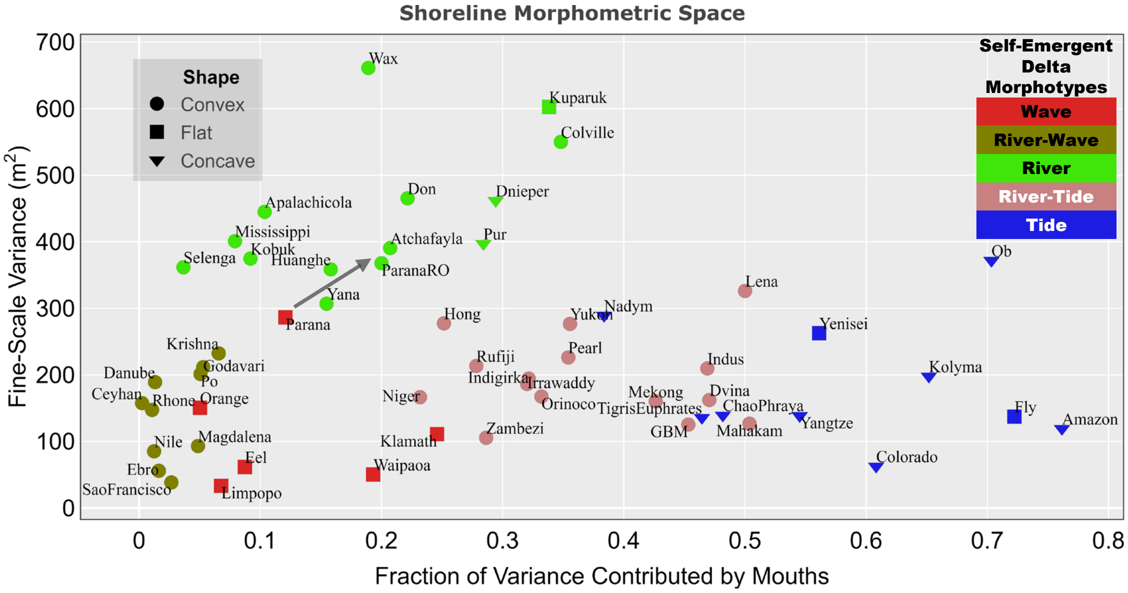

Figure 2.3: **The Shoreline Morphometric Space (SMS).** Deltas shorelines are positioned in the three-dimensional space constructed by the macroscale shape, fM, and $gFSV$ metrics. Unsupervised clustering of the SMS using k-protoypes reveals five self-emergent delta morphotypes, i.e. classes of morphologically similar systems. The relative position of the deltas in the SMS elucidates the dominant forcing acting on each morphotype, e.g increased fM a signature of greater tidal influence. The classified deltas are shown in Figure 2.4. The arrow indicates the shift in the SMS position of the river distributary section of the Parana shoreline (ParanaRO) compared with the shoreline of the entire Parana, see text for details.

systems which are convex, smooth at fine scales, typically have spits or flying spits, and little to no variability contributed by mouths, for example, the Ebro and Rhone deltas. Lastly, the fifth morphotype is denoted as the “river-tide morphotype” as it contains convex deltas with tidally widened mouths and headless channels, resulting in intermediate variability contributed by mouths, for example, the Mahakam and Orinoco deltas.

The dominant forcings determined by the quantitative classification of shorelines correspond with expert assessment of the dominant forcings based on qualitative comparisons of delta morphology (Ainsworth et al., 2011; Nienhuis et al., 2020) suggesting that shoreline structure carries a distinct signature of the processes that generated that delta. An interesting further step is to check whether the inferred dominant forcings align with the relative sediment fluxes driven by each forcing, for which we use the recently developed sediment flux estimation framework of Nienhuis et al. (2020).

2.4 Are Delta Morphotypes Aligned With Relative Sediment Fluxes?

Each of the 54 deltas was projected onto the ternary Galloway diagram according to the relative sediment flux transported by rivers, waves, and tides as estimated in Nienhuis et al. (2020)(Figure 2.5). Before contrasting delta morphotypes with their relative sediment fluxes we note a few important issues which we anticipate to cause discrepancies in the mapping between the morphotype and dominant sediment flux. First, the marine sediment fluxes are estimated using simplified, although nonlinear, physical models which transform tidal amplitudes and offshore wave-climate into tidal and wave sediment fluxes, respectively. Therefore, any uncertainty in the tidal amplitude and wave climate will propagate into uncertainty in the sediment flux estimate. Second, sediment fluxes are estimated using single, represen-

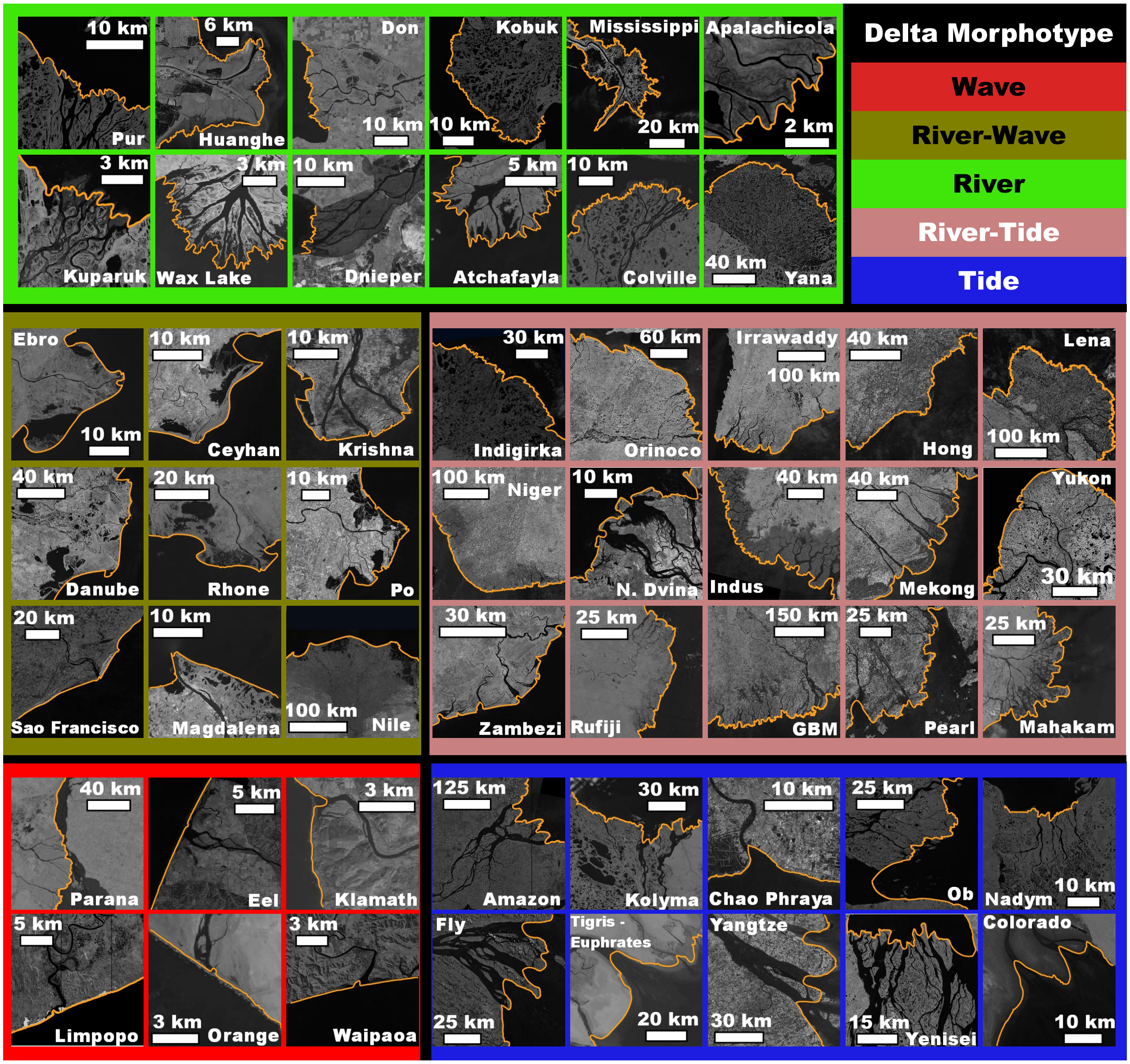

Figure 2.4: **Deltaic morphotypes identified from the SMS**. The deltas corresponding to the five morphotypes which emerged from the SMS (Figure 2.3). Shorelines are shown in orange with underlying imagery from Landsat or Google Earth.

tative locations for wave climate, tidal amplitude, and fluvial discharge, not acknowledging possible multi-mouth or multi-lobe structure (Nienhuis et al., 2020). Moreover the sediment fluxes are estimated using contemporary wave climate, tidal amplitude measurements, and modelled, pre-anthropogenically-influenced riverine discharge and sediment loads (Appendix A; Nienhuis et al. (2020)), and represent snapshots of the relative sediment flux, while delta morphology represents the temporally integrated effect of the forcings acting on the delta (Syvitski et al., 2022). Accordingly, any significant spatiotemporal heterogeneity or non-stationarity in the fluxes over each delta's evolution might not be reflected in the contemporary sediment flux estimates. Therefore, some misalignments between delta morphotype and dominant sediment flux are expected, hoping however, that a general agreement will emerge. The delta morphotypes are found to generally have relative sediment fluxes in line with the dominant forcings expressed in their shoreline structure (Figure 2.5). For example, the river morphotype and wave morphotype deltas lie in the right corners of the Galloway diagram, and the river-wave morphotype deltas span the space in-between these two end member classes with varying degree of relative tidal influence. However, it is noted that this partitioning does not correspond to a simple ternary dissection of the Galloway space where deltas with a single forcing contributing more than 50% of the total sediment flux align with a morphotype dominated by that forcing. Rather, deltas in the river morphotype typically have relative river sediment flux in excess of 80%, although there are notable outliers. A similar observation is made for deltas in the wave morphotype. Morphological expression of dominance by a single forcing is therefore limited only to small corners of the Galloway space.

Of interest are the morphologically similar deltas which appear scattered or as misalignments between shoreline-inferred dominant forcing and dominant relative sediment flux in the Galloway diagram, as these yield valuable insight into the relationship between observed shoreline structure and the relative sediment fluxes. As discussed before, some outliers arise due to the uncertainty in the sediment fluxes. For example, deltas in the tidal morphotype

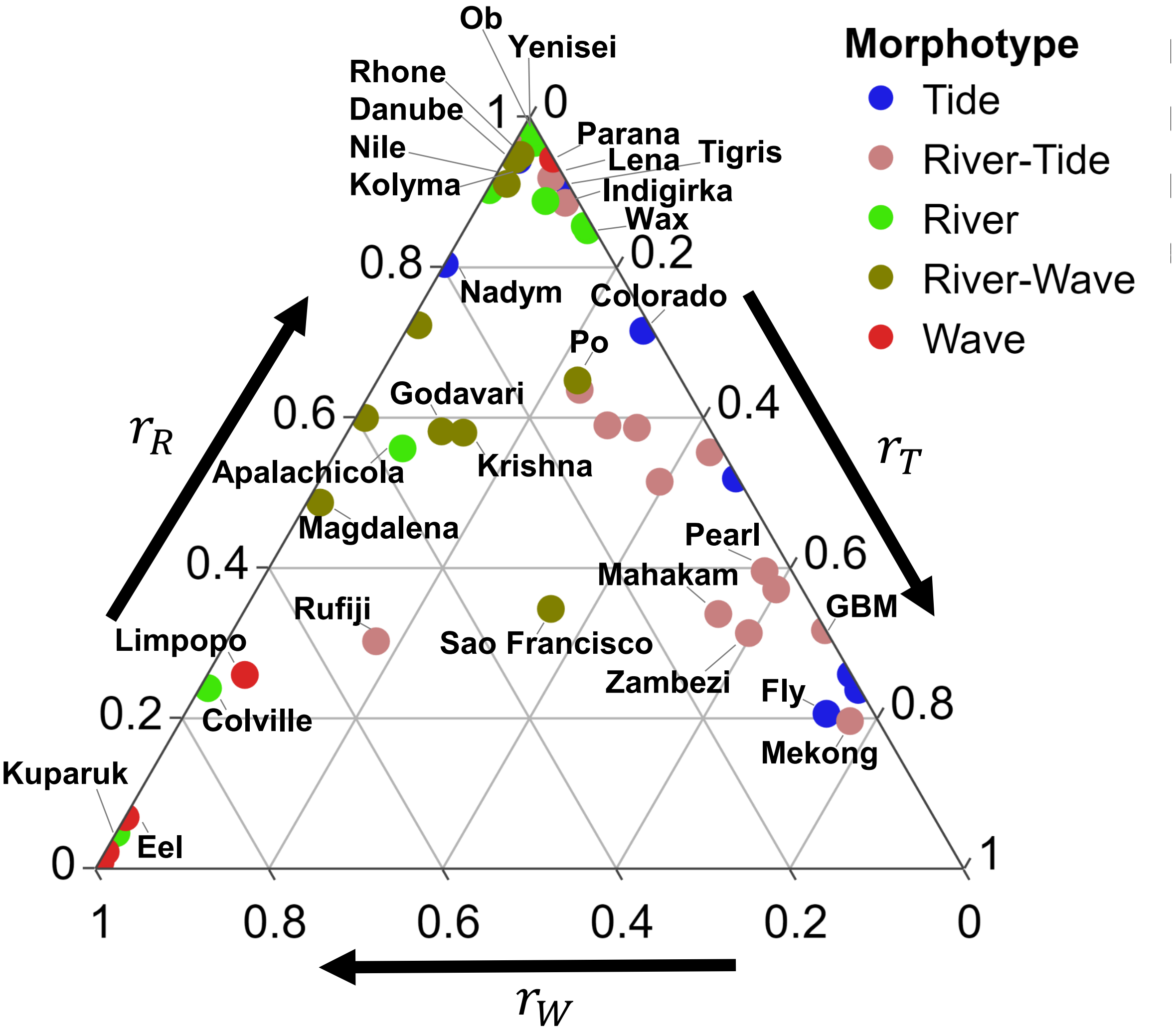

Figure 2.5: **Comparison of delta morphotypes to sediment flux budget.** The 54 deltas are positioned in the Galloway diagram using their relative sediment flux and colored by their morphotype emergent from the shoreline morphometric space (Figure 2.3). Delta morphotypes tend to fall in contiguous regions of the Galloway space which are outlined with dashed lines. Misalignments highlight spatiotemporal heterogeneity in the relative sediment fluxes not captured by their contemporary estimates Nienhuis et al. (2020).

such as the Kolyma and Tigris-Euphrates have relatively low tidal sediment fluxes, despite displaying clear tidal widening. We suspect that this results from under-estimation of the tidal sediment fluxes for these deltas. Similarly, river morphotype deltas such as the Colville, Kuparuk, and Apalachicola, are characterized by abundant mouthbars but have high estimated wave sediment fluxes which are expected to inhibit mouthbar formation (Jerolmack & Swenson, 2007). The Kuparuk and Apalachicola are associated with valley-confined or sheltered shorelines where wave climate data may be particularly uncertain. These misalignments highlight that the shoreline morphometric approach may be more robust than the sediment flux approach for delta classification as it is less sensitive to its defining parameters (e.g. critical angle or range considered for fine scales; see Appendix A).

Further misalignments of interest are the river-tide morphotype deltas and tide morphotype deltas which are scattered across a range of relative tidal influence. This mixture arises as the river-tide and tide morphotypes consist of deltas with intermediate to high fraction of variance contributed by mouths (**fM**) due to headless and wide channels. However, the river-tide morphotype consists solely of deltas that are convex at the macroscale, e.g. the Irrawaddy, Indus, and Mahakam, which is a signature of historical progradation of the delta planform due to fluvial deposition. Also deltas such as the Zambezi and Rufiji are convex with wide headless channels and have abundant tidal mangroves (Anthony et al., 2021; Erftemeijer & Hamerlynck, 2005), suggesting historical significant river and tidal influence, but have otherwise smooth, sandy shorelines and translating spits indicating recent wave influence. This suggests that although these systems at present have large relative tidal sediment fluxes, the estimated relative sediment fluxes do not capture the historical river dominance which constructed them. Thus, as tides widen and preserve former distributary channels (Hoitink et al., 2017), and the timescale for waves to erase the convex depositional system formed by river progradation could be on the order of centuries (Nienhuis et al., 2016), the signature of a river remains on its delta long after it has stopped flowing. Therefore, careful consideration must be given to possible temporal heterogeneities in each of the sediment fluxes when computing their relative values and assessing the alignment between morphotype and relative sediment flux (Syvitski et al., 2022). This is especially critical for characterizing morphologic response to sediment flux changes, e.g., decreasing riverine sediment delivery or changes in wave climate, and for projecting delta futures under climate change.

Lastly, we hypothesize that some of the misalignments arise because the morphologic metrics are computed along the length of the entire shoreline, although the sediment fluxes are computed via point estimates and don't convey information on spatial heterogeneity in the forcings acting on the delta. For example, the Parana delta lies in the wave morphotype although it has a complex distributary network in its southern half and is dominated by riverine sediment flux (Figures. 2.3,2.4,2.5). However, the Parana's depositional environment is unique as the Uruguay river runs parallel to its northern shore (Milana & Kröhling, 2015), which we posit acts as a longshore current that smoothens the shoreface but is not captured by the global sediment flux estimation framework which only includes wind-driven longshore transport. To test this hypothesis, we computed the three multiscale metrics of shoreline structure only on the section of the shoreline between the active distributaries in the southern section, terming it ParanaRO, and found that the ParanaRO indeed lies in the river morphotype (Figure 2.3), in agreement with its dominant riverine sediment flux (Figure 2.5).

Note that the defined framework to characterized shoreline structure allows us to further explicitly interrogate explicitly spatial variability in shoreline structure, e.g. may arise from marine reworking of abandoned distributary lobes following channel avulsion. Investigation into deltas with lobes of distinct morphology may lead to separation of these deltas within the SMS and could shed further light on the alignment between sediment flux and morphotype. However, the framework for estimating sediment fluxes (Nienhuis et al., 2020) will likely need to be adjusted to account for highly spatially variable sediment fluxes given multi-lobe or multi-mouth structures or variable wave climate (Syvitski et al., 2022). We note that combining shoreline metrics with metrics of network complexity (Konkol et al., 2022; Tejedor et al., 2015a,b, 2016, 2017) may help to separate deltas further within the SMS and identify subnetworks that need to be treated separately in terms of their morphology and sediment fluxes. In particular, network information may disaggregate the relatively large river-tide morphotypes and the tide morphotypes, with a possible separation of the valley-confined Ob and Yenisei deltas from estuarine systems such as the Kolyma, Ganges Brahmaputra, and Colorado. This further sub-division of deltas may also be able to yield insight into the influence of other controls on delta morphology including grain size (Caldwell & Edmonds, 2014), valley confinement, cold region processes, or sea level history (Nienhuis et al., 2023; Overeem et al., 2022). Interestingly, no systematic signature of near-shore sea-ice, permafrost, or river-ice was detected on shoreline structure (Lauzon et al., 2019; Overeem et al., 2022; Piliouras et al., 2021), except for a lack of wave influenced arctic systems which may relate to the short wind fetch present due to sea ice (Barnhart et al., 2014) or the presence of a shallow subaqueous ramp dampening wave runup and breakup at the subaerial shoreline (Overeem et al., 2022).

2.5 Conclusions

We have introduced a novel quantitative framework to classify river delta morphology based on a multiscale characterization of delta shoreline structure through geometric and spectral metrics which form a three-dimensional shoreline morphometric space (SMS). Unsupervised classification of 54 deltas projected in the SMS reveals self-emergent morphologically similar deltas, i.e. delta morphotypes which are further associated with dominant forcings based on the metrics. We then found that dominant forcings inferred from shoreline structure generally align with the dominant forcings quantitatively estimated by their relative sediment fluxes. We posit that misalignments arise due to possible spatiotemporal variability in the dominant forcings not captured in the relative sediment fluxes, providing a basis for more detailed analysis of those deltas. The proposed shoreline morphologic classification framework relies on readily available satellite imagery making it easily applicable for remote, poorly instrumented coastlines and basins as well as on extraterrestrial bodies, for which forcings are not available.

CHAPTER 3

Channel Network Control on Seasonal Lake Area Dynamics in Arctic Deltas

3.1 Introduction

Lakes play a key role in the hydrologic and biogeochemical cycles of arctic deltas, serving as hotspots of methane and carbon dioxide emissions (Squires et al., 2009; Tank et al., 2009). Thus, understanding lake response to permafrost thaw and constraining lacustrine emission estimates is critical for forecasting trajectories of the polar north (Elder et al., 2018; Wik et al., 2016) as arctic deltas alone are estimated to contain 90 ± 37 Pg-Carbon (Schuur et al., 2015), compared with 860 Pg-Carbon in the atmosphere (Le Quéré et al., 2018). Annual methane emissions from lakes have been estimated using a nonlinear dependence on lake area, typically computed using mean annual lake area (Bastviken et al., 2004). However, remote sensing studies of arctic lake area dynamics across various geomorphic settings and on seasonal to annual time scales have found seasonally variable lake area extent depending on proximity to river source, lake morphometry, and underlying permafrost content (Chen et al., 2012, 2013; Jepsen et al., 2013; Rey et al., 2019; Rover et al., 2012; Smith et al., 2005). For example, Cooley et al. (2019) found that in 2017 on the Mackenzie Delta, lake areas had decreased from their June maximum by $8 - 12\%$ in August. This temporal variability contributes to uncertainty in the arctic carbon budget, especially given the nonlinear dependence of methane emissions on lake area. Lake and wetland coverage also modulate surface albedo, therefore understanding variable water extent is key for modeling the land surface energy budget of the Arctic (Vonk et al., 2015). In addition, long-term trends of lake area extent over the past several decades are highly spatially heterogeneous, and seasonal variability in lake sizes is of the same order of magnitude as observed decadal trends (Chen et al., 2013), indicating the need to understand seasonal heterogeneity for trend quantification and uncertainty reduction of energy and carbon budgets.

Physical drivers of spatial variability in lake area dynamics include depth to permafrost, as the negligible hydraulic conductivity of frozen soil limits groundwater flow, inhibiting hydrologic connectivity between lakes and their surroundings (Walvoord & Kurylyk, 2016). For example, remote sensing studies on the Yukon Flats floodplains found that thicker active layers and associated near-surface (i.e., shallow) hydrologic connectivity were linked with higher rates of lake area loss and interannual variability in lake area for some lakes closer to the channels, compared with lakes surrounded by shallow permafrost farther from the channels (Rey et al., 2019). Furthermore, field observations on the Colville Delta, Yukon-Kuskokwim Delta, and other arctic floodplains have found that the river network imposes a pattern on the permafrost and vegetation distribution on the delta through repeated flooding and inundation of the areas closer to channels, leading to a thicker active layer (Viereck, 1973; Zheng et al., 2019) and denser vascular vegetation (Jorgenson, 2000; Jorgenson et al., 1997), which may drive patterns in seasonal lake area change. In addition, higher sedimentation rates in lakes closer to the channels may also contribute to systematically shallower lakes (Jorgenson et al., 1997), which would then exhibit higher rates of summertime shrinkage under equal evaporation rates.

We propose that rigorously quantifying from remotely sensed data the seasonal dynamics of lake area extents as a function of their positions relative to the channel network will add valuable insight into the hydro-geomorphologic functioning of these systems, which is hard to directly measure in the field. It will also provide a means for improved estimates of carbon and energy fluxes, which are nonlinearly dependent on lake area extents. In this paper we present a detailed analysis of summertime lake shrinkage in two arctic deltas (Yukon and Colville) as a function of the distance to the nearest channel and document a highly structured variability which is specific to each delta, providing a signature of the system's hydro-geomorphologic structure and seasonal dynamics. Through consideration of possible explanatory variables (surface connectivity, temperature, and vegetation spatial structure) we propose predominant physical mechanisms for the observed patterns and suggest the attractive possibility of using remote sensing observations of lake area seasonal change to augment mechanistic understanding of arctic hydro-geomorphology.

3.2 Deltas, Data, and Channel Network Extraction

We studied the summertime lake area dynamics of two Alaskan deltas: the Yukon (apex at 62°N, $3,415$ km^2, discontinuous permafrost zone) and the Colville (apex at 70°N, 549 km^2, continuous permafrost zone) (Figure 3.1). The two systems have different climates, riverine sediment characteristics, and morphologies. The Yukon is characterized by abundant lakes but a lack of permafrost features such as polygonal tundra, a sediment load primarily of silty and sandy material (Dupre & Thompson, 1979), a mean annual air temperature of -1.2°C, and a mean summer air temperature of 11.6°C (NOAA GSOD Station 702005). The Colville is characterized by numerous lakes and permafrost features including ice-wedges and frost mounds, and has a sediment load of mainly sand and gravel (Walker, 1998), mean annual air temperature of -11.0°C, and mean summer air temperature of 6.2°C (NOAA GSOD Station 700637). Estimates of near-surface permafrost presence indicate a 98% chance of observing permafrost within 1 m of the surface on the Colville ((Pastick et al., 2015); Figure 3.1a), with active layer thickness between 36 and 100 cm, and vegetation composed of willows, sedges, and bryophytes (Jorgenson et al., 1997). This is in contrast with the 17% chance of near-surface permafrost on the Yukon ((Pastick et al., 2015); Figure 3.1a), indicating active layer thickness in excess of 1 m and/or the complete absence of permafrost, and vegetation composed of willows and sedges (Jorgenson, 2000).

To analyze lake area changes on the deltas, we used the Global Surface Water (GSW) data set which provides monthly 30-m spatial resolution, Landsat-derived global water cover masks from March 1985 to December 2018 (Pekel et al., 2016). We present analysis of the monthly lake shrinkage rates from June to July (summer), the months which have the greatest data availability and correspond to the period post-snowmelt and streamflow recession (see Appendix B for further information). Data availability and quality (e.g., missing data due to clouds, Landsat 7 striping, and snow cover) are variable during the time of record, so we applied a threshold of at least 60% of the delta (excluding the channel network) being resolved (i.e., classified as land or water), which was met for 10 summers on the Yukon and for 16 summers on the Colville (Figure B.2). To compare lake shrinkage rates from year to year, we used the Interactive Multisensor Snow and Ice Mapping System 24-km daily snow cover data set, available from 1997 till present, to compute the date of snow cover disappearance as the date when less than 15% of the study area was classified as snow (Helfrich et al., 2007; National Ice Center, 2008).

Computing lake area change as a function of the distance to the nearest channel required first extracting the Delta Channel Network (DCN) and second computing the distance of every pixel (land or water) to the nearest channel. Automatic channel network extraction for river deltas has recently been advanced with the Python package RivGraph (Schwenk et al., 2015), which utilizes water coverage imagery to extract and skeletonize the DCN. We found that no major channels avulsed or lake breaching took place on either delta during the period of record and therefore used a constant DCN (**see Appendix B for more details**). To reduce the effect of channelized flow, only water bodies (e.g., inundated depressions, ponds, and lakes, hereafter collectively referred to as lakes) disconnected from the channel network were considered in our analysis. We also utilized higher resolution DigitalGlobe imagery to account for small streams not visible in Landsat (see section 3.4). Once the DCN was extracted and the disconnected lakes were identified, we computed the shortest linear distance of every land or water pixel to the nearest channel, d_{nc}, a calculation equivalent to the distance transform of a binary image (Haralick & Shapiro, 1992). The probability distribution functions of d_{nc} for both deltas are provided in Appendix B.

3.3 Summertime Lake Area Dynamics as a Function of Distance to the Nearest Channel

We tested the control of the DCN on summertime lake area dynamics by quantifying the lake shrinkage rate, S, using a pixel-based monthly shrinkage estimate, S_p, as a function of d_{nc}. S_p is computed as the fraction of water area loss from 1 month to the next, in our case from June to July (see description of data availability and calculations in Appendix B). We found that both deltas, for every year in the period of record (2001–2018), showed a robust pattern in lake shrinkage rates (Figures 3.2a and 3.2c) with a systematic decrease of shrinkage rates farther away from the channels, reaching almost a constant rate after a distance characteristic of each delta (approximately $1,500$ m for Yukon and $2,000$ m for Colville). The interannual variability in the magnitude of S_p was identified as being associated with differences in the day of snow cover disappearance, with a higher shrinkage rate when snow cover disappeared later in the year, in our case closer to June; see Figures 3.2a and 3.2c. As the shrinkage pattern seems robust from year to year and is modulated only in magnitude, we estimated the weighted average normalized water area loss, $\bar{S_p}$, as a function of d_{nc}, shown in black in Figures 3.2a and 3.2c, where the weights were proportional to the number of valid (i.e., resolved) pixels each year in each distance bin. The observed summertime shrinkage signal is apparent in over 26 years of data over the two deltas, indicating that the topology and

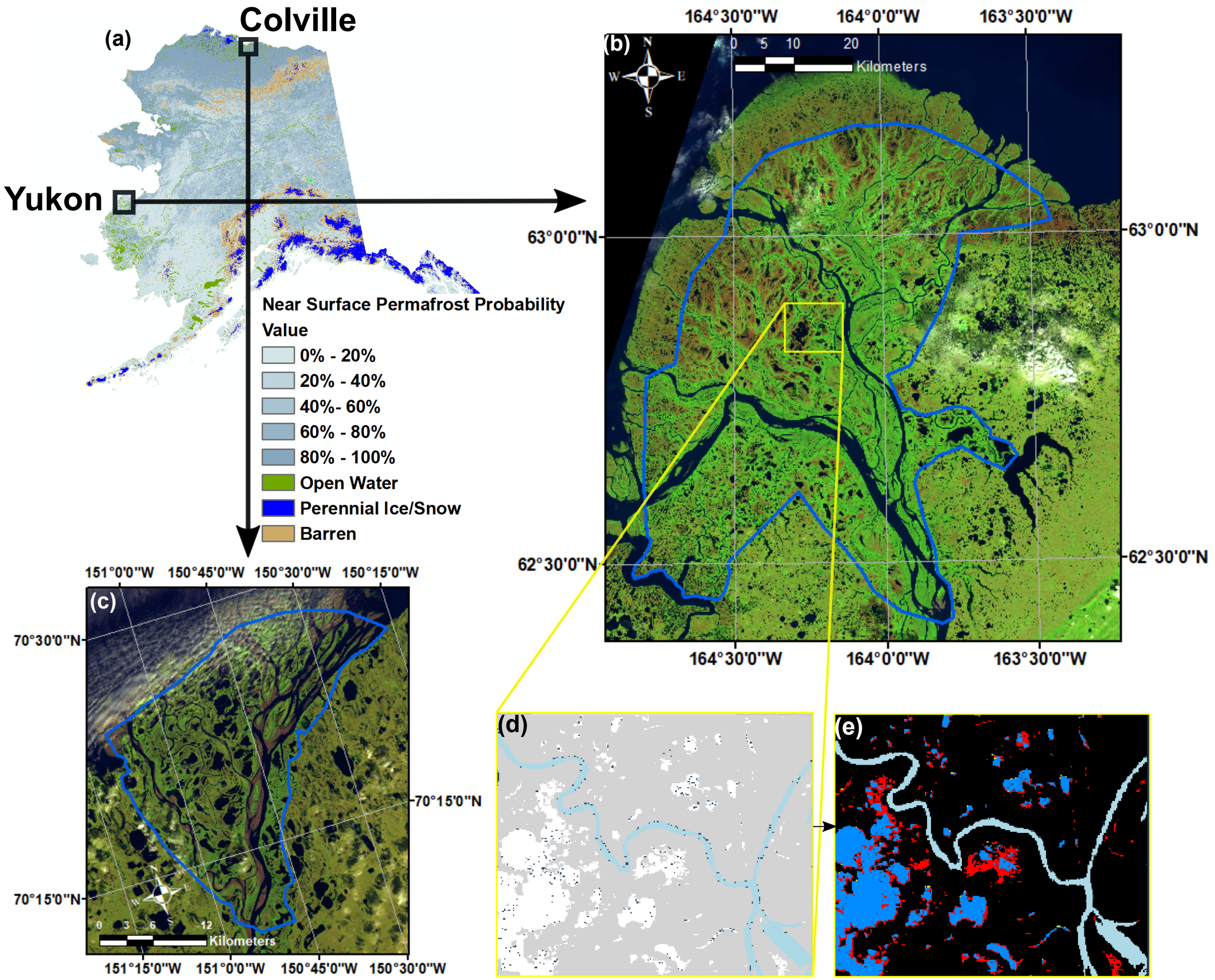

Figure 3.1: **Study areas and illustration of seasonal lake area shrinkage.** (a) A map of the near-surface permafrost probability from Pastick et al. (2015) and the locations of the Colville and Yukon deltas. (b) A Landsat 8 scene (falsely colored in R-Surface Water Infrared, G-Near Infrared, B-Green) taken on 6 July 2014 over the Yukon Delta, with the study zone outlined in blue. (c) The same over the Colville Delta on 12 August 2014. (d) The classified June 2008 water mask from the Global Surface Water (GSW) data set, with land in gray, channels in light blue, lakes in white, and no data in dark gray. (e) The lake area shrinkage from June to July 2008 is depicted with water that drained or evaporated marked in red, water that remained water in dark blue, and land shown in black.

geometry of the channel network leave a signature on the spatial pattern of lake shrinkage. While S_p can be computed in summers with missing data (e.g., due to cloud cover), this pixel-wise approach neglects the spatial context of the water pixels, i.e., lumps all water pixels together irrespective of their arrangement within specific water bodies. We know, however, that the location of a water pixel, e.g., an interior versus exterior pixel of a lake, is subject to different hydro-geomorphologic processes and thus analyzing shrinkage rates within an object-based context can provide complementary and physically interpretable information. This object-based approach, however, can only be performed on imagery with sufficient data quality (i.e., with a negligible fraction of no data pixels). To implement an object-based approach we used an iterative morphological erosion operation (see Figure 3.2 inset; (Haralick & Shapiro, 1992)) to classify water pixels according to their position in the different lakes. Specifically, we classified them as belonging to an internal perimeter (IP), with IP_1 indicating the shoreline perimeter of a lake, IP_2 the next internal perimeter, etc. We then estimated a monthly lake shoreline shrinkage rate, S_{IP_i}, computed as the fraction of water area loss of water pixels in IP_i, as a function of d_{nc}. We note that the weighted average of S_{IP_i} for all i, with weights proportional to the number of IP_i pixels over the total number of water pixels, will converge to S_p when all IPs are considered, i.e., when the morphological erosion operation has "eroded" all lakes to their center-point. We highlight the results of this object-based analysis for the first three IPs on the summer of 2014, when both deltas had over 99% of the nonchannel study area resolved, and compare them with the pixel-based analysis results made over multiple years. The shrinkage rate of the shoreline perimeter of lake bodies (IP_1) for year 2014 shows a well-behaved decreasing pattern as a function of d_{nc} (Figures 3.2b and 3.2d). On the Yukon, a steady but slower decrease in S_{IP_2} and S_{IP_3} is observed compared with S_{IP_1}. On the Colville, S_{IP_2} and S_{IP_3} decrease with d_{nc} albeit they are more variable. Independent of distance, as expected, the most external IPs have a higher rate of shrinkage, but decay to similar distances compared with the pixel-based shrinkage rate, S_p. Given that this method is a more direct representation of lake shrinkage compared to the pixel-based

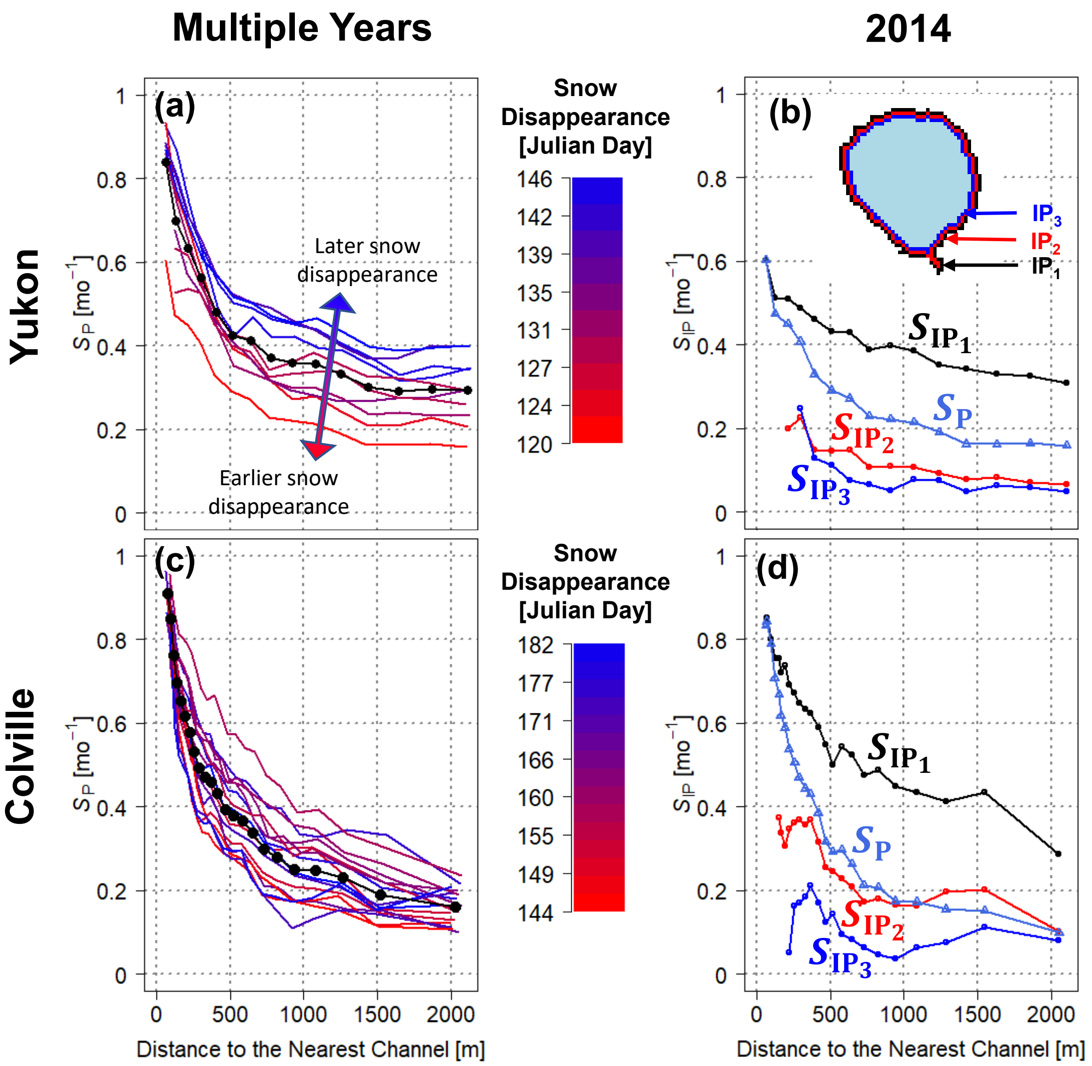

Figure 3.2: **Summertime lake shrinkage as a function of the distance to the nearest channel.** (a, c) Shrinkage rate, estimated by the monthly fraction of water area loss S_P as a function of d_{nc}, for 26 summers, each curve marked by the date of snow disappearance on the Yukon (a) and the Colville (c) with the weighted average shrinkage rate curve shown in a black dotted line. (b, d) The results of the lake shoreline shrinkage from an object-based analysis are shown for 2014 on the Yukon (b) and for 2014 on the Colville (d), with the pixel-based estimate shown in light blue as comparison. The inset in (b) highlights the first three Internal Perimeters (IPs) of a sample lake in black, red, and blue, with the remaining water shown in light blue.

approach and that similar patterns and length scales of shrinkage rates are identified, this result strongly supports the existence of a spatial organization of lake shrinkage rates around the channel network. It also validates the use of a pixel-based estimate which enables lake shrinkage rates to be quantified more readily even when there is missing data in the water masks.

3.4 Physical Attribution of the Spatial Pattern of Summertime Shrinkage

We explored three physical mechanisms that may contribute to the observed spatial pattern of shrinkage: surface connectivity of lakes closer to the channels via very narrow pathways not detected in the Landsat imagery of 30-m resolution, systematically shallower lakes closer to the channels versus farther away, and enhanced vegetation coverage and a thicker active layer closer to the DCN.

3.4.1 Drainage Due to Subpixel Surface Connectivity

At the 30-m spatial resolution of GSW, unresolved structural connectivity, e.g., narrow tie channels (Rowland et al., 2009), may lead to the mischaracterization of lakes as disconnected. The higher shrinkage rates may then be due to these subpixel channels, and therefore the decreasing shrinkage rate a signature of sub 30-m DCN structure. To test this, we randomly sampled between both deltas a total of $1,069$ lakes identified from the GSW imagery and used DigitalGlobe (0.31 to 0.65 m spatial resolution) imagery available via Google Earth to identify subpixel channel connectivity (see Appendix B for dates). Channel-lake connectivity was manually determined based on the observed presence or absence of small, connected channels over the summer months (June to August) as in Chen et al. (2013). On the Yukon we sampled 809 out of $12,745$ lakes in 2014, and found 547 lakes disconnected from the channel network. On the Colville we sampled a total of 260 out of $1,409$ lakes in 2014, and found 211 disconnected.

To evaluate the DCN control on shrinkage rates we used the GSW imagery to compute S_p for the subsampled lakes identified as disconnected at the DigitalGlobe 0.6-m resolution. We found that these lakes exhibited decreasing S_p as a function of d_{nc} up to $1,500$ m (Figures 3.3a and 3.3d), albeit the patterns are less smooth due to the small sample sizes. These results indicate that the higher shrinkage rates closer to the DCN are not the result of surface connectivity by narrow (< 30 m width) channels, but rather the result of near-surface hydro-geomorphologic processes.

3.4.2 Systematic Control on Lake Depth as a Function of Distance to the Nearest Channel

Lakes located closer to the DCN in general have higher inundation and sedimentation rates than lakes farther away, as indicated by the classification of Jorgenson (2000), and therefore might be shallower (i.e., lower height to width ratios closer to the DCN). Systematically shallower lakes closer to the DCN could then have higher shrinkage rates, even with equal evaporation rates. Here we wanted to test the hypothesis that systematic lake depth increase with distance is not the primary cause for the observed higher shrinkage rate closer to the channels. However, there is a lack of delta-wide lake bathymetry measurements to validate this hypothesis. As a proxy to bathymetry, we used water surface temperatures, positing that shallower lakes will likely have warmer surface temperatures than deeper lakes. We used Landsat Thermal Infrared (TIR) band-derived land surface temperature (LST) (Malakar et al., 2018) to analyze surface water temperatures over individual Landsat scenes. To obtain LST data from TIR reflectance, a thermal emissivity ϵ for each pixel must be specified, which

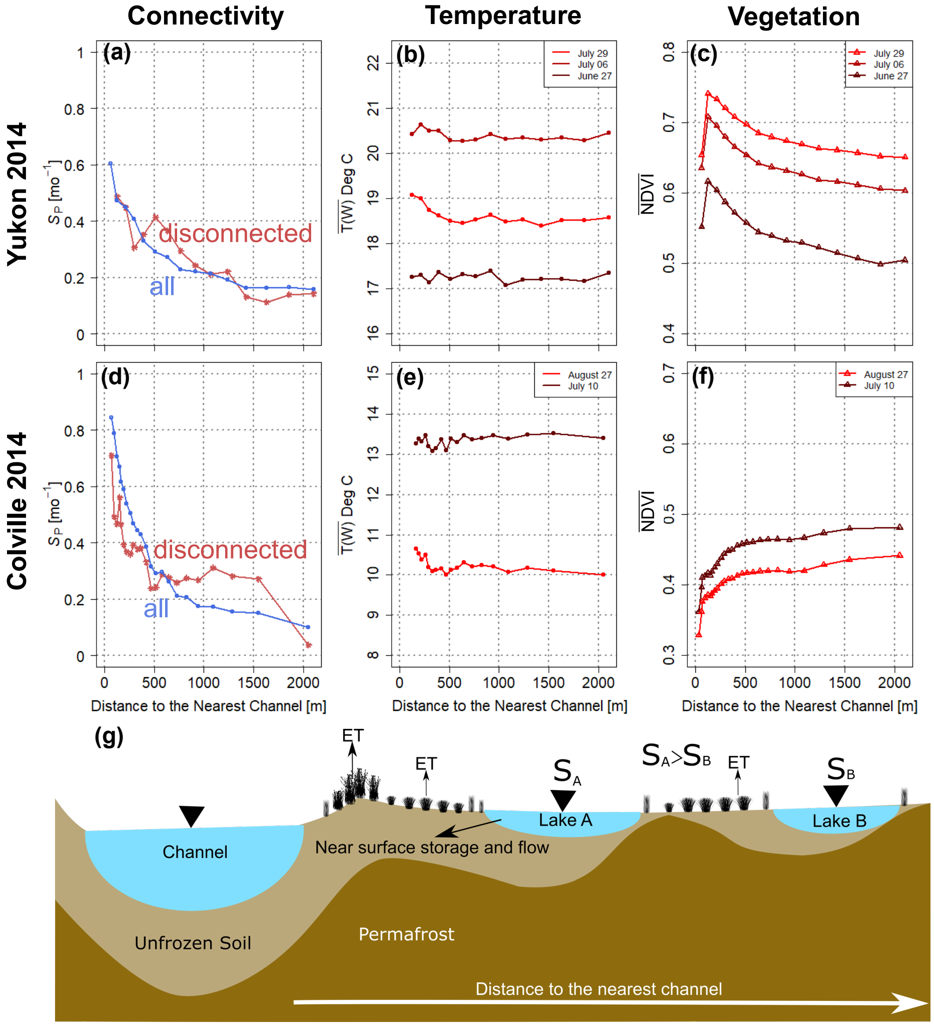

Figure 3.3: **Examining physical mechanisms for increased lake shrinkage closer to the delta channel network.** (a, d) Comparison of the 2014 water area shrinkage rates of all lakes disconnected from the channel network as inferred from the Landsat images at 30-m resolution (same as in Figures 3.2a and 3.2b) and a subset of lakes disconnected from the channels as inferred from high resolution (0.6 m) to rule out that subpixel surface connectivity not seen in Landsat cannot explain the observed structured shrinkage patterns. (b, e) Average surface temperature of water pixels in internal perimeter IP_2 (a proxy for lake depth) is independent of distance from the channel network indicating that lake depth is not the primary cause for the observed higher shrinkage rates closer to the channels. (c, f) Mean NDVI of June land pixels spikes and decreases on the Yukon (c), and steadily increases on the Colville indicating presence of barren sandbars next to the channels (f). (g) Schematic illustrating that the enhanced shrinkage, S, closer to the DCN is predominantly caused by increased near-surface storage and flow, a result of increased heat content near the channel, and modulated by higher evapotranspiration rates due to denser vegetation content on the Yukon.

is constant over water. To discard water LST variability due to emissivity heterogeneity, we analyzed only pixels classified as water both in the GSW and LST data set, i.e., pixels with ϵ greater than 0.99 in the spectral range of the Landsat 8 TIR.

Visual inspection of the Landsat scenes showed that the centers of lakes do not show significant temperature variability, likely due to a depth threshold being achieved where the water surface temperature is not primarily controlled by lake depth. To account for differences in lake morphology and for the fact that lakes are generally smaller closer to the channel network (Figure B.4), we analyzed the temperature on the outer edges of the lake (e.g., IP_2). We found that the average outer perimeter water temperature was nearly constant, i.e., independent of d_{nc} (Figures 3.3b and 3.3e). As we explicitly account for the position of a water pixel relative to the edge of the lake it lies in, this analysis specifically tests whether there are systematically warmer, and thus shallower, lake banks closer to the DCN. The nearly constant temperature observed across the edges of lakes on the deltaic surface does not support the hypothesis of systematically shallower lakes closer to the DCN, implying that lake depth is not the primary control of the observed shrinkage pattern.

3.4.3 Enhanced Near-Surface Connectivity and Vegetation Density by the DCN

Extensive field studies on the Colville and the Yukon-Kuskokwim delta have found that in permafrost affected fluvial landscapes, the coevolution of landforms, permafrost, and vegetation imprints distinct spatial patterns on the geomorphology and ecology of the landscape (Jorgenson, 2000; Jorgenson et al., 1997; Shur & Jorgenson, 2007). These studies have documented a gradient in vegetation density and type with distance from the channels, with barren sandbars immediately around the channel network, followed by vascular vegetation including willows and shrubs in the active floodplain around the DCN, compared with greater sedge and bryophyte density in the inactive floodplain farther from the DCN, indicative of deeper active layer thickness near channels (Jorgenson et al., 1997, 1998; Jorgenson, 2000). In the active floodplain, higher rates of sedimentation limit organic matter deposition and permafrost aggradation, while the inactive floodplain has a thicker organic layer, which insulates and protects frozen soil contributing to shallower depth to permafrost (Jorgenson et al., 1998). On the Colville, visual inspection showed that the channel network is abutted by barren sandbars, while on the Yukon the channel network is generally enveloped by land cover with high near infrared reflectance, colored in green in Figure 3.1b, indicative of greater vegetation density and photosynthetic activity (Laidler et al., 2008). Given greater sand deposition immediately around the DCN and enhanced vegetation content on the floodplain closer to the DCN (Jorgenson et al., 1998), greater shrinkage rates may be due to greater subsurface flow pathways (due to deeper active layers) and higher evapotranspiration rates (Figure 3.3g). Due to a paucity of field observations of subsurface flow and evapotranspiration rates spanning the spatial and temporal domains analyzed, we examined DCN control on vegetation coverage using Landsat-derived Normalized Difference Vegetation Index (NDVI) as a proxy for vegetation density and therefore evapotranspiration rates.

Individual Landsat scenes from June to August 2014 over both deltas were used to compute the mean NDVI of land, as identified from the June 2014 GSW water mask, as a function of d_{nc} (Figures 3.3c and 3.3f). On the Colville, an increase in NDVI with d_{nc} is observed for both Landsat scenes, which is due to the sparsely vegetated sandbars adjacent to the channels, that undergo frequent ice scouring and reworking (Jorgenson et al., 1998), thus significantly decreasing the mean NDVI. On the Yukon, a sharp increase in NDVI followed by a decrease until $1,500$ m from the channel is observed, which corresponds to some sandbars present on the edge of the DCN, followed by dense vegetation which decreases as a function of d_{nc}. These interpretations are consistent with field survey photos provided by N.J. Pastick; see also Pastick et al. (2014). The overall average NDVI in the colder Colville delta is relatively lower than in the warmer Yukon delta and indicates sparser vegetation and lower photosynthetic activity. However, as indicated by transects from field surveys done on the Colville between 1992 and 1996, the deepest thaw depth and coarsest soil is located in these sandbars (Jorgenson et al., 1997), which implies greater water storage capacity and hydraulic conductivity closer to the DCN. The relatively shallower thaw depths on the colder Colville delta have less near-surface storage and flow capacity than the warmer Yukon delta, which likely contributes to the steeper gradient in shrinkage rates (Figures 3.2a and 3.2c). The presence of deeper thaw zones closer to waterbodies in the Arctic is supported by numerical modeling and observational evidence (Rowland et al., 2011; Woo, 2012). For example, comparison of a borehole located 6 m versus 145 m from the edge of a fjord in Svalbard showed significantly higher maximum and average temperatures throughout the soil profile at the site closer to the fjord (Kristensen et al., 2008). In addition, heat advection from near-surface flow accelerates heat transport, preventing permafrost formation or thawing existing permafrost (Aas et al., 2019; McKenzie & Voss, 2013; Rowland et al., 2011; Walvoord & Kurylyk, 2016; Wellman et al., 2013). Empirical estimates of near-surface permafrost indicate that the probability of observing shallow permafrost increases with distance from the channel network (Pastick et al., 2015) (Figure B.5). These studies provide evidence that waterbodies and water flow modify subsurface flow pathways via modulation of temperature-controlled soil permeability; therefore, enhanced shrinkage due to near-surface connectivity may act as a positive feedback by maintaining a deeper active layer thickness and in turn amplifying near-surface storage and flow. This effect is likely present near all lakes (Figure 3.3g), not only near the DCN, and contributes to the length scale of DCN control on shrinkage rates.

3.5 Conclusions

Analysis of the summertime surface lake area dynamics of arctic deltas indicates that lake area extent primarily decreases following snowmelt, and that the monthly shrinkage rate strongly depends on the distance from the channel network, with higher shrinkage rates closer to the channels. This signal is detected every summer over a combined 26 years of satellite observations over two deltas of different climate and morphology. This seasonal lake shrinkage signal should be considered in future estimates of lacustrine methane emissions, e.g., those based on nonlinear relationships between methane emission and lake area (Bastviken et al., 2004), to constrain uncertainties in the arctic carbon budget. Higher rates of decreasing water coverage closer to the channels will imply a spatially heterogeneous but structured distribution of methane emissions within a delta which must be accounted for in regional or global assessments and also in projected trends (Cooley et al., 2019). The higher shrinkage rates seen closer to the channel network are likely primarily caused by enhanced near-surface storage and flow closer to the channels and by denser vegetation coverage, a signature of the coevolution of landforms, permafrost, and ecology of these arctic landscapes. As the observed pattern is therefore controlled, in part, by physical processes that are difficult to measure in the field (i.e., near-surface flow and storage), this analysis presents the potential for partial inference of such processes from targeted analysis of readily available Landsat imagery. The spatial and temporal variability of surface and subsurface hydrologic connectivity of lakes in arctic deltas and future trends under warmer temperatures is of the utmost importance for assessing and constraining estimates of carbon emissions and for providing quantitative metrics of change. For example, permafrost thaw and associated increasing hydrologic connectivity (Walvoord & Kurylyk, 2016) may shift colder systems such as the Colville to experience increased near-surface flow, altering residence and transport times of water and nutrients on the delta. Future work will expand the analysis to a larger set of arctic deltas (Piliouras & Rowland, 2020), and use connectivity theory (Tejedor et al., 2015a,b, 2018) to quantitatively study the topology of the complex channel-lake networks of arctic deltas and their expression on the patterns of seasonal lake shrinkage rates.

CHAPTER 4

Climate Signatures on Lake And Wetland Size Distributions in Arctic Deltas

4.1 Introduction

Coastal river deltas are landscapes at significant risk from sea level rise and sediment deprivation (Nienhuis et al., 2020; Syvitski et al., 2009). Arctic deltas are likely more vulnerable than their temperate counterparts due to the presence of thermokarst lakes in permafrost, which are sensitive to rapid Arctic warming (Emmerton et al., 2007; Piliouras & Rowland, 2020; Walker, 1998). Pan-arctic thermokarst lake coverage is responding to warmer temperatures in complex ways, as temperature-driven ground ice loss drives lake growth through retrogressive thaw slumping along lake shorelines (Grosse et al., 2013) but also generates surface and subsurface hydrologic connectivity that can cause lake drainage (Grosse et al., 2013; Jones et al., 2020; Rowland et al., 2011; Yoshikawa & Hinzman, 2003). Observed changes in lake area over the last 50 years have shown both positive and negative trends depending on local hydrology, climate, permafrost zonation, ice content, landscape age, and geomorphic setting (Arp et al., 2011; Chen et al., 2012; Jones et al., 2011; Nitze et al., 2018; Plug et al., 2008; Smith et al., 2005). Irrespective of whether lake coverage is expanding or decreasing, the reorganization of thermokarst lake cover will have significant implications for polar atmospheric carbon fluxes (Engram et al., 2020; Grosse et al., 2013; Petrescu et al., 2010; Rowland et al., 2011; Van Huissteden et al., 2011; Walter Anthony et al., 2018).

Moreover, thermokarst lakes in deltas modulate the transport of riverine freshwater, sediment, and nutrient fluxes to the Arctic ocean, by trapping and holding sediment (Marsh et al., 1999; Piliouras & Rowland, 2020) and modifying the residence times and pathways of nutrient transport through the delta (Cunada et al., 2021; Emmerton et al., 2007; Lesack & Marsh, 2010; Squires et al., 2009; Tank et al., 2009). Therefore, changing deltaic lake coverage and its spatial distribution will also alter the timing and magnitudes of riverine fluxes to the Arctic Ocean, which has broader implications for near-shore circulation and ecosystem productivity (Lique et al., 2016).

We hypothesize that lake size variability and spatial arrangement across arctic deltas (Figure 4.1) may encode information on climate influence in permafrost environments, akin to how channel network structure is a signature of the riverine, tidal, and fluvial fluxes, which shape temperate deltas (Nienhuis et al., 2016, 2018; Tejedor et al., 2015a,b, 2016, 2017) (see also (Seybold et al., 2007; Zanardo et al., 2013) for the signature of climate in fluvial networks). In particular, we hypothesize that two primary drivers of lake size variability across deltas are ice content and climate and test this hypothesis quantitatively. Physically we expect that colder deltas have thicker permafrost, which is able to support larger lakes by preventing connection to the sub-permafrost groundwater table that can lead to eventual lake drainage (Grosse et al., 2013; Walvoord & Kurylyk, 2016; Yoshikawa & Hinzman, 2003) or diminished lake growth rates. We also expect that deltas with greater soil ice fraction will have larger lakes as soil ice acts as a subsurface hydraulic barrier, while soil ice melt induces subsidence and therefore lake growth. The hypothesized relationships between lake size and ice content or temperature would be useful for constraining physical models and predicting the future of arctic delta morphology in a warmer climate.

However, a challenge in assessing the climatic signature on thermokarst lake sizes is the significant interannual (Grosse et al., 2013; Rey et al., 2019) and seasonal variability (Chen et al., 2012, 2013; Cooley et al., 2019; Vulis et al., 2020) in lake area, which makes it difficult to distinguish perennial waterbodies (lakes) from ephemerally inundated depressions (wetlands) using the short summertime window of available spaceborne observations. In particular, seasonal water may inundate ephemeral wetlands, which would be misidentified as perennially inundated lakes from remote-sensing imagery. The processes underlying ephemeral wetland versus perennial lake formation are distinct, as lakes are the result of thermokarst-driven growth and evolution (Grosse et al., 2013), while wetlands are the result of hydrologic variability (Le & Kumar, 2014), and as defined in this study, only seasonally inundated. These ephemerally inundated wetlands likely have less significant thermal impacts on the landscape than lakes, and are thus expected to lack a relationship with delta climate. In the remainder of this study, we present a methodology to mine the historical Landsat imagery record to distinguish lakes and wetlands, and then characterize their respective size distributions as well as their potential dependence with climate.

4.2 Study Sites, Data, and Lake and Wetland Extraction

Lake and wetland size distributions on 12 arctic deltas characterized by a range of air temperature and ice content across Siberia (Indigirka, Kolyma, Lena, Nadym, Ob, Pur, Yana, and Yenisei), Canada (Mackenzie), and Alaska (Colville, Kobuk, and Yukon) were examined (Figure 4.1). The deltas include those formed by the six arctic rivers with the greatest discharge and other major rivers along the Siberian and Alaskan coastlines. Lakes and wetlands were extracted over the subaerial portion of each delta, which was delineated using Google Earth. Delta Mean Annual Air Temperature (MAAT) was obtained from 2000 to 2016 using the 15-km spatial resolution Arctic Systems Reanalysis V2 (Bromwich et al., 2018). Delta soil ice content was estimated from a 12.5-km spatial resolution ice classification map (Brown et al., 1997). To distinguish between hydrologically perennial lakes and ephemeral wetlands,

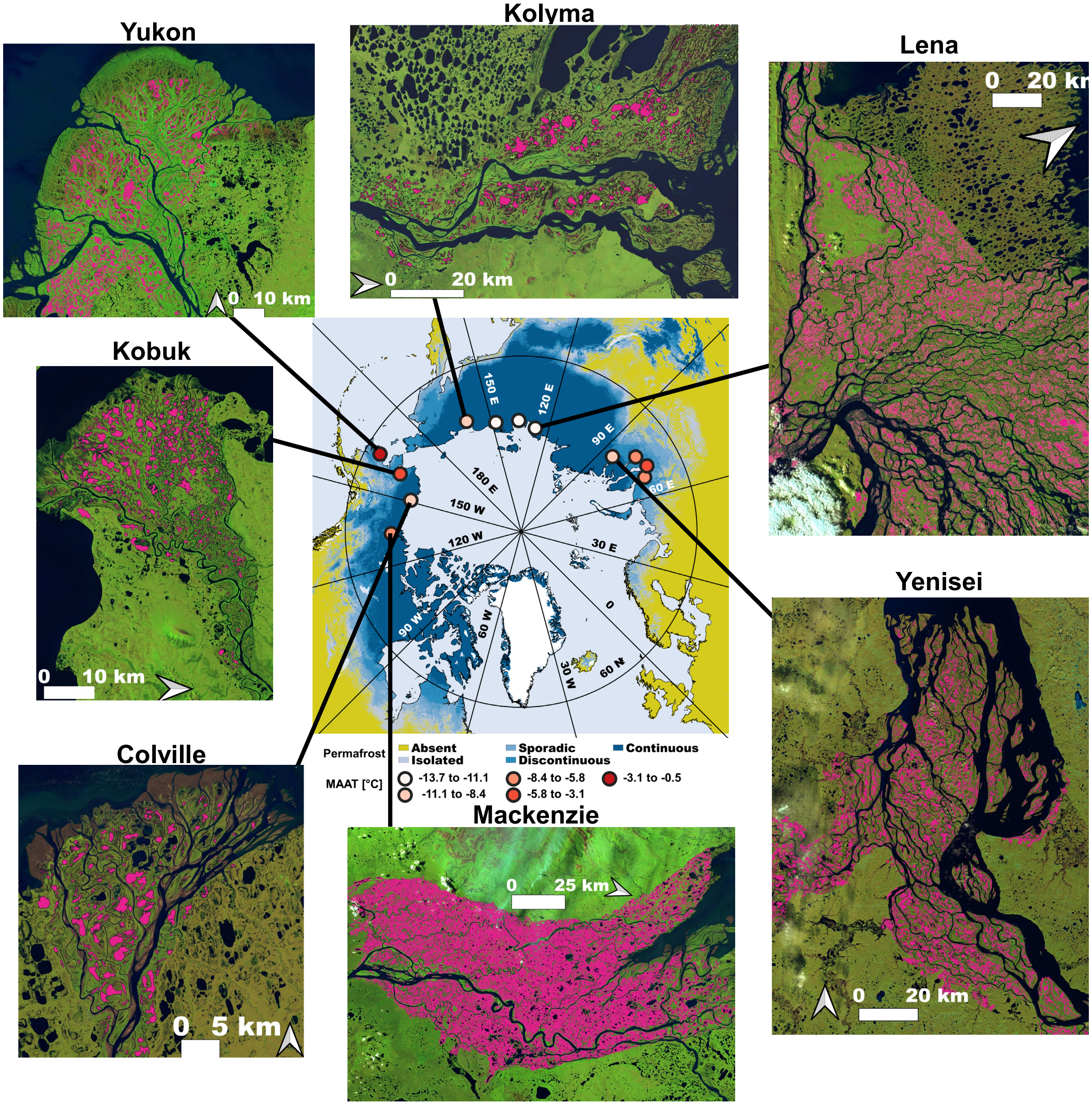

Figure 4.1: **Arctic deltas examined in this study.** Twelve arctic deltas (see colored open circles in the central panel for location) were examined along a range of Mean Annual Air Temperature (MAAT) and ice content. The central map shows delta locations, colored by 2000-2016 mean MAAT, estimated from the Arctic Systems Reanalysis V2 (Bromwich et al., 2018), and underlain by Arctic permafrost zonation(Obu et al., 2019). Summertime Landsat-8 scenes of 5 out of the 12 delta are shown with waterbodies identified from a single July Global Surface Water mask (Pekel et al., 2016) colored in pink.

we utilized the spatiotemporal interannual variability of water coverage over each delta from 1999 to 2018. We used the Landsat-derived, 30-m spatial resolution Global Surface Water (GSW) data set, which provides monthly composited water masks from March 1984 to December 2018 that classify the landscape into 30-m pixels that are land, water, or no data (i.e., unable to classify due to cloud cover, Landsat-7 striping, or snow and ice cover) (Pekel et al., 2016). Due to sparse data availability prior to 1999 on most deltas, we only analyzed the period from 1999 to 2018, and to remove the effect of significant snowmelt and spring time flooding, we restricted our analysis to July water masks similar to other studies (Muster et al., 2019; Nitze et al., 2018). We only examined the subaerial portion of each delta, manually delineated using Google Earth.

To identify and separate lakes from wetlands, we first computed for every pixel i the July "water pixel occurrence," w_i, as the fraction of Julys from 1999 to 2018 for which the pixel was classified as water, discarding no-data pixels (Figure 4.2a). The water pixel occurrence w_i can take values from 0 to 1, with $w_i = 1$ if and only if the pixel was classified as water for the whole record, and $w_i = 0$ if and only if the pixel was classified as land for the whole record. Second, we identified a reference year, y^*, with water coverage on the subaerial delta closest to that of the temporal average over the 20-year period of record and sufficient data quality (i.e., greater than 99% pixels classified as land or water and no significant georeferencing (collocation) errors) and used this year to identify individual waterbodies using 8-neighbor connected component analysis (see Appendix C, Figures C.1 to C.3 for details on selection of $y^{\{}ast)$. Third, we classified the waterbodies identified in year y^* into lakes and wetlands using the water pixel occurrence, w_i. For each waterbody, $O_k^{y^*}$, we computed the "occurrence index" B_k as the mean of w_i for all pixels within $O_k^{y^*}$, which corresponds to the fraction of pixels within the waterbody that were on average occupied by water over the 20 years (Julys) of record. A waterbody was then classified as a lake if B_k exceeded a threshold value θ and as a wetland if B_k was less than θ. We evaluated the results over a range of θ values, from $\theta = 0.80$ to $\theta = 0.90$, to account for differences in the flooding regime across different deltas and to test the robustness of our results (Tables C.1 to C.3 and Figures S4 and S5 in Appendix C). The lake and wetland size distributions shown in Figures 4.3 and 4.4 are extracted at a threshold value of $\theta = 0.85$. Only waterbodies at least $5,400$ m^2 (i.e., six pixels) in size were included in our analysis to reduce estimation errors at small areas. We tested the robustness of our methodology by performing a duplication, wherein we selected an alternative reference year, y^*_{alt}, with similar water coverage and data quality to extract waterbody extents and repeated the analysis (Appendix C, Table C.4, and Figures C.4 and C.5). All analyses were performed in R using geospatial and image processing packages (Gillespie, 2015; Hijmans, 2020; Pau et al., 2010; Pebesma, 2018, 2021).

4.3 Lake Size Distributions and a Proportionate Growth Model

From a simple thermodynamical perspective, thermokarst lakes are thermal reservoirs, which interact with their surroundings through heat exchange. In particular, unfrozen lake waters are net heat sources, thawing the surrounding ice-rich soil, which leads to lake basin expansion (Grosse et al., 2013). As larger lakes have a larger thermal inertia, they remain unfrozen for longer periods (Grosse et al., 2013) and maintain larger lake to soil temperature gradients, which enables them to grow at faster rates. Thus, based on this simple thermodynamical argument, and on field observations (Jones et al., 2011), we can postulate that thermokarst lake growth is compatible with a stochastic proportionate growth model (Crow & Shimizu, 1988; Mitzenmacher, 2004) (i.e., growth rate proportional to lake size), where stochasticity arises from the variability of soil properties that modulate growth. A key property of this general class of proportionate growth models is that they generate objects (in our case lakes) with sizes obeying a lognormal (LN) distribution (Appendix C; Crow & Shimizu (1988)). Thus, our expectation based on simple physical arguments is that arctic

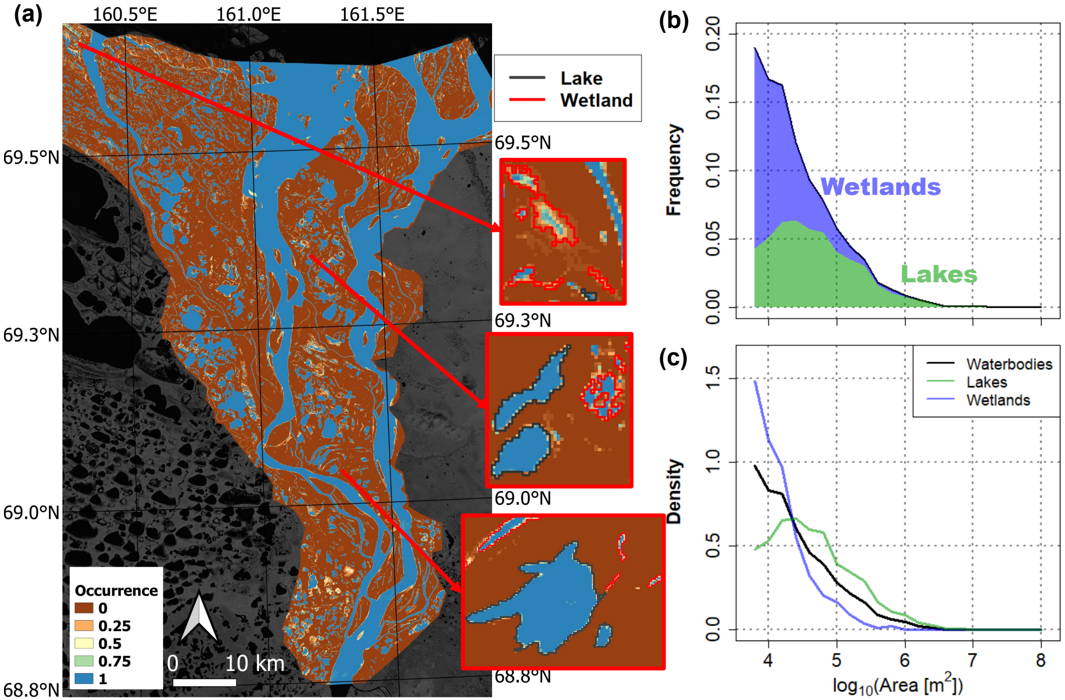

Figure 4.2: **Example of waterbody classification procedure on Kolyma Delta.** The waterbody classification procedure which marks waterbodies as either perennial lakes or ephemeral wetlands based on their July occurrence index, and the resulting size distribution. (a) July pixel water occurrence w_i over the Kolyma delta from 1999 to 2018. Brown indicates land pixels ($w_i = 0$) and blue indicates perennially inundated water pixels ($w_i = 1$), with colors in between indicating water pixels indicated only a fraction of the time. (b) The histogram of waterbody sizes is partitioned into the relative fraction of lakes (green) and wetlands (blue) at an occurrence index threshold $\theta = 0.85$. (c) The probability density function (PDF) of lake sizes in green and wetland sizes in blue, compared with waterbody sizes in black.

deltas should universally exhibit lakes whose sizes are lognormally distributed. In particular, since we only observe lake sizes above $5,400$ m^2 (six pixels), we expect lake sizes to follow a truncated lognormal distribution (Equation 4.1):

$$f_X(x;\nu,\beta^2) = \begin{cases} 0 & \text{for } x < x_{min} \\ \frac{\frac{1}{x\beta\sqrt{2\pi}} e^{\frac{-(\ln(x)-\nu)^2}{2\beta^2}}}{1-\Phi(\frac{\ln x_{min}-\nu}{\beta})} & \text{for } x \geq x_{min} \end{cases} \tag{4.1}$$

where $\Phi(\cdot)$ is the cumulative distribution function (CDF) of a standard normal variable, ν is the scale parameter, β the shape parameter, and x_{min} the minimum value at which the LN is observed, here $5,400$ m^2 (Clauset et al., 2009). When x_{min} approaches zero, the denominator approaches unity and 4.1 is simply the LN distribution. Having separated lakes and wetlands based on the methodology outlined in Section 4.2, we examined the empirical probability density function (PDF) and exceedance probability of lake sizes (Figures 4.3a and 4.3b). As postulated, we found that the examined lake sizes can be accurately described by a truncated LN distribution for the whole range of lake sizes (spanning 3.5 orders of magnitude) in the 12 deltas under study (see Quantile-Quantile (Q-Q) plots in Figure 4.3b). The rigorous Lilliefors-corrected Kolmogorov-Smirnov (KS) test (Clauset et al., 2009) shows that for every delta, the fitted LN distribution could not be rejected at the 5% significance level within the range of thresholds utilized for the identification of lakes from the general waterbody population (Tables C.1 to C.3 in Appendix C). For most deltas, the LN fit could not be rejected over the entire range, but in several deltas the test outcome depended on the threshold, due to the fact that the hydrogeomorphological specificities of the different deltas can lead to potential suboptimal lake/wetland separation for certain threshold values and ranges of waterbody sizes. Furthermore, the robustness of the revealed universality of the LN distribution of lake sizes was confirmed by successfully testing that lake sizes are LN distributed when alternative years were used as reference to extract waterbodies (Table C.4, Figure C.4). Previous empirical (suggesting different distributions for arctic waterbodies)

(Muster et al., 2019) and theoretical (suggesting a proportionate growth model) (Victorov et al., 2019) studies have failed to demonstrate this universality because thermokarst lakes and wetlands were analyzed together (Table C.5 and Figure C.6), and as we show in the next section, wetlands do exhibit a different distribution.

4.4 Wetland Size Distributions and an Inundated Topography Model

Arctic delta wetlands are, by definition, ephemeral waterbodies emerging on the delta top due to local ice/snow melt and riverine flooding. Therefore, wetland sizes are expected to be highly dependent on the seasonal delta hydrology, which controls overall delta wetness (hydrologic forcing), and delta topography; the topography in turn constitutes the spatial layout for inundation and controls both the emergence of disjoint wetlands and their sizes for a given forcing. The prevalence of power law distributions describing the sizes of waterbodies emerging from landscape inundation has been extensively documented (Bertassello et al., 2018; Cael & Seekell, 2016; Cael et al., 2015; Le & Kumar, 2014; Mandelbrot, 1982; Messager et al., 2016). For instance, recent analysis of the sizes of wetlands identified from inundating low-relief topography and observed wetlands in the contiguous United States were found to exhibit power law distribution of areas consistent with inundated topography (Bertassello et al., 2018; Le & Kumar, 2014). Therefore, our hypothesis was that the Arctic delta wetlands will follow a similar distribution. The form of the power law PDF used in this study is given in Equation 4.2, where x_0 is the minimum size above which the power law is fit and α is the power law exponent (Clauset et al., 2009):

$$f_X(x;\alpha) = \frac{\alpha - 1}{x_0}\left(\frac{x}{x_0}\right)^{-\alpha}, x > x_0 \tag{4.2}$$

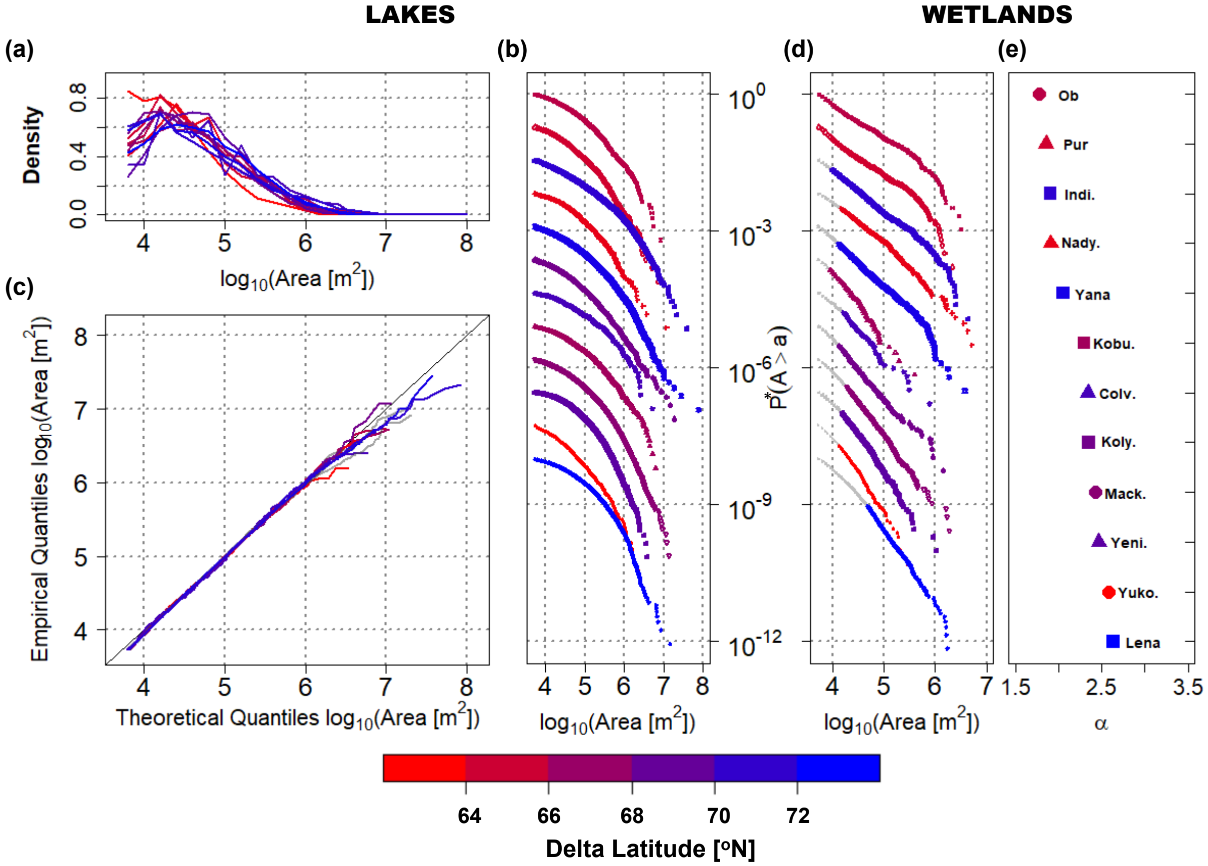

Figure 4.3: **Size distributions of lakes and wetlands extracted at occurrence index threshold $\theta = 0.85$.** (a) Lake size probability density functions (PDFs) for the 12 deltas, (b) lake size exceedance probabilities, and (c) quantile-quantile plots of the lognormal with truncation from below at the minimum lake size (5,400 m^2) fitted to the lake size distribution. In (b) fitted distributions whose fit to data is rejected at the 5% significance level (Kolmogorov-Smirnov (KS) test) are in grey. (d) Wetland size exceedance probability, (e) fitted power law exponent, α, of all 12 deltas. The exceedance probabilities in (b) and (d) are rescaled by a factor τ, i.e. $P^* = P_\tau$, for visual display and comparison of the differences between lake and wetland size distributions on each delta. The distributions are ordered by increasing values of α to highlight the range of observed α. For each delta, power laws are fit to the colored points above the minimum wetland size, x_0, which was optimally determined using the procedure of Clauset et al. (2009). The power law parameter α in (d) is the scaling exponent of the PDF.

We observed that wetland size distributions in the 12 arctic deltas indeed show strong evidence of being power law distributed (log-log linearity over two orders of magnitude in Figure 3d). Using the robust methodology of Clauset et al. (2009) for power law testing and fitting, we found that the power law hypothesis for wetland sizes could not be rejected at the 5% significance level with a Lilliefors-corrected KS test for 11 out of 12 deltas (at $\theta = 0.85$, Table C.1). As with lakes, the power law distribution of wetland sizes is robust with respect to the threshold, which establishes the separation of waterbodies into lakes and wetlands (Tables C.2 to C.3). Moreover, the robustness of our hypothesis was verified by extracting waterbodies and identifying wetlands in an alternative reference year, wherein again most deltas displayed power law wetland size distributions (Table C.4, Figure C.4) The observed power law exponents range from 1.8 to 2.8 and are similar to what has been found for wetlands in the contiguous United States (Bertassello et al., 2018; Le & Kumar, 2014) and other waterbodies on multiple scales (Cael et al., 2015). The range in the observed exponents at different thresholds is attributed to the hydrogeomorphic variability within and across the deltas, and the imperfect separation between lakes and wetlands. We point out that the evaluation of alternative models such as the LN distribution cannot be performed on a statistical basis, for example, using the Akaike Information Criterion (Burnham & Anderson, 2004), due to the limited sample size (for more details see Appendix C; Figure C.8; (Clauset et al., 2009)). However, the observed power law exponents and the lack of interpretability of the alternative distribution (e.g., LN) parameters strongly suggest that the power law is a physically meaningful model to describe the wetland size distribution (Appendix C). Recent literature has hypothesized that lakes in the Arctic are consistent with landscape inundation mechanisms (Muster et al., 2019). This hypothesis was grounded on the finding that empirical statistics of waterbodies obey two relationships (a linear relationship between conditional mean and conditional variance and a hyperbolic relationship between conditional mean and conditional skewness), which are consistent with those arising from an inundation model experiment (Muster et al., 2019). However, as we show here (Appendix

C, Figure C.9), these same relationships arise from a proportionate growth model and an LN distribution, cautioning their use for distinguishing between the power law and LN probability distributions and for making physical inferences.

4.5 Climate Trends

How thermokarst lake coverage on arctic deltas will respond to projected 21st century warming is a question of critical interest due to the impacts on methane emissions (Engram et al., 2020; Petrescu et al., 2010; Van Huissteden et al., 2011), the release of old carbon (Grosse et al., 2013; Rowland et al., 2011), replumbing of surface-subsurface hydrologic partitioning (Walvoord & Kurylyk, 2016), and changes in water and biogeochemical cycling to the ocean (Piliouras & Rowland, 2020; Piliouras et al., 2021). Discovering robust relationships between lake size distributions and climate variables such as temperature and soil ice content would provide valuable insight into the future of lake coverage on arctic deltas. Given the clear differences in lake versus wetland size distributions (Figure 4.3) and their associated generative processes, we reemphasize the hypothesis that only lake sizes should encode the signature of climate through temperature and ice content, while ephemeral wetlands should be agnostic to it. We have tested this hypothesis by analyzing the relationships between mean lake and wetland size (areal extent) with respect to MAAT and soil ice content. The data suggest that the mean thermokarst lake size increases by $9 \cdot 10^4$ m^2, that is, doubling, over a $12°C$ decrease in the average 2000 to 2016 MAAT (Bromwich et al., 2018), indicating that colder deltas have significantly larger lakes on average (Figure 4.4a). Modern MAAT may not be representative of paleoclimatic temperature variability; however, mean lake size also has a significant linear relationship ($p = 0.023$, bootstrap $p = 0.023$, and $R^2 = 0.42$) with delta apex latitude, which is a reasonable proxy for historical temperature differences between the deltas, strongly supporting a temperature to lake size relationship. Mean lake size also generally positively relates to soil ice content, as higher ice content on the delta may support lake growth due to greater settlement from ice melt (Grosse et al., 2013), with lower ice content associated with smaller lakes (Figure 4.4a). A similar trend between lake sizes and MAAT is observed when an alternative reference year is used to extract waterbodies in (Figure C.5a), supporting the robustness of this dependence. On the other hand, the data show no relationship between mean wetland size and MAAT (Figures 4.4b and **S5b**). Also expected, but confirmed, mixing the two waterbodies makes it hard to detect the climatic signal on the landscape. Indeed, a joint analysis reveals a non-significant relationship with MAAT (Figure C.6d).

The observed relationship for mean lake size and MAAT is attributed to the greater capacity of colder deltas to support large lakes due to their presumably thicker and cooler permafrost, which prevents sub-lake taliks from connecting to the sub-permafrost groundwater table (Walvoord & Kurylyk, 2016). This connection in low relief deltaic environments would reduce lake level as river stage recedes through the summer, transitioning the margins of perennially inundated lakes to ephemerally inundated, thereby reducing lateral thermal fluxes from the lake to the surrounding permafrost, that is, diminishing lake growth and decreasing the observed size of perennially inundated lakes (Figures 4.4c and 4.4d). Such an effect would be clearest in large lakes that have deep taliks (Grosse et al., 2013), and indeed, we found that the peripheries of large lakes were inundated more often on average over the period of record on warmer deltas compared with colder deltas (see Figure 4.4e). Note that the fraction of the periphery that remains water (inundated) on average over the period of record was quantified as the mean w_i of all pixels bordering each lake (in an 8-neighbor sense), and the average value for the large lakes (defined as those with areas between 10^5 and 10^6 m^2) is reported for each delta.

Such a relationship between MAAT and lake periphery inundation may also occur due to evapotranspiration rates being higher on warmer deltas, which leads to greater lake margin

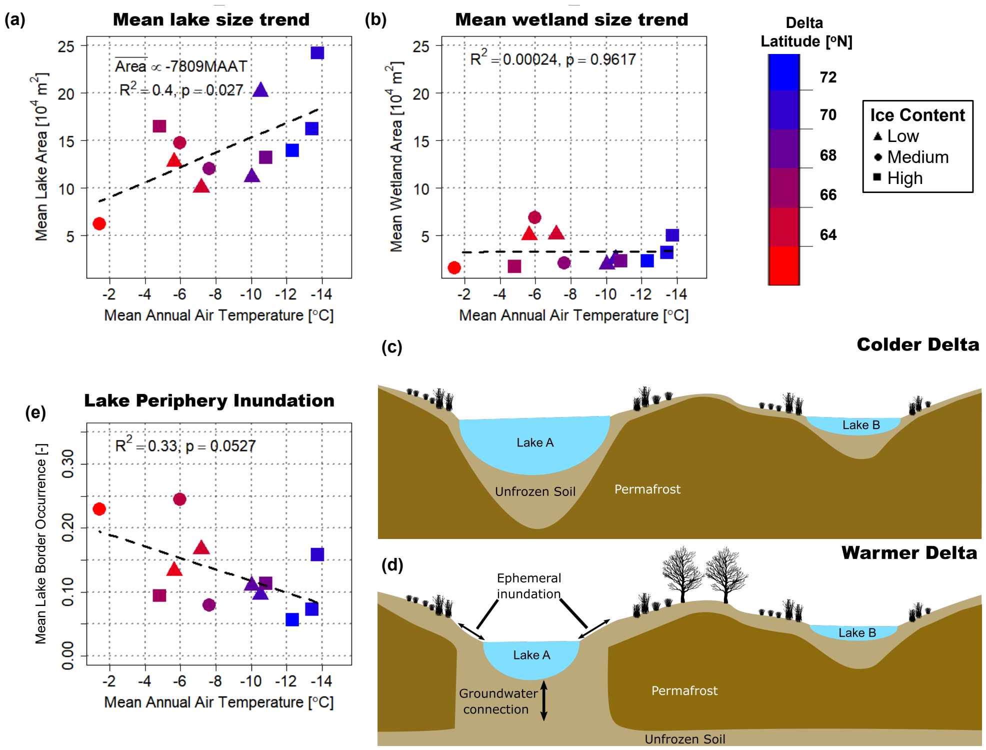

Figure 4.4: **Lake and wetland size climate trends.** (a) Scatterplot between mean lake size and MAAT showing a significant relationship between the two, with bootstrap $p = 0.0264$ and Spearman rank correlation -0.5 ($p = 0.1038$). A significant trend between the 90^{th} percentile of lake sizes and MAAT ($p = 0.041$, bootstrap $p = 0.0366$, and $R^2 = 0.36$) was also found (not shown). (b) Scatterplot between mean wetland size and MAAT showing lack of a significant relationship. (c and d) The relationship between lake size and MAAT is attributed to colder deltas having thicker permafrost, which prevents lakes from connecting to the sub-permafrost aquifer. In warmer deltas, connection to the sub-permafrost aquifer leads to greater lake level change over the summer, driving increased variability in inundation along the peripheries of lakes, and diminishing rates of thermally driven lateral expansion. (e) Scatterplot between the fraction of the periphery of large lakes that remains water on average over the period of record and MAAT shows a weak (i.e., $p = .0527$, bootstrap $p = 0.0551$) linear relationship, supporting the proposed mechanism (c and d).

loss. However, we found that average June-July precipitation minus evapotranspiration (P-ET, i.e., the vertical hydrologic budget) (Bromwich et al., 2018) over the delta is uncorrelated with MAAT, and therefore P-ET does not explain the relationship between delta temperature and how often lake peripheries are inundated (Figure C.6d). This mechanism could be validated in future studies by imaging subsurface permafrost structure across the deltas, which has been done in other lake-rich permafrost environments (Rey et al., 2019).

4.6 Perspectives and Conclusions

By harnessing more than 20 years of remote sensing data over the Arctic, we have developed a methodology to classify waterbodies, depending on their year-to-year variability as lakes (perennial) and wetlands (ephemeral). The statistical distributions of lake and wetland sizes are distinct and appear to be universal across arctic deltas, reflecting the respective underlying mechanisms driving the formation and evolution of those waterbodies. Specifically, it was found that thermokarst lake sizes obey a lognormal distribution, which can be interpreted as the emergent signature of the thermal mechanism driving lake formation and growth. On the other hand, wetland sizes may be described by a power law distribution, which is compatible with landscape inundation models relevant to ephemeral waterbodies (Bertassello et al., 2018; Le & Kumar, 2014). The difference between the underlying forming mechanisms leads also to different expectations with respect to possible relationships with climatic variables. Indeed, our results reveal a significant trend between mean lake size and mean annual air temperature, supporting the hypothesis that colder environments are able to grow and sustain larger thermokarst lakes, while no signature of climate is found in the mean wetland sizes. The power law exponents of the wetland size distributions were found to range between 1.8 and 2.8 (a smaller exponent indicates a thicker tail of the PDF) in line with what has been observed in other regions (Bertassello et al., 2018; Cael et al., 2015;

Le & Kumar, 2014) and further analysis of high-resolution topography is expected to provide additional insight on this range. The decreasing trend of mean lake size with warmer temperatures found here can form the basis for future lake area change projections; however, recognizing that the relationship from the 12 examined deltas, although statistically significant, explains only 40% of the variance and lake change may display significant spatial variability (Chen et al., 2012). These relationships provide some of the first quantification of climate influence on delta morphology along with other recent work on channel network structure (Lauzon et al., 2019; Piliouras et al., 2021). Spatially resolved permafrost depth and ground ice content on the deltas (Rey et al., 2019), as well as analysis of physically based models forced with different climate scenarios (Coon et al., 2019; Overeem et al., 2018) is needed to better understand cause-and-effect and derive relationships that can serve as the basis of projections of landscape change (e.g., increased water ephemerality under warming scenarios) and associated carbon cycle impacts in specific delta environments. Major arctic deltas store approximately 91 ± 39 Pg-Carbon, potentially making them significant sources of future carbon emissions (Schuur et al., 2015), motivating the need for further study of the biogeochemical cycling in these landscapes.

CHAPTER 5

Characterizing lake patterns to understand geomorphologic and climatic processes on arctic deltas

5.1 Introduction

Abundant thermokarst lakes on arctic deltas play an important role in modulating the transport of riverine sediment to the coast and controlling the timescale and transport of nutrients such as phosphorous, carbon, and nitrogen (Cunada et al., 2021; Emmerton et al., 2007; Squires et al., 2009). Thermokarst lakes are formed by the thaw of ice-rich permafrost and are sensitive to climatic drivers; both increasing and decreasing trends in lake cover have been documented depending on local permafrost extent, topography, geology, temperature, and precipitation (e.g., Chen et al., 2013; Nitze et al., 2018; Plug et al., 2008; Rey et al., 2019; Veremeeva et al., 2021).

An additional significant source of uncertainty underlying the observed trends is the flashiness of arctic hydrology which results in seasonal and interannual variability in lake extents. For example, Chen et al. (2012) showed that in the Yukon Flats floodplains, interannual variability in lake extent can be on the same order of magnitude as documented longer-term trends. Later work in the same region showed that floodplain waterbodies exhibit several classes of temporal dynamics, ranging from flashy to perennially inundated, which are hypothesized to be interlinked with permafrost depth (Rey et al., 2019). In a pan-Arctic study, Cooley et al. (2019) also showed varying seasonal change in lake area across four arctic regions of differing geology and climate. Focusing on arctic river deltas, Vulis et al. (2021) controlled for hydrologic variability on each delta by identifying lakes that were perennially inundated over a 20-year period. They found that colder deltas have significantly larger average lake size, which was attributed to a thicker and deeper permafrost layer in colder deltas.

However, extensive analysis of the spatial distribution of lake patterns and dynamics is still lacking. Prior work examining lake cover has generally commented on the distinct geometries and patterns formed by lakes (Figure 5.1; e.g. Grosse et al., 2013), but quantitative insight into spatial distributions of these patterns is lacking. Muster et al. (2019) presented visually distinct spatial patterns of lakes but did not perform extensive analysis of these patterns, only of the lake size distributions. Rey et al. (2019) clustered waterbodies based on their temporal dynamics but did not consider their spatial context. Arp & Jones (2009) documented that the bulk statistics of lake cover, such as the lake density (i.e. the number of lakes per unit landscape area) and lake area fraction (i.e. limnicity, the fraction of landscape area taken up by lakes) varied across regions of Alaska and called for future research into studying the spatial organization of lakes in these specific regions to build process understanding. Recent studies have examined the spatially explicit pattern of lake coverage and dynamics, but only in limited settings. For example, Vulis et al. (2020) showed that on two arctic deltas, summertime lake area shrinkage is inversely related to the distance to the distributary channel network due to an inferred thinner permafrost layer near rivers.

In this study we ask whether there are distinct patterns of lakes within deltas, what controls these patterns, and whether there exist any relationships of lake characteristics to climatic or geomorphic variables. We attempt to answer these questions through analysis of the database of lake cover on 12 arctic deltas introduced in Vulis et al. (2021). We introduce several tools to characterize lake patterns at multiple spatial scales, which offer the potential for physical inference into climate and geomorphic control on lake formation. The study is organized from a top-level bulk statistical characterization of lake patterns towards identification and discussion of specific regions and processes identified across deltas. In section 5.2 we first introduce the study sites and lake database used for lake pattern quantification. In section 5.3 we examine bulk lake cover statistics on each delta, including new information-theoretic based descriptions of the lake size distribution and lake spatial cover, and the relationship of bulk lake cover statistics to climate. In section 5.4, we examine lake distribution through location analysis and show that lakes are non-randomly distributed on the delta planform. In section 5.5, we examine the spatial variability of surface hydrologic connectivity between lakes and discuss implications for deltaic dynamics and for the detection of permafrost. Conclusions are presented in section 5.6.

5.2 Study zones and extraction methods

Twelve deltas across the Arctic which span a range of sizes and climatology were examined (Table 5.1). The selected deltas include those formed by the largest rivers entering the Arctic Ocean by discharge (Mackenzie, Yukon, Kolyma, Lena, Yenisei, and Ob), as well as other significant lake-containing deltas in Alaska (Colville and Kobuk) and Siberia (Pur, Nadym, Yana, and Indigirka). The twelve deltas consist of river-dominated, river-tide, and tidally dominated systems (Table 1; Vulis et al. (in review)). The deltas lay on a gradient of permafrost zonation (Obu et al., 2019), soil ice volume (Brown et al., 1997), and mean annual air temperature (MAAT, estimated from 2000 to 2016, Bromwich et al. (2018)). We use the methodology of Vulis et al. (2021) to extract lakes, wherein lakes were identified by first extracting waterbodies from a year, y^*, with average hydrology (i.e. average water cover) in July, selected to represent post-flood conditions (see Vulis et al. (2021) for details).

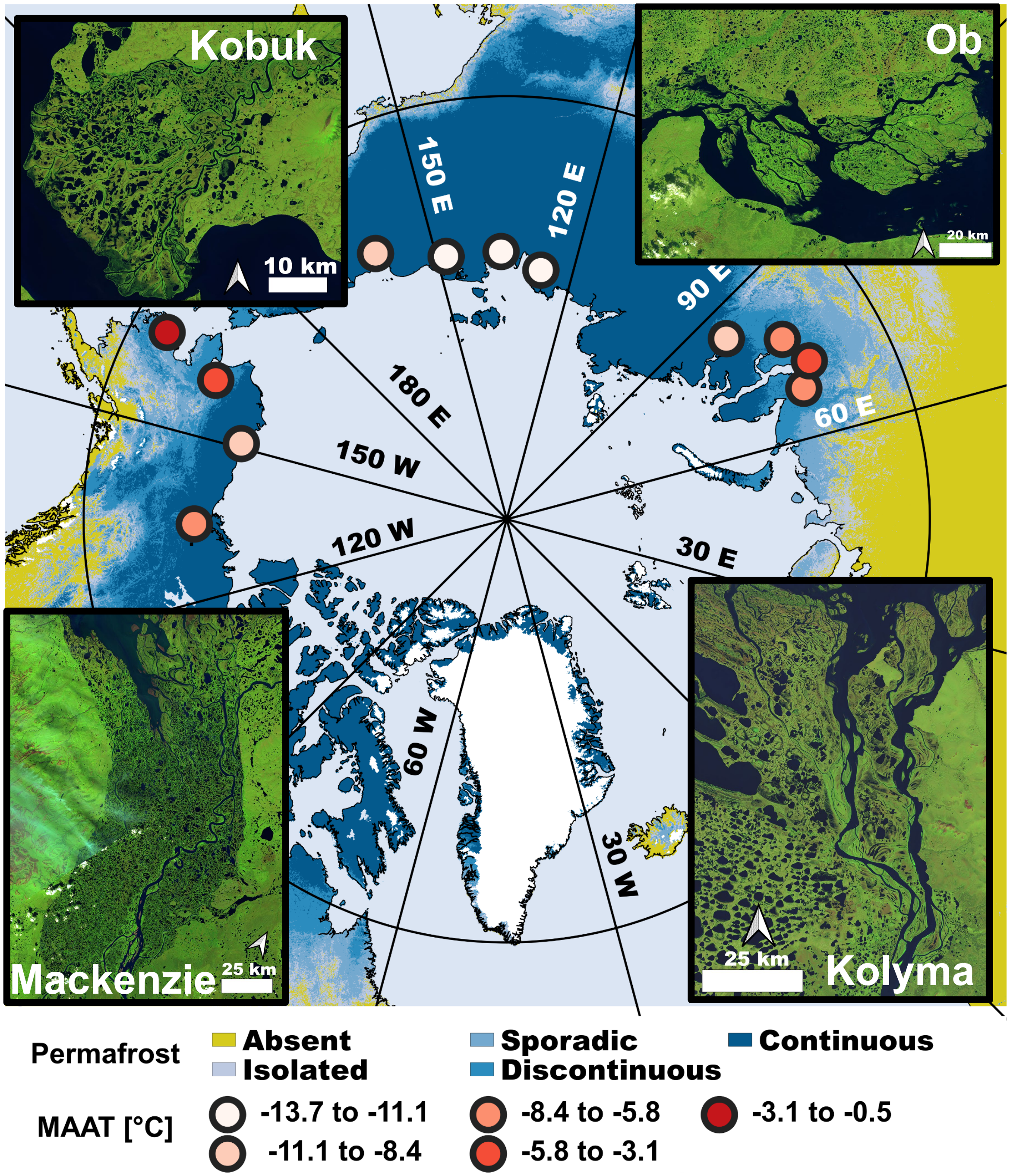

Figure 5.1: **Arctic delta locations and lake patterns**. Map of the twelve arctic deltas under study with examples of lake patterns on four example deltas, after Vulis et al. (2021).

Waterbodies below a minimum mapping unit of $5,400$ m^2 (6 pixels) were not considered for further analysis. Then the July water occurrence, w_i^J, which is defined as the fraction of years over the period of record (1999 – 2018) that a pixel was identified as water in July was computed. For each waterbody identified in y^*, the average waterbody occurrence, i.e. average of w_i^J for all pixels within the waterbody, was computed and then waterbodies were classified as lakes if the average waterbody occurrence exceeded a threshold of 0.85. Note that for two valley-confined deltas, the Nadym and the Pur, we found that water levels stabilized in August rather than July, and therefore we altered the procedure and used August as a reference month. In these deltas, y^* was selected as a year with average hydrology in August and the August water occurrence w_i^A was used for later classification. This led to classification of fewer waterbodies as wetlands and more robust extraction of perennial lake cover. This change in the methodology did not impact the findings of Vulis et al. (2021), namely a significant relationship between mean lake size and MAAT, and the emergent lognormal distribution of lake sizes.

Table 5.1: **Delta climate and geomorphologic properties.** Note that the non-channelized subaerial area of each delta is reported here.

Delta	**Area** [km^2]	**Apex Latitude** [°N]	**Age** [ka]	**MAAT** [°C][7]	**Morphotype**[8]	**Soil Ice Volume**[9]
Yukon	3,900	62.4	2.5 to 5[1,2]	-1.4	River-Tide	medium
Kobuk	1,200	66.9	-	-4.8	River	high
Nadym	2,000	65.6	-	-5.6	Tide	low
Ob	2,900	66.8	3[3]	-5.9	Tide	medium
Pur	2,100	66.5	2.6[4]	-7.2	River	low
Mackenzie	11,600	67.6	14[5]	-7.6	-	medium
Yenisei	6,100	69.6	7[3]	-10.0	Tide	low
Colville	400	70.2	4[6]	-10.5	River	low
Kolyma	2,900	68.7	6.5[3]	-10.8	Tide	high
Lena	13,600	71.9	7[4]	-12.3	River-Tide	high
Yana	8,500	70.8	4[4]	-13.4	River	high
Indigirka	7,400	70.6	6.5[3]	-13.7	River-Tide	high

[1] Dupre & Thompson (1979); [2] Nelson & Creager (1977); [3] Korotaev et al. (2017);
[4] Korotaev (2011); [5] Burn & Kokelj (2009); [6] Jorgenson et al. (1998);
[7] Bromwich et al. (2018); [8] Vulis et al. (in review); [9] Brown et al. (1997)

a Dupre (1979); b Nelson et al., (1979); c Korotaev (2017, in Russian); d Korotaev (2011); e Burn and Kokelj (2009);f Jorgenson et al., (1998); g Bromwich et al., (2018); h Vulis et al., (2023); i Brown et al., 1999

5.3 Assessment of the relationship of lake cover properties with climate

5.3.1 Standard Statistics

As thermokarst lake formation is driven by the thaw of ice rich permafrost, we first asked whether there is a climate signature on bulk lake coverage. Two common bulk lake cover statistics that are typically used are lake density and lake areal fraction (also known as limnicity; Grosse et al. (2013)). Lake density is defined as the number of individual lakes (N_L) over the non-channelized area of the subaerial delta A_{delta}. The lake area fraction is defined as the fraction of non-channelized delta area taken up by lakes (i.e total lake area, $A_{L,T}$, over A_{delta}). Both metrics are computed with respect to non-channelized delta area such that variation in channelized area between deltas does not influence the values of the metrics.

We observe that the Mackenzie appears as a significant outlier in terms of lake density and lake area fraction (Figure 5.2a, circled point). We hypothesize that it may be an outlier because it formed while draining the margins of the thawing Laurentide ice sheet (Burn & Kokelj, 2009), which may have led to large inputs of silts especially when compared with the other deltas which were not immediately downstream of thawing glaciers. This unique deglaciation history contributes to an estimated initial progradation age of $14,000$ years ago, compared with estimated ages of less than $8,000$ years for the remaining deltas (Table 5.1). This combined increased progradation time with higher levels of silt may have led to preferential conditions for the growth of the abundant thermokarst lakes observed on the

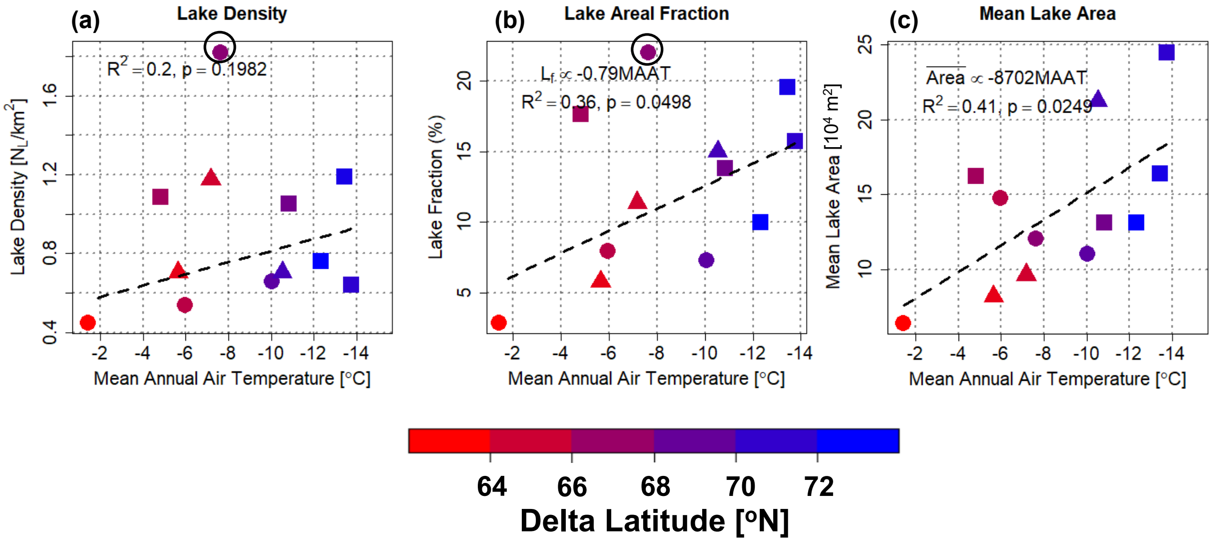

Figure 5.2: **Bulk lake cover statistics on arctic deltas.** (a) Lake density, i.e. number of lakes per unit delta island area, shows no relationship with climate and the Mackenzie delta (MAAT = −7.6°C, black circle) appears as an outlier. (b) Lake area fraction, i.e. fraction of delta area taken up by lakes shows a significant increase in colder systems, when excluding the Mackenzie delta. (c) The mean lake area to climate trend as reported in Vulis et al. (2021) which suggests that lake area fraction (b) increases due to the presence of larger lakes. Figure 2.

modern delta.

Even when excluding the Mackenzie from a regression analysis, we find no statistically significant relationship between climate, represented by MAAT, and lake density (Figure 5.2a, $R^2 = 0.2$, $p = 0.1982$). However, we do observe a weak relationship between climate and lake areal fraction when excluding the Mackenzie (Figure 5.2b, $R^2 = 0.36$, $p = 0.0498$). As there is no relationship between climate and lake density (Figure 5.2a), the weak relationship of lake area fraction with climate may be driven by the presence of larger lakes, which would be supported by the previously reported trend in mean lake area to MAAT (Figure 5.2c). We also found that when not including the Kobuk delta (MAAT = -4.5°C), there is a significantly stronger relationship ($R^2 = 0.7$, $p = 0.0028$) between climate and lake area fraction. Although the Kobuk delta also appears to be an outlier in terms of lake density and lake area fraction, there is no strong physical motivation for why this delta should be excluded.

5.3.2 Information Theoretic characterization of lake cover

Although lake density and lake area fraction are commonly used measures of lake spatial coverage, they provide limited information about the lake cover on a delta as they do not reflect information about lake size heterogeneity. To illustrate this point, we show in Figure 5.3 four panels where each panel has an identical number of lakes (10), lake area fraction (0.1), density (0.03 lakes / m^2), and mean lake area (30 m^2), but each configuration has a different lake size distribution, which could be a signature of process. To overcome these limitations and account for both lake size and their number, we propose a novel set of information-theoretic lake cover metrics, inspired from newly developed metrics of braided river geometry (Dong & Goudge, 2022; Tejedor et al., 2022) and which can capture lake diversity and provide additional information on lake patterns.

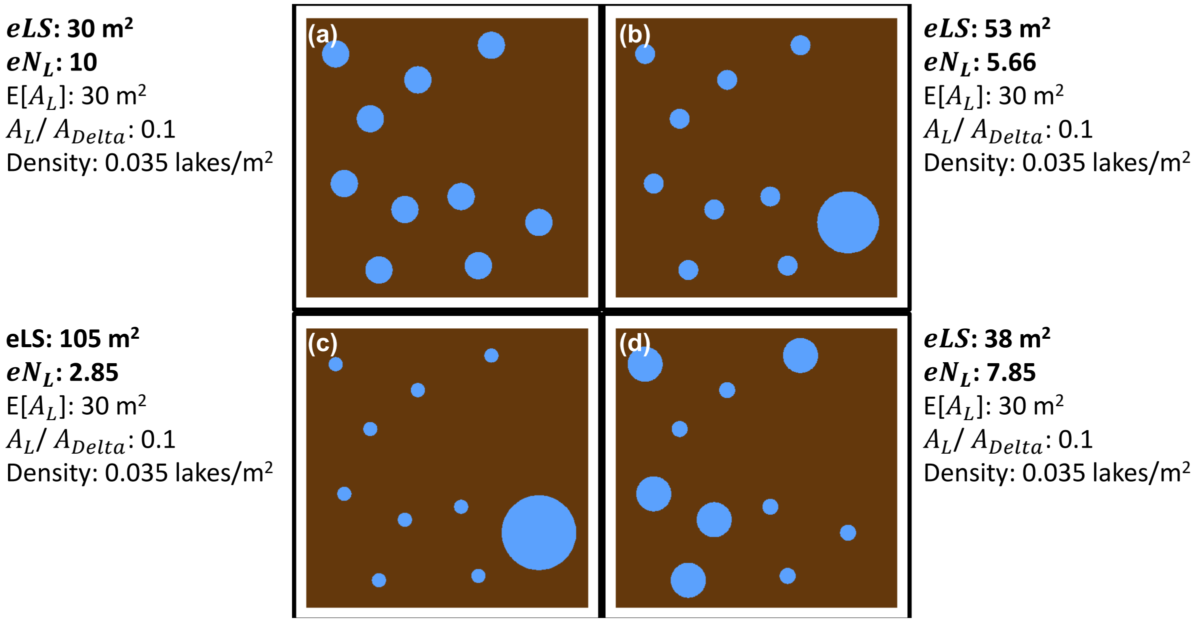

Figure 5.3: **Information theoretic metrics of lake cover.** Every panel shows lakes (blue) on land (brown) with identical lake area density (0.035 lakes per m^2), lake area fraction (10%), and mean lake area (30 m^2), but visually distinct patterns. We introduce an effective lake count, eN_L which is based on the entropy of the lake size distribution, and utilize it to compute an effective lake density(eN_L/A_{delta}) and effective lake size (eLS), which distinguish the above patterns.

Specifically, Tejedor et al. (2022) introduced an entropic Braided Endex (eBI) to characterize at the section of a multi-threaded river both the number of channels and the heterogeneity in their widths. Drawing on their approach and applying it to lakes, we propose an effective number of lakes, eN_L, and then define several metrics based on this quantity. The effective number of lakes, eN_L, is derived below by conceptualizing a stochastic process based on the lake pattern and then computing the Shannon Entropy of the process.

Consider randomly selecting a water pixel from a given panel in Figure 5.3. The probability of selecting a pixel belonging to a specific lake i is given by the area of the lake, $A_{L,i}$, normalized by the total lake area $A_{L,T}$, i.e. $p_i{=}A_{L,i}/A_{L,T}$. The stochastic process defined here has potential outcomes equal to the number of lakes, N_L, with each outcome having probability p_i. When the lakes are of equal size, every outcome is equally likely, i.e. the randomly selected pixel could belong with equal probability to any of the lakes (Figure 5.3a). When the area of one lake is significantly larger than the others, it is much more likely that the randomly selected pixel will fall on that lake compared with any other lake (Figure 5.3c).

This comparison can be alternatively cast by considering how surprising the outcome of the process is. In Figure 5.3c we are less surprised when the pixel lands in the large lake and more surprised if it lands in one of the small lakes, while in Figure 5.3a it is equally surprising for the pixel to land in any of the lakes. This intuitive notion of surprise is mathematically defined for any individual outcome i as $-\log_2 p_i$. Note that when an outcome takes place with probability 1, i.e. there is only one lake, then the surprise is equal to zero as the pixel will always be chosen from that lake. Then to compare lake distributions, we compute the expected value of the surprise of the process, which is known as the Shannon Entropy, H (Eqn. 5.1); Cover & Joy (2006). See Tejedor et al. (2022) and references therein for examples of the entropy used in a geomorphic context.

$$H = -\sum_i p_i \log_2 p_i = -\sum_i \frac{A_{L,i}}{A_{L,T}} \log_2 \frac{A_{L,i}}{A_{L,T}} \tag{5.1}$$

For a given number of lakes, the entropy is maximal when the probability of the randomly selected pixel falling in any lake is equal, i.e. when all lakes have the same size, and decreases when lake sizes are heterogeneous. For example, for the 10 lakes shown in Figure 5.3a $H = 3.32$. For heterogeneous lake size distributions, e.g. Figure 5.3c, where the large lake has an area 30 times larger than any of the other equal-sized lakes, the entropy is 1.51, that is, the average surprise is much lower in Figure 5.3c compared with Figure 5.3a. To transform the entropy into a more readily interpretable quantity, we consider what is the equivalent number of lakes of equal size that would yield exactly the same entropy as the observed distribution, which we define as the effective number of lakes, eN_L (Tejedor et al., 2022). The eN_L is computed via Equation 5.2:

$$eN_L = 2^H \tag{5.2}$$

As was argued by Tejedor et al. (2022) when introducing the entropic braiding index, the eN_L captures the intuitive notion of an effective count of the lakes. For example, in Figure 5.3c, the effective number of lakes is just under 2.85, while in Figure 5.3d it is 7.85, which reflects the predominance of the larger lakes in the pattern.

5.3.3 Entropic Metrics

Based on the effective number of lakes, eN_L, we propose three metrics of the lake size distribution and lake spatial cover. We evaluate these metrics at the delta scale below and show their utility at evaluating heterogeneity in deltaic lake patterns.

Lake Size Homogeneity

By definition, when every lake has the same exact size, eN_L equals N_L (Figure 5.3a) and eN_L decreases as lake sizes become more heterogeneous. Therefore, the ratio of eN_L

to N_L measures the homogeneity of lake sizes. The ratio approaches 1 when lakes are all the same size, i.e. the pattern is composed of homogeneous lakes, and tends towards zero as eN_L decreases, i.e. the pattern is composed of heterogeneous lakes (Figure 5.3). This is similar to the channel heterogeneity metric proposed by Tejedor et al. (2022) and to entropic diagnostics for evaluating landscape regionalizations (Nowosad & Stepinski, 2018).

We do not find that lake size homogeneity linearly depends on climate (Figure 5.4a), but rather, that three groups of deltas emerge: very cold, heterogeneous systems (Kolyma, Yana, Indigirka), a cold, relatively homogenous system (Yenisei), and the remainder of the deltas which have intermediate homogeneity. For the very cold systems this arises because there are abundant small lakes, a possible signature of early-stage lake growth, along with very large, coalesced lakes, a signature of late-stage lake growth. On the Yenisei there are relatively no large, coalesced lakes leading to more overall homogeneity, which may be a signature of more uniform soil ice volume and intermediate stage lake growth. This suggests that differences in the heterogeneity of lake sizes may be a signature of geologic variability or lake growth history.

Effective Lake Size

We define an effective lake size, eLS as the total lake area divided by the effective number of lakes (Equation 3).

$$eLS = A_{L,T}/eN_L \tag{5.3}$$

Note that the effective lake size of a lake pattern has as a lower bound the mean lake size, but becomes larger than the mean as the lake sizes become more heterogeneous and the eN_L decreases. For arctic deltas, we find that colder deltas have significantly larger eLS, which aligns with the previously reported relationship between climate and mean lake size. We observe that the climate trend with eLS is steeper than the climate trend with mean lake area, which we attribute to the presence of large coalesced lakes in the very cold deltas which leads to more heterogeneity and a higher effective lake size. This explanation aligns with the proposed mechanism for the climate relationship, namely that generally colder permafrost allows for the growth and support of larger lakes on colder deltas (Vulis et al., 2021).

Effective Lake Density

Finally, we define an effective lake density as the effective number of lakes per unit area, analogously to the lake density.

$$eLD = eN_L/A_{delta} \tag{5.4}$$

This metric is less sensitive than the lake density to the presence of abundant small lakes whose count is sensitive to the satellite resolution used to extract lakes. For example, increasing the minimum mapping unit from $5,400$ m^2 (6 pixels) to $18,000$ m^2 (20 pixels) on the Yana decreases the lake density from 1.19 lakes per km^2 to 0.8 lakes per km^2, but only decreases the effective lake density from 0.23 to 0.21 effective lakes per km^2.

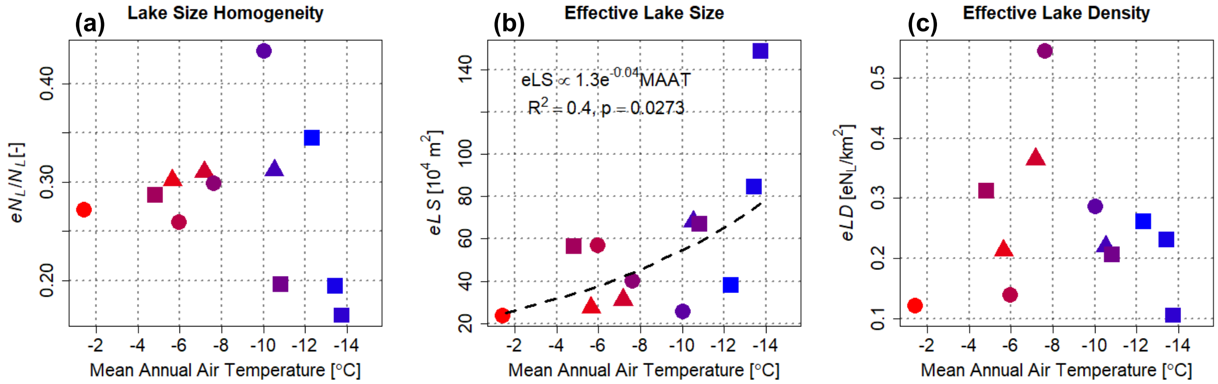

Figure 5.4: **Entropic measures of lake size distribution and coverage.** (a) Lake size homogeneity is given by the ratio of the effective number of lakes to the number of lakes and shows no relationship with temperature, instead highlighting 3 groups of deltas: low, intermediate, and high homogeneity. (b) The effective lake size shows a positive trend with temperature corroborating that colder deltas have greater lake coverage associated with larger lakes. (c) The effective lake density shows no relationship with temperature and the Mackenzie has significantly larger effective density than any other delta highlighting its uniqueness. Colorbar is same as in Figure 5.3

We observe that there is no relationship between effective lake density and temperature and we also note that the Mackenzie stands out as having a much larger effective density than any other delta. This further suggests that even when controlling for heterogeneity, the Mackenzie is a delta that is unique in terms of lake coverage compared with most other systems. Caution should therefore be taken when extrapolating field measurements and physical inference performed in this system to the broader group of arctic deltas.

5.3.4 Discussion on delta-scale entropic metrics

We presented the three entropic metrics as an intuitive set of easily computable quantities to characterize lake cover in the face of heterogeneity, with broad applicability outside arctic deltas. Application to lake distributions on arctic deltas yielded insight into permafrost process and lake formation history on the deltas. Specifically, we found that deltas group into 3 levels of differing lake size homogeneity. The separation between the low and high homogeneity systems is attributed to distinct stages of lake growth in these deltas. We also observed a steeper relationship between effective lake size and temperature than between mean lake size and temperature, which is attributed to the presence of large coalesced lakes in the very cold deltas that the eLS captures. Lastly, we do not observe a relationship between effective lake density and climate, supporting that it is an increase in lake size and not abundance that is observed in the lake area fraction with climate relationship (Figure 5.2). We note that the metrics are computed over the entire delta but can also be used to compare heterogeneity of subregions within a delta or to track temporal variability in lake size distribution.

5.4 Lake Spatial Distribution

Having quantified the bulk characteristics of the lake distributions using both traditional and entropic measures, we now turn to analysis of the spatial distribution of lakes. Specifically we expect that lake locations will contain information on soil ice volume and permafrost degradation state, as lakes grow as the result of ice-rich permafrost degradation and that ice-rich permafrost is hypothesized to grow only after complete channel abandonment and cessation of flooding (Jorgenson et al., 1998). Visual inspection of the deltas does in fact suggest the appearance of patterns in lake cover. To determine whether these patterns are in fact significant, we tested whether lake locations exhibit clustering or whether lakes are distributed according to complete spatial randomness (Diggle, 2013). We use a distance-based approach, wherein we test if the observed probability distribution function (PDF) of inter-lake distances is significantly different than the PDF of inter-lake distances under complete spatial randomness. To measure the inter-lake distance we introduce the concept of lake neighborhood distance.

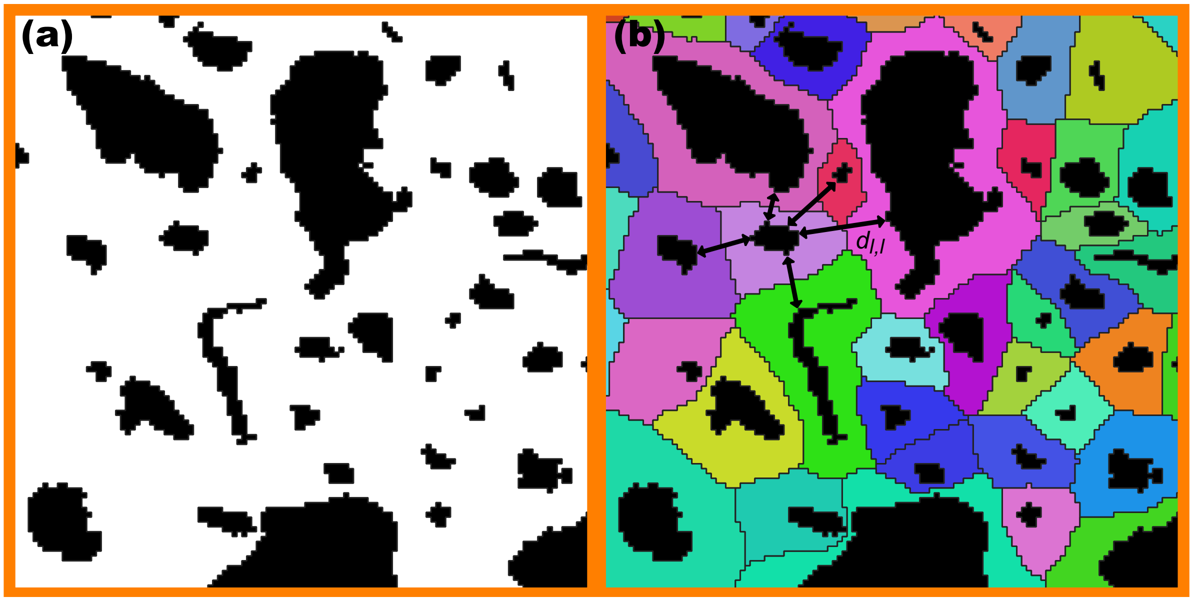

Figure 5.5: **Defining a lake neighborhood distance.** (a) Section of real lakes (black) on the Yana delta. (b) Generalized Voronoi tessellation (Okabe et al., 2000) in arbitrary colors, after which distances between lakes which share a Voronoi boundary are measured. The full geometry of each lake is used to generate the Voronoi tessellation.

5.4.1 Lake Neighborhood Distance

The distances between individual spatial geometries such as lakes or islands are typically approximated by the centroid-to-centroid distance of each object (Diggle, 2013). However due to the multiscale nature of lake sizes, presence of irregular and non-convex lake shape, and the dissection of the spatial domain by the channel network, such an approximation excludes important information. Moreover, the centroid of non-convex lake geometries is not necessarily contained within the lake, making this approximation difficult to interpret. Therefore, we measure lake to lake distances explicitly as the minimum distance between shorelines of two lakes, which is relatively fast to estimate using computational geometry algorithms implemented in a geographic information system (e.g. Pebesma (2021); see Figure 5.5).

Typically, the distance distribution considered for each i^{th} lake is either the nearest neighbor distance or the average or max distance to its k closest neighbors, where k is fixed. By construction, the nearest neighbor distance lacks information on the distance to most neighboring lakes, which can limit further interpretation of its value, so it is preferable to use the distance to the k closest neighbors. Then consider that the number of adjacent lakes which can fit adjacent to a given lake scales positively with the size of the lake, as very large lakes can have more close neighbors, while very small lakes can have few neighbors. Further consider that the distance between two distant enough lakes is necessarily influenced by whether additional lakes lie between them. It is therefore desirable to adjust k depending on lake size such that a scale-appropriate neighborhood can be defined.

To address these considerations, we introduce the notion of the neighborhood of a lake through the Voronoi tessellation of the lakes (Okabe et al., 2000) and then measure the average distance to its neighbors. The Voronoi tessellation is an exhaustive partition of a spatial domain which marks every point in the domain with its nearest lake and encloses the marked areas in a polygon (Figure 5.5). Note that to identify the nearest lake, the full geometry of each lake is utilized, not just the centroid of each lake, which is known as a generalized Voronoi tessellation (Okabe et al., 2000). To account for the dissection of landscape by channels which impose a necessary separation of lakes from one another, we treat the entire channel network as a single "lake" when generating the tessellation, but discard it from further analysis.

For every lake, its neighborhood consists of the q lakes with which it shares a side in the Voronoi tessellation. Note that q changes from lake to lake and is a property of the underlying spatial distribution of lakes. Finally for every lake l, we define its neighborhood distance $d_{l,l}$, as the average lake to lake distance $d_{l,j}$, from lake l to its $j = 1 \ldots q$ neighbors, including the channel if the channel is a neighbor. We then computed the distribution of $d_{l,l}$ for all lakes in each delta.

5.4.2 Non-randomness of lake locations

To determine whether the lake patterns contain statistically significant clusters of closely packed lakes, for a large number of iterations (100) we reshuffled the real lakes on each delta and recomputed the distribution of $d_{l,l}$ in each reshuffling (Figure 5.6). In order to ensure completion of the reshuffling, lakes were placed on the landscape from largest to smallest.

We found that lakes on arctic deltas exhibit clustering, as indicated by the higher coefficient of variation, i.e. lower mean and higher standard deviation, in the distribution of $d_(l,l)$ compared with complete spatial randomness (Figure 5.6). Curiously, most real deltas exhibit a constant coefficient of variation and therefore a similar degree of clustering across deltas. However, the Nadym delta exhibits significantly higher clustering of lakes than any other deltas, which we explore further in sections 5.4.3 and 5.5.

5.4.3 Densely and coarsely packed lakes

The clustering of lake locations indicates that lakes on arctic deltas contain information on the processes which form them, however the probability distributions in Figure 5.6 do not identify where these clusters are. Due to the statistical concerns of identifying areas of significant lake clustering in the presence of interchannel islands, on each delta we simply identify zones of dense and coarse packing as lakes with neighborhood distances below the 25^{th} percentile and above the 75^{th} percentile of that delta's $d_{l,l}$ PDF, respectively, and use those to locate areas in terms of revealing information about process.

Spatially contiguous zones of densely packed lakes are observed on multiple deltas (Figure 5.7) and appear to correspond to process similarities across deltas. For example, on the Yana, a 15-km wide marine zone is characterized by densely packed lakes stretching along the seaward perimeter of the delta. This zone runs adjacent to the coastal delta and is also

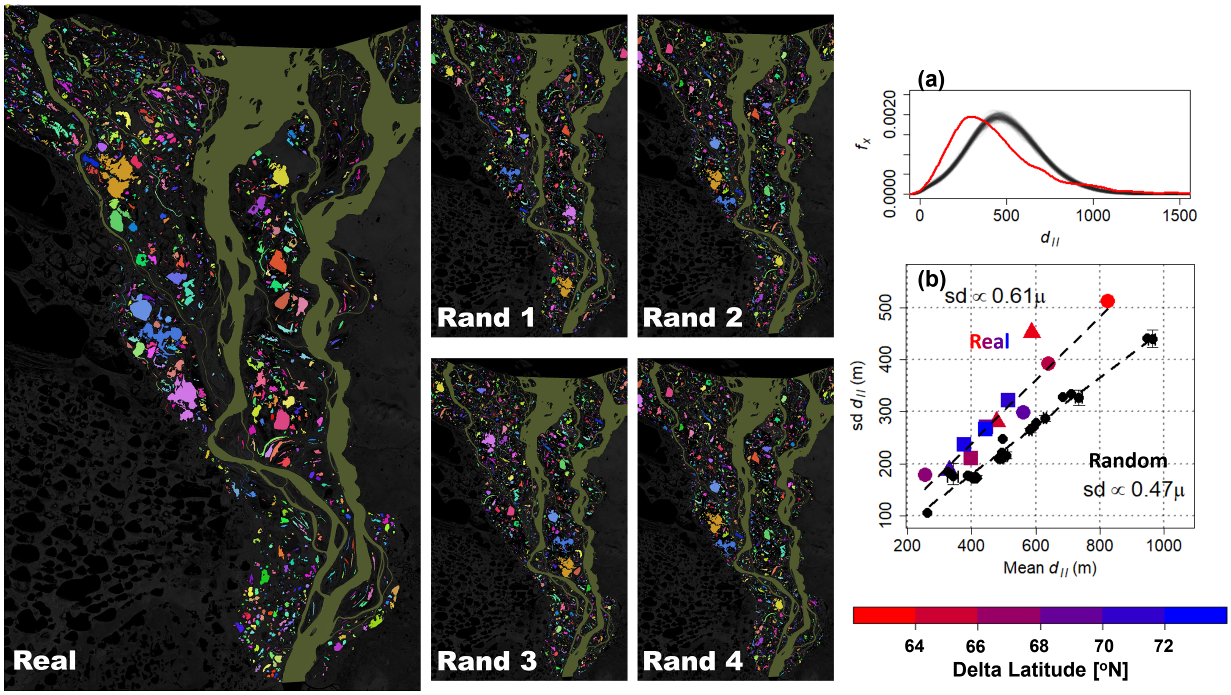

Figure 5.6: **Non-random lake locations on major arctic deltas.** The real lake distribution of the Kolyma delta is shown along with 4 examples of the randomly reshuffled lakes, with each lake having a unique, random color. (a) The probability density function (PDF) of the lake neighborhood distance for 100 reshufflings (black) compared with the true neighborhood distance PDF (red), with significantly smaller mean and larger standard deviation in the real lakes. (b) On every delta, lakes exhibit clustering as evidenced by a larger coefficient of variation (slope) of the observed distance distributions compared with the reshuffling. The Nadym (triangle) has a coefficient of variation equal to 0.77, indicating greater clustering than any other delta.

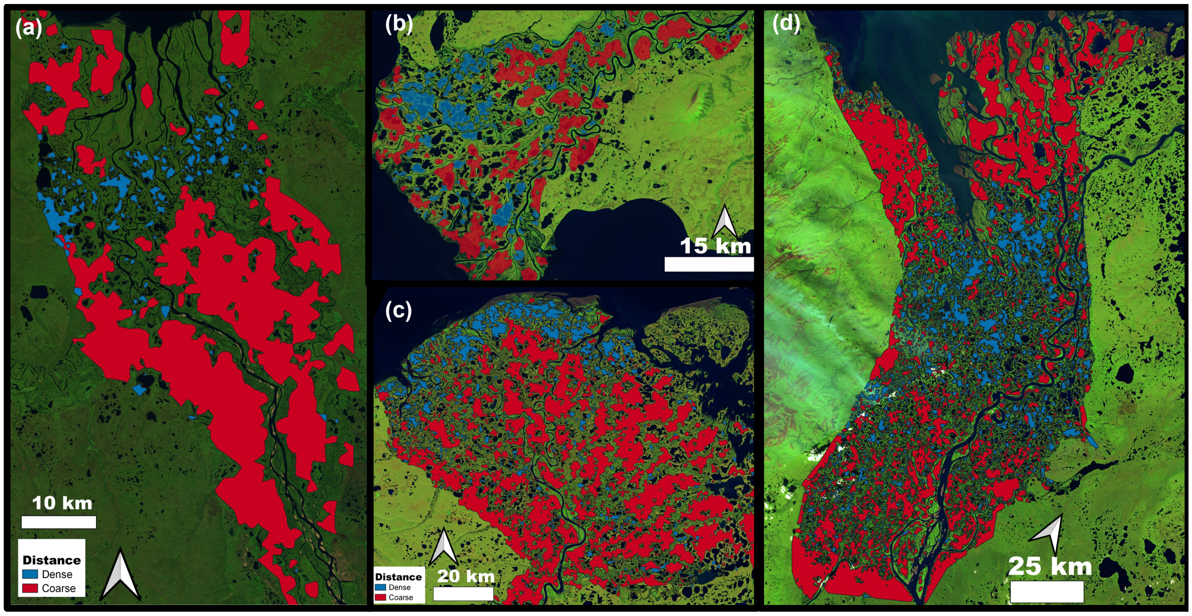

Figure 5.7: **Densely and coarsely packed lakes.**Spatially cohesive zones of densely packed lakes can be observed on the (a) Nadym, (b) Kobuk, (c) Yana, and (d) Mackenzie.

observed on the Indigirka and Kolyma deltas. In all 3 deltas, these densely packed lakes are characterized by an eLS between 28% to 47%of the delta-wide eLS, while coarsely packed lakes are significantly larger than densely packed lakes (Figure 5.8). Visual inspection of the marine zone with high-resolution imagery available via Google Earth shows abundant circular lakes at or below the Landsat resolution amidst high centered polygonal tundra, suggesting this zone is characterized by highly degraded permafrost.

Although relationships in lake size and spacing are observed in these three deltas, there is not a general monotonic relationship between the two across deltas, and there is not a clear correspondence between size, spacing, and permafrost process. For example, a similar spatially cohesive zone of high packing and small lakes is observed in the Nadym delta but $12 - 15$ km upstream of the shoreline (Figure 5.7a), while lakes are particularly sparse in the floodplains upstream. However visual inspection shows that in areas of extensive inundation during periods there is no evidence for polygonal tundra, suggesting a lack of existing permafrost. The Kobuk and Mackenzie are also characterized by spatially contiguous zones of densely packed lakes in the lower delta, but densely packed lakes are similar in size

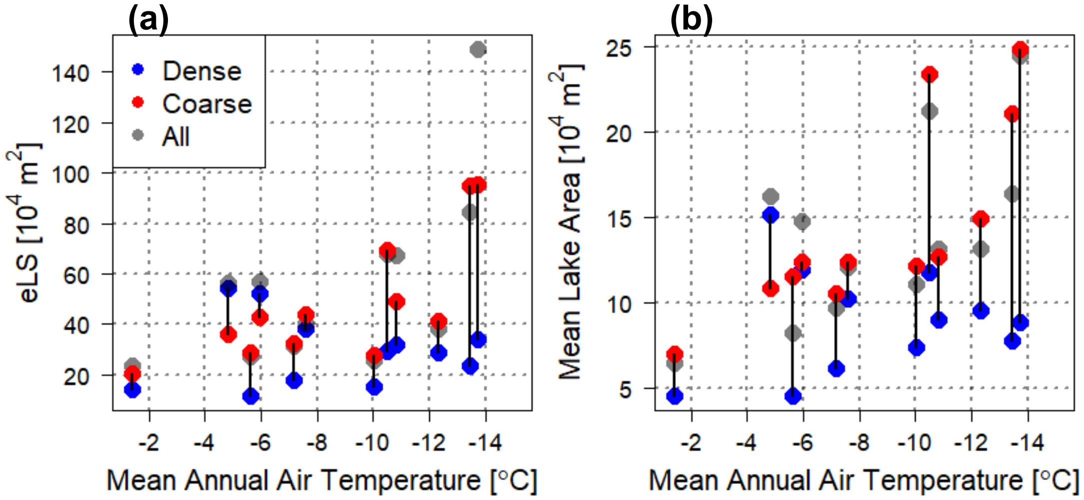

Figure 5.8: **Lake sizes in densely and coarsely packed zones.** The eLS (a) and mean lake size (b) in the densely packed zones (blue) and coarsely packed zones (b). Bars indicate pairs of points corresponding to a single delta. Densely packed lakes range from being significantly smaller (e.g. Yana, Indigirka) to larger (Kobuk) than coarsely packed lakes.

to all lakes, and not significantly smaller. On the Kobuk, densely packed lakes are even larger than coarsely packed lakes, i.e. the relationship between size and spacing is reversed. Lastly, large blocks of spatially cohesive densely packed lakes are not observed on all deltas, e.g. on the Yenisei. Further information is necessary to make physical inference on the drivers of these patterns. Given that arctic deltas have extremely variable surface hydrology driven by snowmelt and flooding, a likely source of additional useful information is the hydrologic connectivity of the lakes on the landscape. This hydrologic connectivity is examined in the next section.

5.5 Incorporating hydrologic connectivity

The lakes identified in this study are by definition perennially inundated and disconnected during low-water, end of summer conditions (i.e. in August or July). However, due to fluvial flooding, localized snowmelt, or precipitation events, these perennial lakes may have surface water connections by ephemeral channels or low-relief between the lakes, e.g. due to a hierarchical depression structure from a drained thaw lake basin (see insets in Figure 5.9). Identifying surface water connectivity between lakes can yield insight on delta hydrology and lake storage, as well as reveal where there is extensive permafrost degradation, as inundation inhibits permafrost growth and thaws existing permafrost (Zhang et al., 2023).

5.5.1 Detecting surface water connections between lakes

To detect lakes which may have surface water connectivity under wet conditions, we use the same Global Surface Water (Pekel et al., 2016) water masks used for the extraction of lakes. We first compute the water pixel occurrence for June through August, i.e. the fraction of total time a pixel was classified as water in those 3 months over the 20 year period of record, w_i^{JJA} (Figure 5.9). Then, we identify wet regions, defined as contiguously connected areas which have experienced inundation ($w_i^{JJA} > 0$) during the period of record. Lastly, we identify lake complexes (LC) as wet regions which contain 3 or more perennial lakes (which were extracted based on the methodology detailed in Section 5.2).

5.5.2 Spatially variable hydrologic connectivity on deltas

Lake complexes reveal both heterogeneity in hydrologic connectivity within deltas and similarities across deltas, offering insight into the permafrost presence on each delta. To generally compare hydrologic connectivity on each delta we report (a) the percentage of lake area contained within LCs and (b) the fraction of subaerial delta area taken up by the Voronoi polygons associated with lakes within LCs (Figure 5.10). By both measures the Yana, Yukon, and Lena have the lowest hydrologic connectivity of any delta, while the Kobuk, Pur, Mackenzie, and Kolyma have among the highest hydrologic connectivity. This lack of

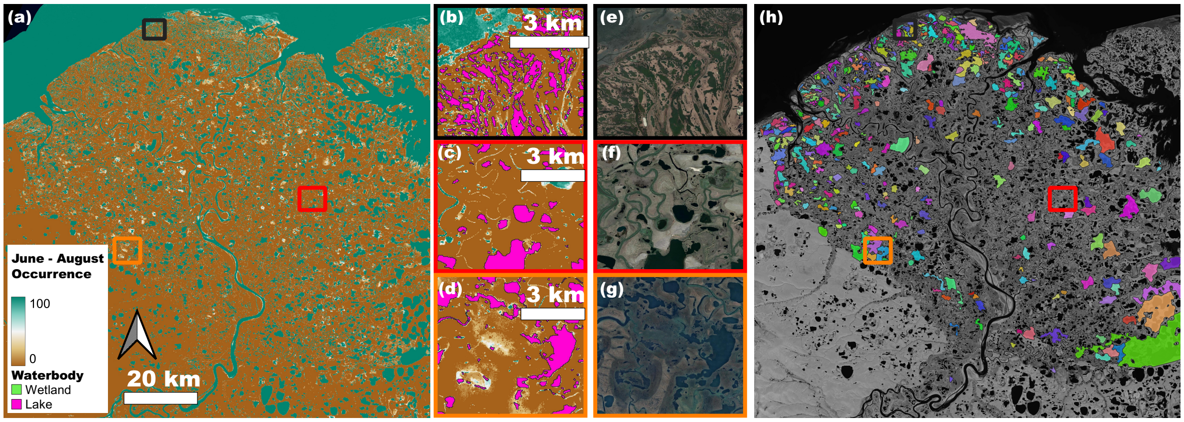

Figure 5.9: **Lake Complex (LC) identification.** (a) Map of June to August water pixel occurrence, w_i^{JJA}, which is used to identify wet regions, i.e. contiguous regions which have ever experienced inundation ($w_i^{JJA} > 0$). (b-d) Highlights of lakes with varying levels of hydrologic connectivity, along with high-resolution satellite imagery available via Google Earth (e-g). (h) Wet regions containing at least 3 lakes (as previously identified) are termed lake complexes and are shown in arbitrary colors, with a high density of LCs in the marine zone and in a likely yedoma-impacted zone in the southeastern portion of the delta.

hydrologic connectivity can be seen on the Yana (Figure 5.12), where lake complexes are observed primarily in the marine zone and near large circular and coalesced lakes in the southeastern part of the delta. On the Kolyma and Kobuk large fractions of the delta are occupied by LCs (Figure 5.12). Interestingly, although the Nadym (red triangle in Figure 5.6) has a large fraction of hydrologically connected lake area, these hydrologically connected lakes do not constitute a majority of the landscape as in other systems (Figure 5.10b).

A general mechanism explaining the origin of the underlying differences in hydrologic connectivity between deltas was not found. One hypothesis is that valley confined deltas such as the Pur experience more spatially extensive flooding compared with progradational deltas such as the Yukon or Lena as spring floodwaters are confined and are therefore more likely to overtop on islands. However, counterexamples to disprove this hypothesis are found in the Indigirka, which is progradational and shows high hydrologic connectivity and the Yenisei which is valley-confined but has low hydrologic connectivity. A second hypothesis is that increased hydrologic connectivity is driven by shallower local relief among lakes but given that the ArcticDEM has uncertainty in flat landscapes on the order of local relief

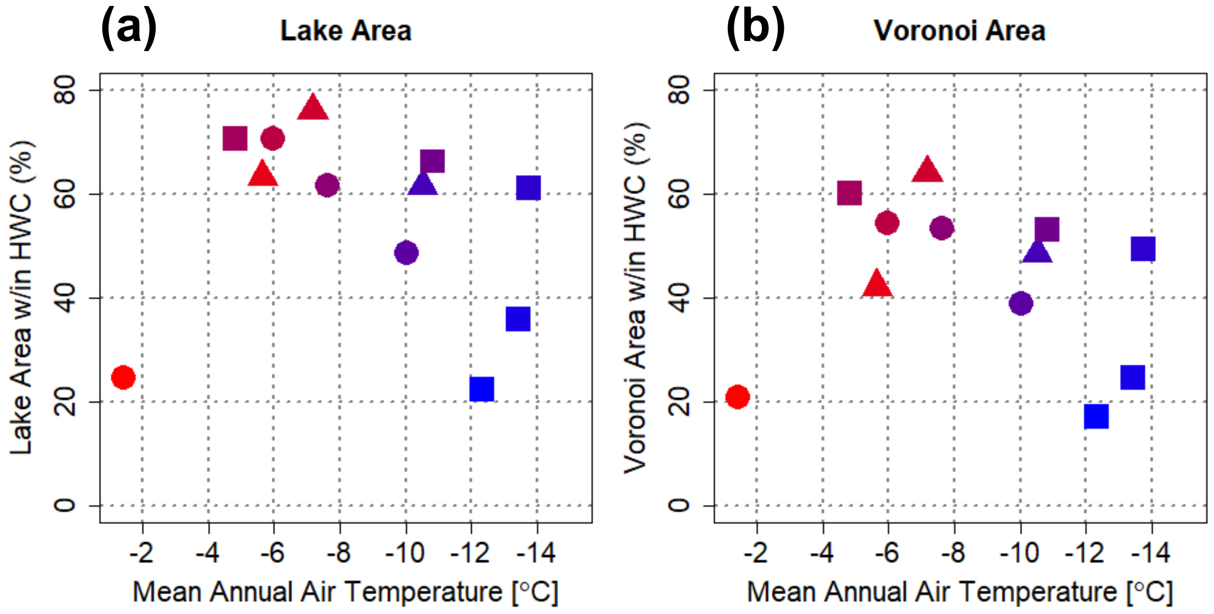

Figure 5.10: **Hydrologic connectivity on each delta as measured by LC statistics.** (a) The percent of lake area present within lake complexes (LCs) and (b) the percent subaerial delta area taken up by LCs for each delta. Neither measure shows a relationship with temperature, suggesting hydrologic connectivity is reflective of local geomorphic process control, not climate. Colorbar is same as in Figure 5.3.

(decameters) and does not control for landscape inundation when retrieving elevation (Porter et al., 2018), we cannot robustly test this hypothesis.

5.5.3 Delta process zones and projected vulnerabilities

Across deltas, the distinct spatial patterns of the lake complexes and associated lake distances and sizes reflect differences in hydrologic processes present on the deltas (Figure 5.13). For example, ephemeral channels activated during spring fluvial flooding or snowmelt are observed on the Kobuk and Indigirka. These suggest that those sections of the delta are able to drain after flooding events. As such ephemeral connectivity between the DCN and lakes can control lake biogeochemistry and the form and magnitude of carbon released into the atmosphere from lakes (Squires et al., 2009), detecting these ephemeral channels can help inform future work on improving deltaic atmospheric carbon emission estimates.

Another common feature across all deltas is the presence of hierarchical depression structures. These hierarchical depressions can correspond to drained thermokarst lake basins (DTLB) or degrading high centered polygonal tundra connecting multiple existing lakes. DTLBs typically consist of several small lakes surrounded by areas of intermediate occurrence, indicating areas of temporary surface water storage. The existence of DTLBs is a signature of extensive ice-rich permafrost development which was able to form large lakes and then drained. This suggests that these areas of the delta have rarely experienced fluvial flooding which would degrade the permafrost (Stephani et al., 2020) and that these areas of the delta are relatively old. The presence of the DTLBs also suggests a lack of active fluvial reworking after drainage which would erase these features from the surface. Further research on arctic deltas focus on detecting these drained thaw lake basins using auxiliary information but the analysis of the spatial distribution of these features is beyond the goal of this study which focuses on characterizing perennially inundated lakes.

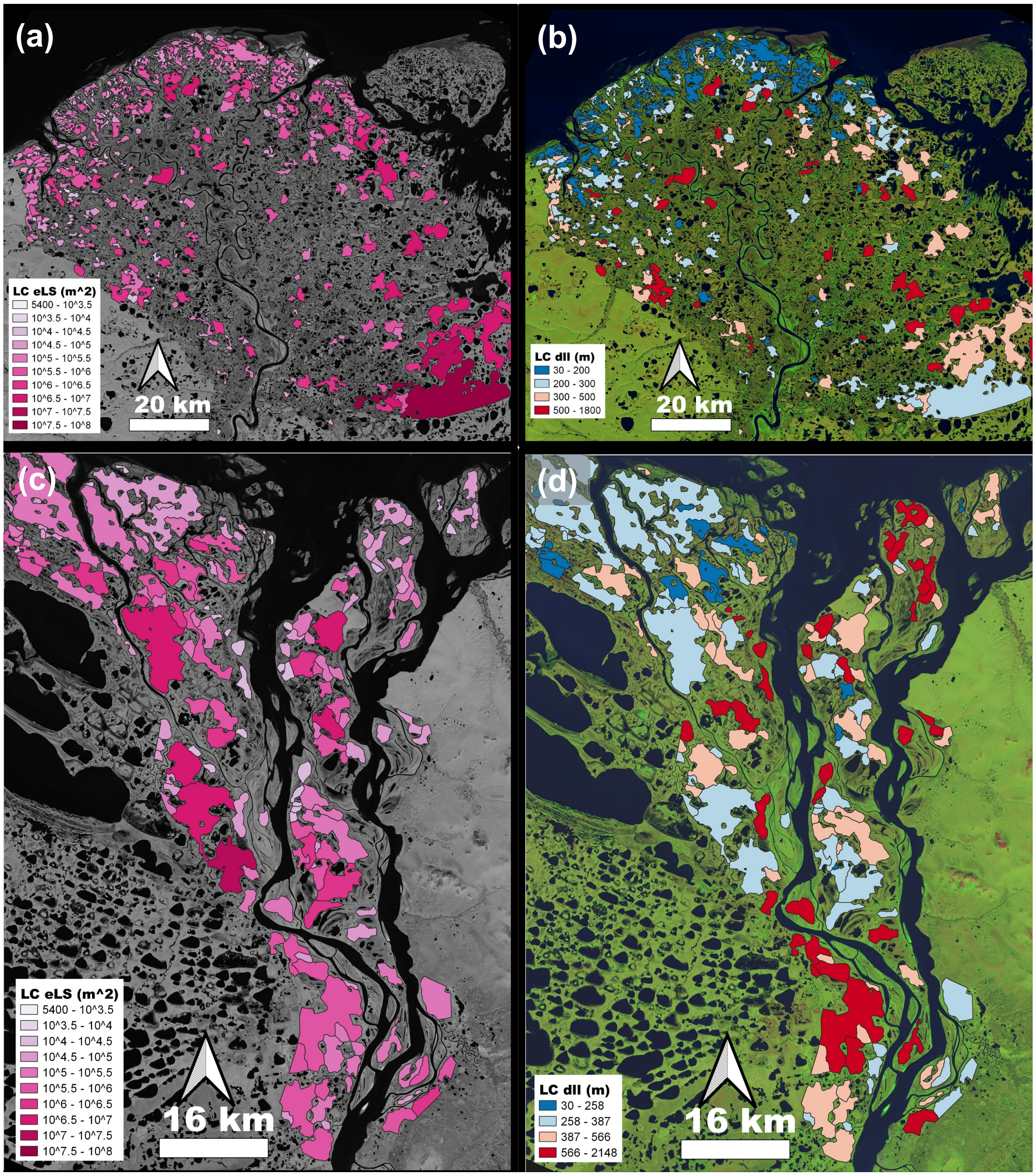

Figure 5.11: **Lake complexes on the Yana and Kolyma deltas.** (a, b) Lake complexes on the Yana delta colored by (a) the eLS of lakes in each LC and (b) average neighborhood distance of lakes in each LC. (c, d) The same maps for the Kolyma.

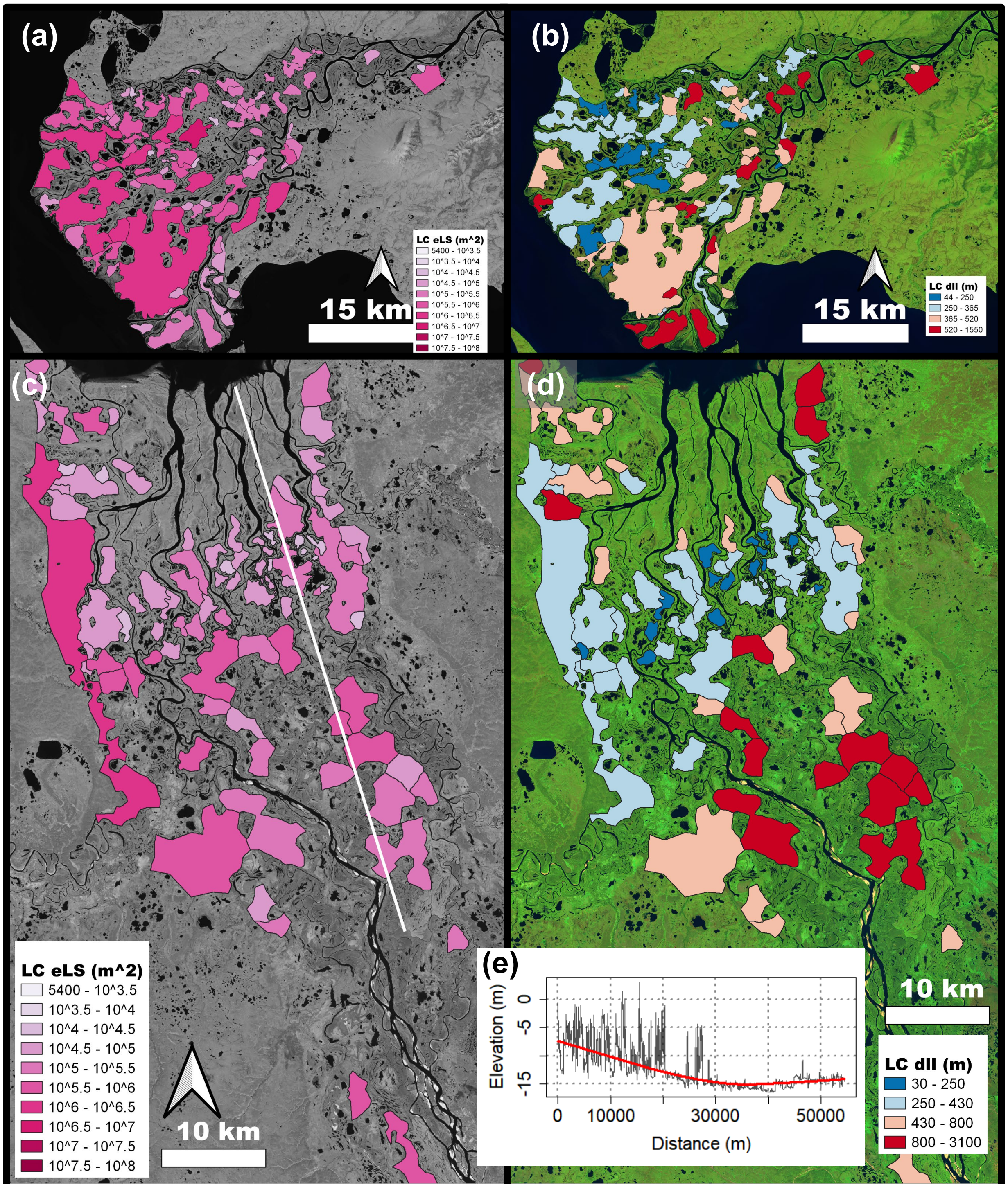

Figure 5.12: **Lake complexes on the Kobuk and Nadym deltas.** (a, b) The Kobuk delta and (c, d) the Nadym delta show distinct spatial patterns in LC coverage and location. (e) An elevation transect given by the white line in (c) which shows a local depression in the LC's with densely packed small lakes about 10 – 15 km upstream of the shoreline.

The aforementioned marine zone is present on the Yana, Kolyma, and Indigirka delta and consists of densely packed, hydrologically connected, small lakes (Figure 5.12i,j). The observed extensive inundation of the marine zone will enhance the degradation of permafrost in these regions (Zheng et al., 2019). Given the presence of ice wedge polygons and thermokarst lakes, further permafrost degradation is expected to lead to further subsidence, which suggests that these three deltas have coastal fringes particularly vulnerable to increased relative sea level rise and enhanced wave activity due to sea ice loss (Overeem et al., 2022).

A similar zone of LCs containing densely packed small lakes is observed on the Nadym delta about 12 km upstream of the coastline and spans the width of the delta. The densely packed small lakes are located within depressions which flood regularly and connect the lakes. Given the extensive intermediate water occurrence in this area and connectivity between lakes, we hypothesized this zone is a large-scale depression and should functionally serve as a retention basin with the less inundated upstream parts of the delta. A transect taken from the ArcticDEM (Porter et al., 2018) corroborates this and shows that this zone is 1 to 2 meters lower than the downstream coastal islands (Figure 5.12). This zone is likely a result of widespread ice-rich permafrost degradation, thermokarst lake formation, and eventual coalescence, which now appears as a massive seasonally inundated depression with small perennial lakes within it.

In contrast to the extensively inundated and densely packed marine zone, are the never-inundated and coarsely spaced or lake absent coastal fringe on the Nadym and Ob deltas. On the Nadym the complete absence of lakes and any inundation suggests that the coastal islands lack ice-rich permafrost altogether. High-resolution imagery from Planet Labs does not show any evidence of permafrost features such as ice-wedge polygons either (Figure 5.13). On the Ob the presence of coarse lakes suggests permafrost degradation has commenced, but high-resolution imagery shows no evidence of ice-wedge polygons, suggesting there is not widespread excess ground-ice on these islands. It is therefore not expected that further

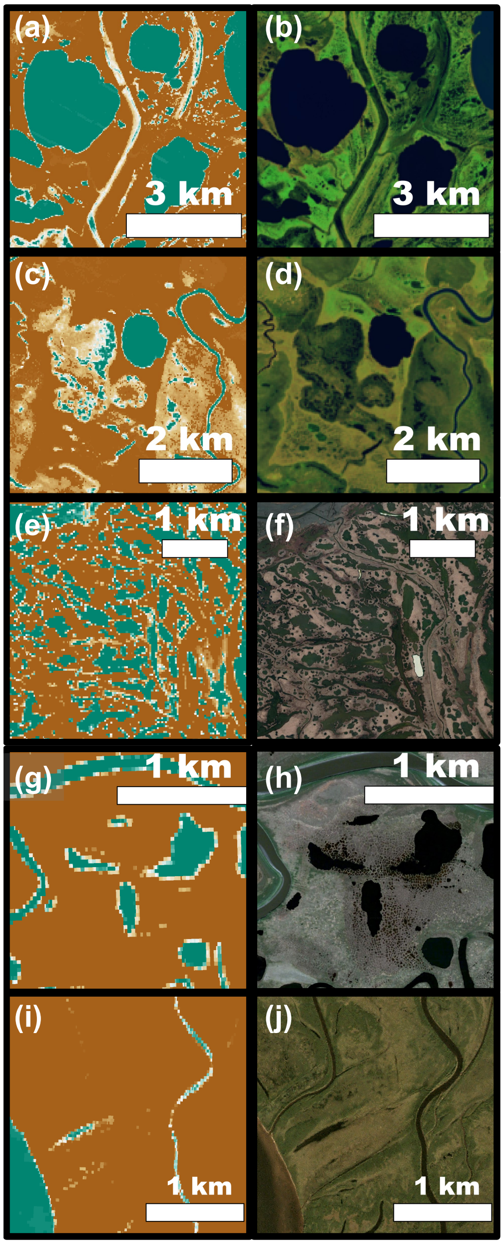

Figure 5.13: **Hydrologic processes and permafrost signatures.** Left panels show June to August water pixel occurrence for example process zones with right panels showing associated optical or multispectral satellite imagery to highlight distinct local features. (a, b) Some lakes may be part of a lake complex due to ephemeral channels which likely drain the lakes. (c, d) Some identified lakes may be part of an LC as they are the perennial remnants of drained thermokarst lake basins. (e, f) Densely packed small lakes present in LC in the marine zone indicate highly degrading permafrost, as supported by the presence of abundant small circular lakes and high-centered ice wedge polygons. (g, h) Some lakes lacking ephemeral inundation are located in low-centered polygonal tundra, suggesting a lack of permafrost degradation and potential for future lake expansion. (i, j) Areas that are never inundated and lack lakes or LC show no evidence of ice-rich permafrost.

permafrost-induced subsidence will take place and increase the vulnerability of these islands to relative sea level rise or permafrost.

The above examples highlight that lake spatial patterns encode information on permafrost presence and soil ice richness. However to extract maps of soil ice volume or permafrost thickness is not trivial and requires incorporation of higher resolution satellite imagery and field data which could be used to train algorithms for landscape classification. Moreover, the observed lake zones could be useful for highlighting representative areas that should be sampled in field campaigns to improve upscaling of point and field measurements to landscape level estimates of permafrost zonation, methane emission, and other relevant landscape properties.

5.6 Conclusions

Arctic river deltas are uniquely distinct from their temperate counterparts as they are dotted by thermokarst lakes which are formed by the thaw of ice-rich permafrost. How this lake cover interacts with the delta channel network and how thermokarst lakes on arctic deltas will respond to warming and fluvial change is not yet well understood. We take steps towards understanding thermokarst lake characteristics on deltas through a pan-arctic analysis of thermokarst lake patterns on 12 major arctic river deltas at multiple spatial scales. We show that:

1. Lake area fraction is typically larger in colder deltas and is associated with increased coverage of the delta top by larger lakes and not an increase in the number of lakes per unit delta area,

2. Heterogeneity in lake sizes is most prominent in the coldest deltas examined, which is attributed to mixed early and late stage lake growth based on the presence of abundant small lakes and large coalesced lakes

3. Lakes are non-randomly distributed on deltas and there are cohesive regions of densely packed lakes on multiple deltas which highlight areas of degraded permafrost, and
4. The degree of hydrologic connectivity between lakes varies between deltas and is spatially heterogeneous, with hydrologic connectivity resulting from hierarchical depression structure (e.g. drained thaw lake basins), ephemeral channels, and extensive permafrost degradation.

Further insight into spatially explicitly permafrost patterns may utilize high resolution satellite imagery fused with the longer-term surface water dynamics captured at medium-resolution (Landsat) presented here. Moreover, given the diversity in lake patterns within and across deltas observed here, further studies on understanding the dynamics of specific deltas through intensive field campaigns, such as the Arctic COLORS campaign on the Yukon, Kobuk, and Mackenzie (Mannino et al., 2022), are likely necessary to project the trajectories of specific systems under climate change.

CHAPTER 6

Conclusions

Summary of Work

River delts are ecologically and environmentally important landscapes which are at risk from sediment deprivation, sea level rise, and human activity (Nienhuis et al., 2020; Syvitski & Saito, 2007; Moodie & Nittrouer, 2021). Arctic river deltas specifically are influenced by cold region processes such as snowmelt-driven hydrology and permafrost-presence, which puts them at high risk from projected climate change including warming and precipitation shifts (Tokarska et al., 2020). In particular, thermokarst lakes, which are formed by the thaw of ice-rich permafrost, are expected to both expand and drain under future warming, reconfiguring deltaic hydrology and impacting the arctic carbon cycle Grosse et al. (2013). Yet studies focusing on thermokarst lake dynamics and trends in deltaic environments are limited. The goal of this work was to increase our understanding of the relationship between process and form on arctic river deltas to pave the way for process-informed predictions of delta response under different scenarios of change.

In Chapter 2, we introduced a new multiscale framework which characterizes river delta morphology via process-targeted measures of its shoreline structure, and used these measures to separate deltas into morphological classes (called morphotypes) and to infer the dominant forcing of each morphotype. We then showed that the dominant forcings inferred from shoreline structure generally align with those estimated via relative sediment fluxes, while positing that misalignments arise from spatiotemporal heterogeneity in deltaic sediment fluxes not captured in the flux estimates.

In Chapter 3, we posed the hypothesis that summertime waterbody shrinkage rates on arctic deltas are controlled by proximity to the delta channel network due to a spatially explicit pattern in active layer thickness and near surface hydrologic connectivity. We documented such a pattern in two Alaskan deltas using 27 summers of remote sensing imagery from Landsat. To provide further evidence of our hypothesis, we falsified alternative hypotheses corresponding to different mechanisms that could lead to a similar pattern, including the existence of undetected sub-pixel resolution channels and systematically shallower waterbodies closer to the channel network. We found that a thicker and deeper active layer is the most likely explanation for the observed lake shrinkage pattern and suggested the potential of investigating waterbody dynamics, from readily available satellite data, for inferring permafrost patterns which are hard to measure directly over large spatial domains.

In Chapter 4, we presented a pan-Arctic study of 12 arctic deltas wherein we classified observed waterbodies into perennial lakes and ephemeral wetlands capitalizing on the historical record of remote sensing data. We provided evidence that thermokarst lake sizes are universally lognormally distributed and that historical temperature trends are encoded in lake sizes, while wetland sizes are power law distributed and have no temperature trend. These findings help to inform possible space-for-time projections of how warming will lead to changes in lake size distribution on arctic deltas.

In Chapter 5, we used the lake dataset generated in Chapter 4 to analyze lake spatial patterns on arctic deltas to mine information on permafrost and geomorphic processes. We introduced a suite of information theoretic measures to characterize lake spatial distribution and lake cover, and utilizing these along with traditional measures we documented a weak relationship between lake spatial coverage and climate. We then showed that lake patterns are spatially structured on all deltas and that surface hydrologic connectivity between lakes is spatially variable within and across deltas, positing that such patterns reflect geomorphic process differences that can be explored for process understanding. For example, combining these analyses with higher resolution satellite imagery and field data may improve estimates of spatially distributed permafrost cover and inform our understanding of permafrost development in deltaic environments, which is important for carbon and nutrient cycling under a changing climate.

Overall, the results of this dissertation have improved our understanding of:

1. The link between observed delta morphology and the dominant forcings which have formed deltas.
2. The spatial distribution of permafrost within arctic river deltas and its relationship to lake dynamics.
3. The thermokarst lake distribution on arctic river deltas and the trajectory of deltaic thermokarst lake coverage under climate change.

Future Perspectives

The two major research avenues pursued in this thesis, namely characterization of river delta morphology via shoreline structure and mapping of surface water dynamics and patterns in arctic deltas, still leave a number of open questions that need to be pursued in order to improve projections of deltaic response to change.

Specifically, the multiscale framework for shoreline characterization developed in Chapter 2 has the potential for detailed elucidation of the relationship between morphology (form) and dominant forcings (process) in evolving deltas. For example, using physics-based numerical models which can simulate river delta morphodynamics, we could track both the relative sediment fluxes contributed by rivers, waves, and tides over the lifetime of a delta and the shoreline structure of the delta, to identify timescales of morphologic response to sediment flux changes, appropriate time periods over which to compute relative sediment fluxes, and how spatial heterogeneity in sediment fluxes manifests in distinct shoreline structure. Moreover, the characterization of river delta shoreline structure could be coupled with analysis of delta channel network structure to see what unique information is present in both features.

In arctic deltas, the methodology and techniques presented herein could be used to inform spatially explicit permafrost coverage and soil ice-richness by corroborating in-situ and field measurements of soil temperatures and ice volume with remotely sensed surface water dynamics. Remotely sensed surface water dynamics, which are spatially resolved while field measurements are not, could then be used as predictors in machine learning algorithms applied over large regions. This approach could be targeted to deltas but would also be applicable in floodplain environments. Such spatially distributed maps of permafrost coverage are critical for understanding where specific zones on a delta or floodplain are going to be most vulnerable to permafrost thaw. Moreover, numerical models of deltaic morphodynamics and hydrology are likely necessary to make projections of deltaic morphology under climate change. The observed surface water dynamics and patterns could be used to constrain and inform these models.

References

Aas, K. S., Martin, L., Nitzbon, J., Langer, M., Boike, J., Lee, H., … Westermann, S. (2019). Thaw processes in ice-rich permafrost landscapes represented with laterally coupled tiles in a land surface model. *The Cryosphere*, *13*(2), 591–609.

Adams, H., Adger, W. N., & Nicholls, R. J. (2018). Ecosystem services linked to livelihoods and well-being in the ganges-brahmaputra-meghna delta. In *Ecosystem services for well-being in deltas* (pp. 29–47). Palgrave Macmillan, Cham.

Ainsworth, R. B., Vakarelov, B. K., & Nanson, R. A. (2011). Dynamic spatial and temporal prediction of changes in depositional processes on clastic shorelines: toward improved subsurface uncertainty reduction and management. *AAPG bulletin*, *95*(2), 267–297.

Anthony, E. J. (2015). Wave influence in the construction, shaping and destruction of river deltas: A review. *Marine Geology*, *361*, 53–78.

Anthony, E. J., Besset, M., Zainescu, F., & Goichot, M. (2021). Geomorphology of a tropical river delta under pressure: the rufiji delta, tanzania—context, channel connectivity and alongshore morpho-sedimentary and hydrodynamic variability. *Geo-Marine Letters*, *41*(2), 1–11.

Arp, C. D., & Jones, B. M. (2009). *Geography of alaska lake districts: Identification, description, and analysis of lake-rich regions of a diverse and dynamic state* (Tech. Rep.). Alaska: U. S. Geological Survey.

Arp, C. D., Jones, B. M., Urban, F. E., & Grosse, G. (2011, jul). Hydrogeomorphic processes of thermokarst lakes with grounded-ice and floating-ice regimes on the Arctic coastal plain, Alaska. *Hydrological Processes*, *25*(15), 2422–2438. Retrieved from `http://doi.wiley.com/10.1002/hyp.8019` doi: 10.1002/hyp.8019

Ashton, A., & Giosan, L. (2011). Wave-angle control of delta evolution. *Geophysical Research Letters*, *38*(13).

Ashton, A., Murray, A. B., & Arnoult, O. (2001). Formation of coastline features by large-scale instabilities induced by high-angle waves. *Nature*, *414*(6861), 296–300.

Aybar, C. (2022). rgee: R bindings for calling the 'earth engine' api [Computer software manual]. Retrieved from `https://CRAN.R-project.org/package=rgee` (R package version 1.1.3)

Barnhart, K. R., Overeem, I., & Anderson, R. S. (2014). The effect of changing sea ice on the physical vulnerability of arctic coasts. *The Cryosphere*, *8*(5), 1777–1799.

Bastviken, D., Cole, J., Pace, M., & Tranvik, L. (2004). Methane emissions from lakes: Dependence of lake characteristics, two regional assessments, and a global estimate. *Global biogeochemical cycles*, *18*(4).

Baumgardner, S. E. (2015). *Quantifying galloway: Fluvial, tidal and wave influence on experimental and field deltas* (Unpublished doctoral dissertation). University of Minnesota.

Bertassello, L. E., Rao, P. S. C., Jawitz, J. W., Botter, G., Le, P. V. V., Kumar, P., & Aubeneau, A. F. (2018, jul). Wetlandscape Fractal Topography. *Geophysical Research Letters*, *45*(14), 6983–6991. Retrieved from `http://doi.wiley.com/10.1029/2018GL079094` doi: 10.1029/2018GL079094

Bhattacharya, J. P., & Giosan, L. (2003). Wave-influenced deltas: Geomorphological implications for facies reconstruction. *Sedimentology*, *50*(1), 187–210.

Broaddus, C. M., Vulis, L. M., Nienhuis, J. H., Tejedor, A., Brown, J., Foufoula-Georgiou, E., & Edmonds, D. A. (n.d.). First-order river delta morphology is explained by the sediment flux balance from rivers, waves, and tides. *Geophysical Research Letters*.

Bromwich, D., Wilson, A., Bai, L., Liu, Z., Barlage, M., Shih, C.-F., ... others (2018). The arctic system reanalysis, version 2. *Bulletin of the American Meteorological Society*, *99*(4), 805–828.

Brown, J., Ferrians, O., Heginbottom, J., & Melnikov, E. (1997). *Circum-Arctic map of permafrost and ground-ice conditions* (Tech. Rep.). Washington DC: U.S. Geological Survey in Cooperation with the Circum-Pacific Council for Energy and Mineral Resources. Retrieved from `https://nsidc.org/data/ggd318`

Burn, C. R., & Kokelj, S. V. (2009). The environment and permafrost of the mackenzie delta area. *Permafrost and periglacial processes*, *20*(2), 83–105.

Burnham, K. P., & Anderson, D. R. (2004). Multimodel inference: understanding aic and bic in model selection. *Sociological methods & research*, *33*(2), 261–304.

Cael, B., Lambert, B., & Bisson, K. (2015). Pond fractals in a tidal flat. *Physical Review E*, *92*(5), 052128.

Cael, B., & Seekell, D. A. (2016, sep). The size-distribution of Earth's lakes. *Scientific Reports*, *6*(1), 29633. Retrieved from `http://dx.doi.org/10.1038/srep29633http://www.nature.com/articles/srep29633` doi: 10.1038/srep29633

Caldwell, R. L., & Edmonds, D. A. (2014). The effects of sediment properties on deltaic processes and morphologies: A numerical modeling study. *Journal of Geophysical Research: Earth Surface*, *119*(5), 961–982.

Chadwick, A. J., Lamb, M. P., & Ganti, V. (2020). Accelerated river avulsion frequency on lowland deltas due to sea-level rise. *Proceedings of the National Academy of Sciences*, *117*(30), 17584–17590.

Chawla, A., Spindler, D. M., & Tolman, H. L. (2013). Validation of a thirty year wave hindcast using the climate forecast system reanalysis winds. *Ocean Modelling*, *70*, 189–206.

Chen, M., Rowland, J. C., Wilson, C. J., Altmann, G. L., & Brumby, S. P. (2012, jan). Temporal and spatial pattern of thermokarst lake area changes at Yukon Flats, Alaska. *Hydrological Processes*, *28*(3), 837–852. Retrieved from `http://doi.wiley.com/10.1002/hyp.9642` doi: 10.1002/hyp.9642

Chen, M., Rowland, J. C., Wilson, C. J., Altmann, G. L., & Brumby, S. P. (2013). The importance of natural variability in lake areas on the detection of permafrost degradation: A case study in the Yukon Flats, Alaska. *Permafrost and Periglacial Processes*, *24*(3), 224–240. doi: 10.1002/ppp.1783

Clauset, A., Shalizi, C. R., & Newman, M. E. J. (2009, nov). Power-Law Distributions in Empirical Data. *SIAM Review*, *51*(4), 661–703. Retrieved from `http://epubs.siam.org/doi/10.1137/070710111` doi: 10.1137/070710111

Cohen, S., Kettner, A. J., Syvitski, J., & Fekete, B. M. (2013). Wbmsed, a distributed global-scale riverine sediment flux model: Model description and validation. *Computers & Geosciences*, *53*, 80–93.

Cooley, S. W., Smith, L. C., Ryan, J. C., Pitcher, L. H., & Pavelsky, T. M. (2019, feb). Arctic-Boreal lake dynamics revealed using CubeSat imagery. *Geophysical Research Letters*, *46*, 2018GL081584. Retrieved from `https://onlinelibrary.wiley.com/doi/abs/10.1029/2018GL081584` doi: 10.1029/2018GL081584

Coon, E., Svyatsky, D., Jan, A., Kikinzon, E., Berndt, M., Atchley, A., . . . others (2019). *Advanced terrestrial simulator.* Retrieved from `https://amanzi.github.io/ats/`

Cover, T. M., & Joy, T. A. (2006). *The Fractal Geometry of Nature* (2nd ed.). New York: Wiley.

Crow, E. L., & Shimizu, K. (1988). *Lognormal Distributions Theory and Applications* (1st Editio ed.). New York: Marcel Dekker.

Cunada, C. L., Lesack, L. F., & Tank, S. E. (2021). Methane emission dynamics among co2-absorbing and thermokarst lakes of a great arctic delta. *Biogeochemistry*, *156*(3), 375–399.

Diggle, P. J. (2013). *Statistical analysis of spatial and spatio-temporal point patterns.* CRC press.

Dong, T. Y., & Goudge, T. A. (2022). Quantitative relationships between river and channel-belt planform patterns. *Geology*, *50*(9), 1053–1057.

Dupre, W. R., & Thompson, R. (1979). The yukon delta: a model for deltaic sedimentation in an ice-dominated environment. In *Offshore technology conference.*

Edmonds, D. A., Caldwell, R. L., Brondizio, E. S., & Siani, S. M. (2020). Coastal flooding will disproportionately impact people on river deltas. *Nature communications*, *11*(1), 1–8.

Egbert, G. D., & Erofeeva, S. Y. (2002). Efficient inverse modeling of barotropic ocean tides. *Journal of Atmospheric and Oceanic technology*, *19*(2), 183–204.

Emanuel, K. A. (2013). Downscaling cmip5 climate models shows increased tropical cyclone activity over the 21st century. *Proceedings of the National Academy of Sciences*, *110*(30), 12219–12224.

Emmerton, C. A., Lesack, L. F., & Marsh, P. (2007). Lake abundance, potential water storage, and habitat distribution in the mackenzie river delta, western canadian arctic. *Water Resources Research*, *43*(5).

Engram, M., Walter Anthony, K. M., Sachs, T., Kohnert, K., Serafimovich, A., Grosse, G., & Meyer, F. J. (2020, jun). Remote sensing northern lake methane ebullition. *Nature Climate Change*, *10*(6), 511–517. Retrieved from `http://dx.doi.org/10.1038/s41558-020-0762-8http://www.nature.com/articles/s41558-020-0762-8` doi: 10.1038/s41558-020-0762-8

Erftemeijer, P. L., & Hamerlynck, O. (2005). Die-back of the mangrove heritiera littoralis dryand, in the rufiji delta (tanzania) following el nino floods. *Journal of Coastal Research*, 228–235.

Fagherazzi, S., Edmonds, D. A., Nardin, W., Leonardi, N., Canestrelli, A., Falcini, F., ... Slingerland, R. L. (2015). Dynamics of river mouth deposits. *Reviews of Geophysics*, *53*(3), 642–672.

French, H. M. (2017). *The periglacial environment.* John Wiley & Sons.

Galloway, W. E. (1975). Process framework for describing the morphologic and stratigraphic evolution of deltaic depositional system. In *Deltas: Models for exploration* (pp. 87–98). Houston Geological Society.

Geleynse, N., Voller, V., Paola, C., & Ganti, V. (2012). Characterization of river delta shorelines. *Geophysical research letters*, *39*(17).

Gillespie, C. S. (2015). Fitting Heavy Tailed Distributions: The poweRlaw Package. *Journal of Statistical Software*, *64*(2). Retrieved from `http://www.jstatsoft.org/v64/i02/` doi: 10.18637/jss.v064.i02

Giosan, L., Syvitski, J., Constantinescu, S., & Day, J. (2014). Climate change: Protect the world's deltas. *Nature*, *516*(7529), 31–33.

Gouhier, T. C., Grinsted, A., & Simko, V. (2021). R package biwavelet: Conduct univariate and bivariate wavelet analyses [Computer software manual]. Retrieved from `https://github.com/tgouhier/biwavelet` ((Version 0.20.21))

Grosse, G., Jones, B., & Arp, C. (2013). *Thermokarst Lakes, Drainage, and Drained Basins* (Vol. 8). Elsevier Ltd. Retrieved from `http://dx.doi.org/10.1016/B978-0-12-374739-6.00216-5` doi: 10.1016/B978-0-12-374739-6.00216-5

Hackney, C. R., Darby, S. E., Parsons, D. R., Leyland, J., Best, J. L., Aalto, R., … Houseago, R. C. (2020). River bank instability from unsustainable sand mining in the lower mekong river. *Nature Sustainability*, *3*(3), 217–225.

Haralick, R. M., & Shapiro, L. G. (1992). *Computer and robot vision* (Vol. 1). Addison-wesley Reading.

Hariharan, J., Passalacqua, P., Xu, Z., Michael, H. A., Steel, E., Chadwick, A., … Moodie, A. J. (2022). Modeling the dynamic response of river deltas to sea-level rise acceleration. *Journal of Geophysical Research: Earth Surface*, e2022JF006762.

Helfrich, S. R., McNamara, D., Ramsay, B. H., Baldwin, T., & Kasheta, T. (2007). Enhancements to, and forthcoming developments in the interactive multisensor snow and ice mapping system (ims). *Hydrological Processes: An International Journal*, *21*(12), 1576–1586.

Hijmans, R. J. (2020). *raster: Geographic Data Analysis and Modeling.* Retrieved from `https://cran.r-project.org/package=raster`

Hoitink, A., AJ, Nittrouer, J. A., Passalacqua, P., Shaw, J. B., Langendoen, E. J., … van Maren, D. S. (2020). Resilience of river deltas in the anthropocene. *Journal of Geophysical Research: Earth Surface*, *125*(3), e2019JF005201.

Hoitink, A., Wang, Z. B., Vermeulen, B., Huismans, Y., & Kästner, K. (2017). Tidal controls on river delta morphology. *Nature Geoscience*, *10*(9), 637–645.

Huang, Z. (1998). Extensions to the k-means algorithm for clustering large data sets with categorical values. *Data mining and knowledge discovery*, *2*(3), 283–304.

Jammalamadaka, S. R., & Sengupta, A. (2001). *Topics in circular statistics* (Vol. 5). world scientific.

Jepsen, S., Voss, C., Walvoord, M. A., Rose, J., Minsley, B., & Smith, B. (2013). Sensitivity analysis of lake mass balance in discontinuous permafrost: the example of disappearing twelvemile lake, yukon flats, alaska (usa). *Hydrogeology Journal*, *21*(1), 185–200.

Jerolmack, D. J., & Swenson, J. B. (2007). Scaling relationships and evolution of distributary networks on wave-influenced deltas. *Geophysical Research Letters*, *34*(23).

Jones, B. M., Arp, C. D., Grosse, G., Nitze, I., Lara, M. J., Whitman, M. S., … Hinkel, K. M. (2020, jan). Identifying historical and future potential lake drainage events on the western Arctic coastal plain of Alaska. *Permafrost and Periglacial Processes*, *31*(1), 110–127. Retrieved from `https://onlinelibrary.wiley.com/doi/abs/10.1002/ppp.2038` doi: 10.1002/ppp.2038

Jones, B. M., Grosse, G., Arp, C. D., Jones, M. C., Walter Anthony, K. M., & Romanovsky, V. E. (2011). Modern thermokarst lake dynamics in the continuous permafrost zone, northern Seward Peninsula, Alaska. *Journal of Geophysical Research: Biogeosciences*, *116*(3), 1–13. doi: 10.1029/2011JG001666

Jorgenson, M. T. (2000). Hierarchical organization of ecosystems at multiple spatial scales on the yukon-kuskokwim delta, alaska, usa. *Arctic, Antarctic, and Alpine Research*, *32*(3), 221–239.

Jorgenson, M. T., Roth, J., Pullman, E., Burgess, R., Raynolds, M., Stickney, A., … Zimmer, T. (1997). An ecological land survey for the colville river delta, alaska, 1996. report for arco alaska, inc., anchorage, ak, by abr. *Inc., Fairbanks, AK*, *17*.

Jorgenson, M. T., Shur, Y. L., & Walker, H. J. (1998). Evolution of a permafrost-dominated landscape on the colville river delta, northern alaska. In *Proceedings of the seventh international conference on permafrost, yellowknife, canada, 1998, collect. nord* (Vol. 57, pp. 523–529).

Knights, D., Sawyer, A. H., Barnes, R. T., Piliouras, A., Schwenk, J., Edmonds, D. A., & Brown, A. M. (2020). Nitrate removal across ecogeomorphic zones in wax lake delta, louisiana (usa). *Water Resources Research*, *56*(8), e2019WR026867.

Konkol, A., Schwenk, J., Katifori, E., & Shaw, J. B. (2022). Interplay of river and tidal forcings promotes loops in coastal channel networks. *Geophysical Research Letters*, *49*.

Korotaev, V. (2011). The holocene history of the river deltasalong the arctic coast of siberia. *Geography and Natural Resources*, *32*(3), 213–219.

Korotaev, V., Rychagov, G., & Rimsky-Korsakov, N. (2017). *Morphodynamics of the mouths of large rivers of the arctic coasts of Russia.* Moscow: Moscow State University.

Kristensen, L., Christiansen, H. H., & Caline, F. (2008). Temperatures in coastal permafrost in the svea area, svalbard. In *Proceeedings of the ninth international conference on permafrost, fairbanks, alaska* (pp. 1005–1010).

Kumar, P., & Foufoula-Georgiou, E. (1994). Wavelet analysis in geophysics: An introduction. *Wavelets in geophysics*, *4*, 1–43.

Laidler, G. J., Treitz, P. M., & Atkinson, D. M. (2008). Remote sensing of arctic vegetation: relations between the ndvi, spatial resolution and vegetation cover on boothia peninsula, nunavut. *Arctic*, 1–13.

Lauzon, R., Piliouras, A., & Rowland, J. C. (2019). Ice and permafrost effects on delta morphology and channel dynamics. *Geophysical Research Letters*, *46*(12), 6574–6582.

Le, P. V. V., & Kumar, P. (2014, mar). Power law scaling of topographic depressions and their hydrologic connectivity. *Geophysical Research Letters*, *41*(5), 1553–1559. Retrieved from `http://doi.wiley.com/10.1002/2013GL059114` doi: 10.1002/2013GL059114

Le Quéré, C., Andrew, R. M., Friedlingstein, P., Sitch, S., Hauck, J., Pongratz, J., … others (2018). Global carbon budget 2018. *Earth System Science Data*, *10*(4), 2141–2194.

Lesack, L. F., & Marsh, P. (2010). River-to-lake connectivities, water renewal, and aquatic habitat diversity in the mackenzie river delta. *Water Resources Research*, *46*(12).

Lique, C., Holland, M. M., Dibike, Y. B., Lawrence, D. M., & Screen, J. A. (2016, mar). Modeling the Arctic freshwater system and its integration in the global system: Lessons learned and future challenges. *Journal of Geophysical Research: Biogeosciences*, *121*(3), 540–566. Retrieved from `http://doi.wiley.com/10.1002/2015JG003120` doi: 10.1002/2015JG003120

Malakar, N. K., Hulley, G. C., Hook, S. J., Laraby, K., Cook, M., & Schott, J. R. (2018). An operational land surface temperature product for landsat thermal data: Methodology and validation. *IEEE Transactions on Geoscience and Remote Sensing*, *56*(10), 5717–5735.

Mandelbrot, B. B. (1982). *The Fractal Geometry of Nature* (1st ed.). New York: Echo Point.

Mannino, A., Friedrichs, M., Hernes, P., Matrai, P., Salisbury, J., Tzortziou, M., & Del Castillo, C. (2022). Arctic-colors (arctic-coastal land ocean interactions) field campaign scoping study update and plans. *Authorea Preprints*.

Marsh, P., Lesack, L. F. W., & Roberts, A. (1999, nov). Lake sedimentation in the Mackenzie Delta, NWT. *Hydrological Processes*, *13*(16), 2519–2536. doi: 10.1002/(SICI)1099-1085(199911)13:16⟨2519::AID-HYP935⟩3.0.CO;2-T

McKenzie, J. M., & Voss, C. I. (2013). Permafrost thaw in a nested groundwater-flow system. *Hydrogeology Journal*, *21*(1), 299–316.

Messager, M. L., Lehner, B., Grill, G., Nedeva, I., & Schmitt, O. (2016). Estimating the volume and age of water stored in global lakes using a geo-statistical approach. *Nature communications*, *7*(1), 1–11.

Milana, J. P., & Kröhling, D. (2015). Climate changes and solar cycles recorded at the holocene paraná delta and their impact on human population. *Scientific Reports*, *5*(1), 1–8.

Mitzenmacher, M. (2004, jan). A Brief History of Generative Models for Power Law and Lognormal Distributions. *Internet Mathematics*, *1*(2), 226–251. Retrieved from `http://www.internetmathematicsjournal.com/article/1385` doi: 10.1080/15427951.2004.10129088

Moodie, A. J., & Nittrouer, J. A. (2021). Optimized river diversion scenarios promote sustainability of urbanized deltas. *Proceedings of the National Academy of Sciences*, *118*(27), e2101649118.

Morgan-Wall, T. (2021). rayshader: Create maps and visualize data in 2d and 3d [Computer software manual]. Retrieved from `https://CRAN.R-project.org/package=rayshader` (R package version 0.24.10)

Muster, S., Riley, W. J., Roth, K., Langer, M., Cresto Aleina, F., Koven, C. D., … Boike, J. (2019, jan). Size Distributions of Arctic Waterbodies Reveal Consistent Relations in Their Statistical Moments in Space and Time. *Frontiers in Earth Science*, *7*(January), 1–15.

Retrieved from `https://www.frontiersin.org/article/10.3389/feart.2019.00005/full` doi: 10.3389/feart.2019.00005

National Ice Center, . (2008). *IMS daily Northern Hemisphere snow and ice analysis at 1 km, 4 km, and 24 km resolutions.* Retrieved from `https://doi.org/10.7265/N52R3PMC`

Nelson, H., & Creager, J. S. (1977). Displacement of yukon-derived sediment from bering sea to chukchi sea during holocene time. *Geology*, *5*(3), 141–146.

Nienhuis, J. H., Ashton, A. D., Edmonds, D. A., Hoitink, A. J. F., Kettner, A. J., Rowland, J. C., & Törnqvist, T. E. (2020, jan). Global-scale human impact on delta morphology has led to net land area gain. *Nature*, *577*(7791), 514–518. Retrieved from `http://dx.doi.org/10.1038/s41586-019-1905-9http://www.nature.com/articles/s41586-019-1905-9` doi: 10.1038/s41586-019-1905-9

Nienhuis, J. H., Ashton, A. D., & Giosan, L. (2016). Littoral steering of deltaic channels. *Earth and Planetary Science Letters*, *453*, 204–214.

Nienhuis, J. H., Hoitink, A., & Törnqvist, T. E. (2018). Future change to tide-influenced deltas. *Geophysical Research Letters*, *45*(8), 3499–3507.

Nienhuis, J. H., Kim, W., Milne, G. A., Quock, M., Slangen, A. B., & Törnqvist, T. E. (2023). River deltas and sea-level rise. *Annual Review of Earth and Planetary Sciences*, *51*.

Nitze, I., Grosse, G., Jones, B. M., Romanovsky, V. E., & Boike, J. (2018, dec). Remote sensing quantifies widespread abundance of permafrost region disturbances across the Arctic and Subarctic. *Nature Communications*, *9*(1), 5423. Retrieved from `http://dx.doi.org/10.1038/s41467-018-07663-3http://www.nature.com/articles/s41467-018-07663-3` doi: 10.1038/s41467-018-07663-3

Nowosad, J., & Stepinski, T. F. (2018). Spatial association between regionalizations using the information-theoretical v-measure. *International Journal of Geographical Information Science*, *32*(12), 2386–2401.

Obu, J., Westermann, S., Bartsch, A., Berdnikov, N., Christiansen, H. H., Dashtseren, A., . . . Zou, D. (2019, jun). Northern Hemisphere permafrost map based on TTOP modelling for 2000–2016 at 1 km2 scale. *Earth-Science Reviews*, *193*(October 2018), 299–316. Retrieved from `https://doi.org/10.1016/j.earscirev.2019.04.023https://linkinghub.elsevier.com/retrieve/pii/S0012825218305907` doi: 10.1016/j.earscirev.2019.04.023

Okabe, A., Boots, B., Sugihara, K., & Chiu, S. N. (2000). *Spatial tessellations: concepts and applications of voronoi diagrams* (2nd ed.). John Wiley & Sons.

Overeem, I., Jafarov, E., Wang, K., Schaefer, K., Stewart, S., Clow, G., . . . Elshorbany, Y. (2018, sep). A Modeling Toolbox for Permafrost Landscapes. *Eos*, *99*. Retrieved from `https://eos.org/project-updates/a-modeling-toolbox-for-permafrost-landscapes` doi: 10.1029/2018EO105155

Overeem, I., Nienhuis, J. H., & Piliouras, A. (2022). Ice-dominated arctic deltas. *Nature Reviews Earth & Environment*, *3*(4), 225–240.

Overeem, I., & Syvitski, J. P. (2010). Shifting discharge peaks in arctic rivers, 1977–2007. *Geografiska Annaler: Series A, Physical Geography*, *92*(2), 285–296.

Overeem, I., Syvitski, J. P., & Hutton, E. W. (2005). Three-dimensional numerical modeling of deltas. *River Deltas—Concepts, Models, and Examples*.

Passalacqua, P., Giosan, L., Goodbred, S., & Overeem, I. (2021). Stable$\neq$ sustainable: Delta dynamics versus the human need for stability. *Earth's Future*, *9*(7), e2021EF002121.

Pastick, N. J., Jorgenson, M. T., Wylie, B. K., Nield, S. J., Johnson, K. D., & Finley, A. O. (2015). Distribution of near-surface permafrost in alaska: Estimates of present and future conditions. *Remote Sensing of Environment*, *168*, 301–315.

Pastick, N. J., Jorgenson, M. T., Wylie, B. K., Rose, J. R., Rigge, M., & Walvoord, M. A. (2014). Spatial variability and landscape controls of near-surface permafrost within the alaskan yukon river basin. *Journal of Geophysical Research: Biogeosciences*, *119*(6), 1244–1265.

Pau, G., Fuchs, F., Sklyar, O., Boutros, M., & Huber, W. (2010). EBImage-an R package for image processing with applications to cellular phenotypes. *Bioinformatics*, *26*(7), 979–981. doi: 10.1093/bioinformatics/btq046

Pebesma, E. (2018). Simple Features for R: Standardized Support for Spatial Vector Data. *The R Journal*, *10*(1), 439–446. Retrieved from `https://doi.org/10.32614/RJ-2018-009` doi: 10.32614/RJ-2018-009

Pebesma, E. (2021). stars: Spatiotemporal arrays, raster and vector data cubes [Computer software manual]. Retrieved from `https://CRAN.R-project.org/package=stars` (R package version 0.5-5)

Pekel, J.-F., Cottam, A., Gorelick, N., & Belward, A. S. (2016). High-resolution mapping of global surface water and its long-term changes. *Nature*, *540*(7633), 418–422.

Perignon, M., Adams, J., Overeem, I., & Passalacqua, P. (2020). Dominant process zones in a mixed fluvial–tidal delta are morphologically distinct. *Earth Surface Dynamics*, *8*(3), 809–824.

Petrescu, A. M., Van Beek, L. P., Van Huissteden, J., Prigent, C., Sachs, T., Corradi, C. A., . . . Dolman, A. J. (2010). Modeling regional to global CH4 emissions of boreal and arctic wetlands. *Global Biogeochemical Cycles*, *24*(4), 1–12. doi: 10.1029/2009GB003610

Piliouras, A., Lauzon, R., & Rowland, J. C. (2021). Unraveling the combined effects of ice and permafrost on arctic delta morphodynamics. *Journal of Geophysical Research: Earth Surface*, *126*(4), e2020JF005706.

Piliouras, A., & Rowland, J. C. (2020). Arctic river delta morphologic variability and implications for riverine fluxes to the coast. *Journal of Geophysical Research: Earth Surface*, *125*(1), e2019JF005250.

Plug, L. J., Walls, C., & Scott, B. M. (2008, feb). Tundra lake changes from 1978 to 2001 on the Tuktoyaktuk Peninsula, western Canadian Arctic. *Geophysical Research Letters*, *35*(3), L03502. Retrieved from `http://doi.wiley.com/10.1029/2007GL032303` doi: 10.1029/2007GL032303

Porter, C., Morin, P., Howat, I., Noh, M.-J., Bates, B., Peterman, K., … others (2018). Arcticdem. *Harvard Dataverse*, *1*, 2018–2030.

Prowse, T., Alfredsen, K., Beltaos, S., Bonsal, B., Duguay, C., Korhola, A., … Weyhenmeyer, G. A. (2011). Arctic freshwater ice and its climatic role. *Ambio*, *40*(1), 46–52.

Rey, D. M., Walvoord, M., Minsley, B., Rover, J., & Singha, K. (2019). Investigating lake-area dynamics across a permafrost-thaw spectrum using airborne electromagnetic surveys and remote sensing time-series data in yukon flats, alaska. *Environmental Research Letters*, *14*(2), 025001.

Rover, J., Ji, L., Wylie, B. K., & Tieszen, L. L. (2012). Establishing water body areal extent trends in interior alaska from multi-temporal landsat data. *Remote Sensing Letters*, *3*(7), 595–604.

Rowland, J. C., Dietrich, W. E., Day, G., & Parker, G. (2009). Formation and maintenance of single-thread tie channels entering floodplain lakes: Observations from three diverse river systems. *Journal of Geophysical Research: Earth Surface*, *114*(F2).

Rowland, J. C., Travis, B. J., & Wilson, C. J. (2011). The role of advective heat transport in talik development beneath lakes and ponds in discontinuous permafrost. *Geophysical Research Letters*, *38*(17), 1–5. doi: 10.1029/2011GL048497

Sawyer, A. H., Edmonds, D. A., & Knights, D. (2015). Surface water-groundwater connectivity in deltaic distributary channel networks. *Geophysical research letters*, *42*(23), 10–299.

Schuur, E. A., McGuire, A. D., Schädel, C., Grosse, G., Harden, J. W., Hayes, D. J., … Vonk, J. E. (2015). Climate change and the permafrost carbon feedback. *Nature*, *520*(7546), 171–179. doi: 10.1038/nature14338

Schwenk, J., Lanzoni, S., & Foufoula-Georgiou, E. (2015). The life of a meander bend: Connecting shape and dynamics via analysis of a numerical model. *Journal of Geophysical Research: Earth Surface*, *120*(4), 690–710.

Schwenk, J., Piliouras, A., & Rowland, J. C. (2020). Determining flow directions in river channel networks using planform morphology and topology. *Earth Surface Dynamics*, *8*(1), 87–102.

Seybold, H., Andrade Jr, J. S., & Herrmann, H. J. (2007). Modeling river delta formation. *Proceedings of the National Academy of Sciences*, *104*(43), 16804–16809.

Shaw, J. B., Wolinsky, M. A., Paola, C., & Voller, V. R. (2008). An image-based method for shoreline mapping on complex coasts. *Geophysical Research Letters*, *35*(12).

Shur, Y. L., & Jorgenson, M. T. (2007). Patterns of permafrost formation and degradation in relation to climate and ecosystems. *Permafrost and Periglacial Processes*, *18*(1), 7–19.

Smith, L. C., Sheng, Y., MacDonald, G., & Hinzman, L. (2005, jun). Disappearing Arctic Lakes. *Science*, *308*(5727), 1429–1429. Retrieved from `http://www.sciencemag.org/cgi/doi/10.1126/science.1108142` doi: 10.1126/science.1108142

Squires, M. M., Lesack, L. F., Hecky, R. E., Guildford, S. J., Ramlal, P., & Higgins, S. N. (2009). Primary production and carbon dioxide metabolic balance of a lake-rich arctic river floodplain: partitioning of phytoplankton, epipelon, macrophyte, and epiphyton production among lakes on the mackenzie delta. *Ecosystems*, *12*(5), 853–872.

Stadnyk, T. A., Tefs, A., Broesky, M., Déry, S., Myers, P., Ridenour, N., . . . Gustafsson, D. (2021). Changing freshwater contributions to the arctic: A 90-year trend analysis (1981–2070). *Elem Sci Anth*, *9*(1), 00098.

Stephani, E., Drage, J., Miller, D., Jones, B. M., & Kanevskiy, M. (2020). Taliks, cryopegs, and permafrost dynamics related to channel migration, colville river delta, alaska. *Permafrost and Periglacial Processes*, *31*(2), 239–254.

Straub, K. M., Li, Q., & Benson, W. M. (2015). Influence of sediment cohesion on deltaic shoreline dynamics and bulk sediment retention: A laboratory study. *Geophysical Research Letters*, *42*(22), 9808–9815.

Strimas-Mackey, M. (2021). smoothr: Smooth and tidy spatial features [Computer software manual]. Retrieved from `https://CRAN.R-project.org/package=smoothr` (R package version 0.2.2)

Syvitski, J., Anthony, E., Saito, Y., Zăinescu, F., Day, J., Bhattacharya, J. P., & Giosan, L. (2022). Large deltas, small deltas: Toward a more rigorous understanding of coastal marine deltas. *Global and Planetary Change*, 103958.

Syvitski, J., Kettner, A. J., Overeem, I., Hutton, E. W. H., Hannon, M. T., Brakenridge, G. R., . . . Nicholls, R. J. (2009, oct). Sinking deltas due to human activities. *Nature Geoscience*, *2*(10), 681–686. Retrieved from `http://www.nature.com/doifinder/10.1038/ngeo629http://www.nature.com/articles/ngeo629` doi: 10.1038/ngeo629

Syvitski, J., & Saito, Y. (2007). Morphodynamics of deltas under the influence of humans. *Global and Planetary Change*, *57*(3-4), 261–282.

Tank, S. E., Lesack, L. F., & Hesslein, R. H. (2009). Northern Delta lakes as summertime CO2 absorbers within the arctic landscape. *Ecosystems*, *12*(1), 144–157. doi: 10.1007/s10021-008-9213-5

Tejedor, A., Longjas, A., Caldwell, R., Edmonds, D. A., Zaliapin, I., & Foufoula-Georgiou, E. (2016). Quantifying the signature of sediment composition on the topologic and dynamic complexity of river delta channel networks and inferences toward delta classification. *Geophysical Research Letters*, *43*(7), 3280–3287.

Tejedor, A., Longjas, A., Edmonds, D. A., Zaliapin, I., Georgiou, T. T., Rinaldo, A., & Foufoula-Georgiou, E. (2017). Entropy and optimality in river deltas. *Proceedings of the National Academy of Sciences*, *114*(44), 11651–11656.

Tejedor, A., Longjas, A., Passalacqua, P., Moreno, Y., & Foufoula-Georgiou, E. (2018). Multiplex networks: A framework for studying multiprocess multiscale connectivity via coupled-network theory with an application to river deltas. *Geophysical Research Letters*, *45*(18), 9681–9689.

Tejedor, A., Longjas, A., Zaliapin, I., & Foufoula-Georgiou, E. (2015a). Delta channel networks: 1. a graph-theoretic approach for studying connectivity and steady state transport on deltaic surfaces. *Water Resources Research*, *51*(6), 3998–4018.

Tejedor, A., Longjas, A., Zaliapin, I., & Foufoula-Georgiou, E. (2015b). Delta channel networks: 2. metrics of topologic and dynamic complexity for delta comparison, physical inference, and vulnerability assessment. *Water Resources Research*, *51*(6), 4019–4045.

Tejedor, A., Schwenk, J., Kleinhans, M., Limaye, A. B., Vulis, L., Carling, P., … Foufoula-Georgiou, E. (2022). The entropic braiding index (ebi): A robust metric to account for the diversity of channel scales in multi-thread rivers. *Geophysical Research Letters*, *49*(16), e2022GL099681.

Tognin, D., D'Alpaos, A., Marani, M., & Carniello, L. (2021). Marsh resilience to sea-level rise reduced by storm-surge barriers in the venice lagoon. *Nature Geoscience*, *14*(12), 906–911.

Tokarska, K. B., Stolpe, M. B., Sippel, S., Fischer, E. M., Smith, C. J., Lehner, F., & Knutti, R. (2020). Past warming trend constrains future warming in cmip6 models. *Science advances*, *6*(12), eaaz9549.

Van Huissteden, J., Berrittella, C., Parmentier, F., Mi, Y., Maximov, T., & Dolman, A. (2011). Methane emissions from permafrost thaw lakes limited by lake drainage. *Nature Climate Change*, *1*(2), 119–123.

Veremeeva, A., Nitze, I., Günther, F., Grosse, G., & Rivkina, E. (2021). Geomorphological and climatic drivers of thermokarst lake area increase trend (1999–2018) in the kolyma lowland yedoma region, north-eastern siberia. *Remote Sensing*, *13*(2), 178.

Victorov, A. S., Orlov, T. V., Kapralova, V. N., Trapeznikova, O. N., Sadkov, S. A., & Zverev, A. V. (2019). Stochastic Modeling of Natural Lacustrine Thermokarst Under Stable and Unstable Climate. In *Natural hazards and risk research in russia* (pp. 241–267). Springer International. Retrieved from `http://link.springer.com/10.1007/978-3-319-91833-4_18` doi: 10.1007/978-3-319-91833-4_18

Viereck, L. A. (1973). Ecological effects of river flooding and forest fires on permafrost in the taiga of alaska. In *Proceedings of the second international permafrost conference* (pp. 60–67).

Vonk, J. E., Tank, S. E., Bowden, W. B., Laurion, I., Vincent, W. F., Alekseychik, P., . . . others (2015). Reviews and syntheses: Effects of permafrost thaw on arctic aquatic ecosystems. *Biogeosciences*, *12*(23), 7129–7167.

Vulis, L., Tejedor, A., Ma, H., Nienhuis, J. H., Broaddus, C. M., Brown, J. C., . . . Foufoula-Georgiou, E. (in review). River delta morphotypes emerge from multiscale characterization of shorelines. *Geophysical Research Letters*. doi: 10.1029/2019GL086710

Vulis, L., Tejedor, A., Schwenk, J., Piliouras, A., Rowland, J., & Foufoula-Georgiou, E. (2020, apr). Channel Network Control on Seasonal Lake Area Dynamics in Arctic Deltas. *Geophysical Research Letters*, *47*(7). Retrieved from `https://onlinelibrary.wiley.com/doi/abs/10.1029/2019GL086710` doi: 10.1029/2019GL086710

Vulis, L., Tejedor, A., Zaliapin, I., Rowland, J. C., & Foufoula-Georgiou, E. (2021). Climate signatures on lake and wetland size distributions in arctic deltas. *Geophysical Research Letters*, *48*(20), e2021GL094437.

Walker, H. J. (1998). Arctic deltas. *Journal of Coastal Research*, 719–738.

Walter Anthony, K., Schneider von Deimling, T., Nitze, I., Frolking, S., Emond, A., Daanen, R., . . . Grosse, G. (2018). 21st-century modeled permafrost carbon emissions accelerated by abrupt thaw beneath lakes. *Nature communications*, *9*(1), 1–11.

Walvoord, M. A., & Kurylyk, B. L. (2016, jun). Hydrologic Impacts of Thawing Permafrost-A Review. *Vadose Zone Journal*, *15*(6), 1 – 20. Retrieved from `https://dl.sciencesocieties.org/publications/vzj/abstracts/15/6/vzj2016.01.0010http://doi.wiley.com/10.2136/vzj2016.01.0010` doi: 10.2136/vzj2016.01.0010

Wellman, T. P., Voss, C. I., & Walvoord, M. A. (2013). Impacts of climate, lake size, and supra-and sub-permafrost groundwater flow on lake-talik evolution, yukon flats, alaska (usa). *Hydrogeology journal*, *21*(1), 281–298.

Wolinsky, M. A., Edmonds, D. A., Martin, J., & Paola, C. (2010). Delta allometry: Growth laws for river deltas. *Geophysical Research Letters*, *37*(21).

Woo, M.-k. (2012). *Permafrost hydrology.* Springer Science & Business Media.

Xu, K., Bentley, S. J., Day, J. W., & Freeman, A. M. (2019). A review of sediment diversion in the mississippi river deltaic plain. *Estuarine, Coastal and Shelf Science*, *225*, 106241.

Yoshikawa, K., & Hinzman, L. D. (2003). Shrinking thermokarst ponds and groundwater dynamics in discontinuous permafrost near Council, Alaska. *Permafrost and Periglacial Processes*, *14*(2), 151–160. doi: 10.1002/ppp.451

Zanardo, S., Zaliapin, I., & Foufoula-Georgiou, E. (2013). Are american rivers tokunaga self-similar? new results on fluvial network topology and its climatic dependence. *Journal of Geophysical Research: Earth Surface*, *118*(1), 166–183.

Zhang, Y., Jafarov, E., Piliouras, A., Jones, B. M., Rowland, J., & Moulton, D. (2023). The thermal response of permafrost to coastal floodplain flooding. *Environmental Research Letters*.

Zheng, L., Overeem, I., Wang, K., & Clow, G. D. (2019). Changing arctic river dynamics cause localized permafrost thaw. *Journal of Geophysical Research: Earth Surface*, *124*(9), 2324–2344.

Zoccarato, C., Da Lio, C., Tosi, L., & Teatini, P. (2019). A coupled biomorpho-geomechanical model of tidal marsh evolution. *Water Resources Research*, *55*(11), 8330–8349.

APPENDIX A

Supplementary Material for Chapter 2

This appendix contains supplementary material for Chapter 2. The supplementary material includes a detailed description of the methods used for shoreline characterization, discussion on the use of the curvature operator for mapping shorelines to 1-D spatial-series, and assessment of the morphometric classification sensitivity to the definition of the fine scale variance.

A.1 Extended Methodology

Shoreline Extraction

The Opening Angle Method (OAM; (Shaw et al., 2008)) was used to define the shorelines of the deltas under study. The OAM and related methods (Geleynse et al., 2012) are used in river mouth impacted coastlines where the traditional definition for a shoreline as the land water interface is not meaningful as the interface can extend far upstream of the actual river mouth.

To utilize the OAM, it is first necessary to generate a binary water mask of the subaerial extent of the delta. Water masks were generated from the Landsat-derived Global Surface Water (GSW) dataset, which provides 30-m spatial and monthly temporal resolution water masks from 1984 to 2018 and is available via Google Earth Engine (Pekel et al., 2016). An individual water mask was used for each delta. In order to account for missing data due to cloud cover and seasonal heterogeneity in water cover, water masks were generally obtained by thresholding the 1984 to 2018 occurrence product, which measures the fraction of time a pixel was covered by water from 1984 to 2018. In deltas with active shorelines e.g. the Danube or Wax Lake, the occurrence for a single representative year was used (Table S1), i.e. maps which measure the fraction of time a pixel was covered by water for a specific year. In the Arctic, snowmelt-driven floods from April to June lead to significant seasonal variability in inundation and apparent subaerial delta extent, therefore the June occurrence was used to identify maximum mouth extent (Vulis et al., 2021). When necessary, masks were manually cleaned to edit or remove features such as jetties or rice paddies, which are visible from contemporaneous satellite imagery and the GSW has difficulty accounting for at its 30-m spatial resolution. Lastly, the OAM algorithm computes an opening angle on all water pixels that lie within the convex hull of the land in the water mask, which leads to unnecessary computations in channel sections upstream of the mouth which are entirely blocked by land. Therefore, these upstream sections were manually marked as land which decreased OAM runtime, as has been previously proposed (Baumgardner, 2015). The OAM was then run on the water mask corresponding to each delta. We made computational improvements to the OAM which significantly improved runtime, and have published this as an R package available via GitHub (https://github.com/lvulis/ROAM). A critical angle θ_c of 45° was then used to define the shoreline as an ordered set of coordinates $S^R_{45} : \{(x, y)_{45}\}$, although we found that the emergent shoreline classification does not change when using a critical angle θ_c of 50°. The shoreline defined in S^R_{45} only extends over the subaerial extent of the delta with start and end points of the shoreline defining the limits of the delta. The subaerial delta was visually outlined and compared with geologic maps where the extent was not clear from Landsat imagery. Note that in several deltas, non-depositional sections of the coastline were included in S^R_{45}, e.g. in valley confined systems such as the Dnieper and Don, and these were removed. Also note that the Missisippi Head of Passes, the Atchafayla, and

Wax Lake deltas were all analyzed as separate systems due to their spatial independence in line with other studies (Galloway, 1975; Geleynse et al., 2012; Konkol et al., 2022; Knights et al., 2020).

Finally, to remove discretization artifacts on the shorelines which arise from being defined at the 30-m pixel scale, the raw shoreline in S_{45}^{R} was first smoothed using a Nadaraya-Watson kernel smoother with a bandwidth of 180-meters (Strimas-Mackey, 2021) and then resampled at a 60-meter interval, resulting in the shoreline S_{45} used in the geometric and spectral analysis.

Macroscale – Shape

To measure the shape of the delta, a circle with parameters $\{(x_c, y_c), R_c\}$ was fit to S_{45} using least squares (Jammalamadaka & Sengupta, 2001). The shoreline may correspond only to a sector of a circle, which the least squares fit captures. The center of the circle (x_c, y_c) corresponds to the center of curvature and R_c the radius of curvature. Deltas with a center of curvature lying in the ocean are concave, while those with a center of curvature lying over land are convex. When R_c is significantly larger than the arc length L_C of the circular sector corresponding to the shoreline, the shoreline is essentially flat. That is, when the ratio $L_c/R_c = \varphi$, where φ is the angle of the sector, is smaller than a cutoff φ_{min}, the shoreline is flat. We found that a cutoff $\varphi_{min} = 2\pi/12 = 30^\circ$ clearly separated flat from concave and convex deltas, i.e. if the shoreline corresponds to a circular sector with a radius at least 12 times its length, it is flat.

Mesoscale – Fraction of variance contributed by mouths

To measure the fraction of variance contributed by mouths (fM), first sections of S_{45} corresponding to mouths were identified by denoting which points in S_{45}^{R} are not a part of S_{90}^{R}, the shoreline corresponding to a critical angle of $\theta_c = 90°$, i.e. $M_{45}^{R} = \{(x_i, y_i) | (x_i, y_i) \in S_{45}^{R}$ and $\notin S_{90}^{R}\}$. This is because OAM-defined shorelines using different critical angles do not overlap within local concavities (e.g. mouths or embayments). This definition may include embayments such as lagoons sheltered by spits, therefore M_{45}^{R} was manually inspected and cleaned to represent only mouths. Lastly, the same smoothing procedure used to transform S_{45}^{R} to S_{45} was used to smooth M_{45}^{R} and produce M_{45}, which identifies the set of points in the smoothed shoreline as mouths.

Then to measure what fraction of variability in S_{45} is contributed by M_{45} we used wavelet analysis to locally estimate the variance in shoreline structure at multiple scales (Kumar & Foufoula-Georgiou, 1994). For the wavelet analysis a univariate series representing the shoreline was produced as the distance d_c from every point in S_{45} to the center of curvature (x_c, y_c), defining a signal $d_c(l)$, where l is the distance along the shoreline. For convex deltas, the mouths show up as minima, which can be seen in the Mahakam Delta (Fig. 2.2). We found that this mapping of the shoreline to a univariate series is preferable to approaches such as extracting the local curvature series, which is effectively a high-pass filter removing large scale features and is sensitive to discretization, see Appendix A.3. Note that mouth widths are typically non-uniform within a delta, resulting in multiscale variability in the $d_c(l)$ signal, supporting the use of localized analysis of variance in the spatial domain. Then, the wavelet transform of $d_c(l)$ was computed using the Morlet wavelet, which has optimal time-frequency localization, with a central frequency of 6 rad/s (Kumar & Foufoula-Georgiou, 1994). The wavelet coefficients are given by $\Psi_{k,l}$ at a wavenumber (spatial frequency) k and location l along the shoreline, and are used to estimate the power, $\Psi_{k,l}^2$ (Fig. A.2).

Finally, the *fM* is defined as the ratio of the integrated wavelet power for all scales over coefficients corresponding to the mouths, $\Psi_{k,l\in M}$ over the total power (i.e. variance) of the signal (Eqn. A.1), where L is the length of the shoreline and k_{min} and k_{max} are the minimum and maximum wavenumbers, respectively. Note that typically, wavelet coefficients inside the cone of influence (COI) are excluded from the computation of the variance as they are impacted by edge effects. However, in some deltas the mouths may contain very large features, sometimes spanning over one third of the length of the signal, therefore for all deltas these coefficients were included for more robust estimation of the relative energy in these locations.

$$fM = \int_{k_{min}}^{k_{max}} \int_0^L \Psi_{k,l\in M}^2 dldk / \int_{k_{min}}^{k_{max}} \int_0^L \Psi_{k,l}^2 dldk. \tag{A.1}$$

Microscale – Gini-Corrected Fine Scale Variance

Lastly the wavelet transform (Kumar & Foufoula-Georgiou, 1994) was used to estimate the variance at fine scales, i.e. from 300 to 1000 meters (Eqn. A.2). Note that here edge effects from the COI can significantly influence the estimated amount of energy at the scales of the features under study, therefore coefficients inside the COI are excluded and the power at each wavenumber k is normalized by the number of points at that frequency, N_k. The sensitivity of the lower bound of 1000 meters was evaluated and no significant changes in the classification were found (Fig. A.1).

$$FSV_{1000} = \frac{1}{N_k} \int_{1/1000}^{1/300} \int_0^L \Psi_{k,l}^2 dldk. \tag{A.2}$$

Although two systems may have the same variance at fine scales, one may lack structural variability (i.e. correspond to white noise), while another may have peaks or increased variability at distinct scales. To account for this structured variability, the power spectral density (PSD) of the actual shoreline spatial series is compared to a white noise series with equivalent variance. Specifically, a spectral Gini coefficient g, which measures the total deviation of the cumulative PSD ($cPSD$) from the $cPSD$ of white noise is computed over the fine scales, and used as a multiplier to the FSV_{1000}, defining the $gFSV = g * FSV_{1000}$. This multiplier is low when shoreline variability is similar to white noise, and high when shoreline variability has defined structures (i.e. peaks or higher energy at finer or coarser scales), and helps to separate deltas with similar FSV_{1000} but distinct modes of variability (see Appendix A.3 for details).

All analyses were performed in R using open source geospatial, statistical, and spectral analyses packages (Strimas-Mackey, 2021; Pebesma, 2018, 2021; Pau et al., 2010; Morgan-Wall, 2021; Aybar, 2022; Gouhier et al., 2021).

Sediment Flux Data

Sediment fluxes for every delta were obtained from version 3 of the 932020Nienhuis et al.Nienhuis et al. () database, which used the WBMSed hydrologic model forced with 1981 to 2010 hydroclimate and assuming no human intervention of landscape properties to estimate riverine sediment fluxes, Q_R, (Cohen et al., 2013), angular wave climate data from WaveWatch 3.0 (Chawla et al., 2013) averaged from 1979 to 2009 to estimate wave sediment fluxes, Q_W, and tidal constituents from TXPOv8 inverted from satellite altimetry measurements from 1992 to 2006 (Egbert & Erofeeva, 2002) to estimate tidal sediment fluxes, Q_T. To reduce uncertainty in tidal amplitude estimates associated with the delta outlet location being located too far upstream of the coastline in the global delta database, for all deltas tidal amplitudes from the TXPO grid were obtained at the OAM shoreline extracted at a critical angle 90°. This only resulted in a difference of more than 5 cm for 9 out of 54 deltas, all with significantly widened mouths.

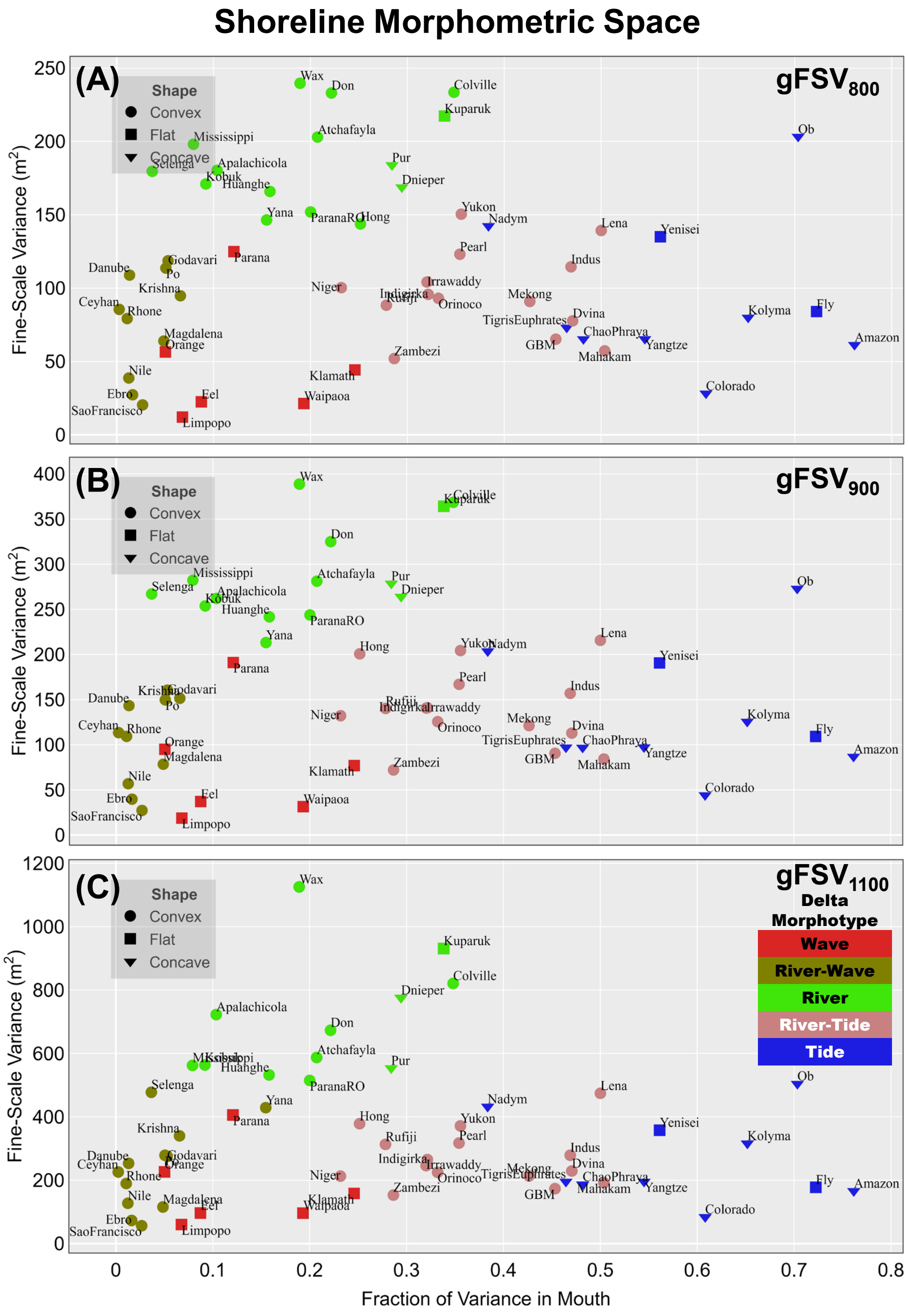

Figure A.1: **Insensitivity of the emergent classes to the upper bound of the finescale variance**. There is almost no discernible difference in the deltas belonging to each emergent phenotype when adjusting the upper wavelength of the Gini-corrected Fine Scale Variance ($gFSV$) between 800 m to 1100 m. Only the Selenga and Yana switch from the river phenotype to river-wave phenotype for an upper wavelength of 1100 m, but lay on the boundary of the two classes.

Sediment flux data represents a delta-wide value, see Nienhuis et al. (2020) and references therein for details. For every delta, the relative sediment flux r_x, where x represents either the river, wave, or tide component is defined as:

$$r_x = \frac{Q_x}{Q_R + Q_T + Q_W}. \tag{A.3}$$

A.2 Spectral Gini Coefficient Definition

In order to help separate wave-influenced deltas which are smooth and lack distinct features in the fine scale ranges from the river and tide influenced deltas which contain structure at fine scales, we adjusted the finescale variance by a spectral gini coefficient. To define the spectral gini coefficient and interpert this adjustment, first consider the wavelet-estimated power spectral density, given by Eqn. A.4,

$$PSD(k) = \frac{1}{N_k} \int_0^L \Psi_{k,l}^2 dl, \tag{A.4}$$

where l is the location and k the wavenumber (scale). The spectral variance SV for a range of wavenumbers (scales) k_0 to k_1 is found by integrating with respect to k:

$$SV = \int_{k_0}^{k_1} PSD(k)dk. \tag{A.5}$$

In general, two signals may have identical SV for a given range of scales but distinct structure. For example, white noise, which by definition has a constant PSD, i.e. $PSD_{WN} = P$, and lacks any structural variability, may have the same SV as a signal with structured variability. To measure the deviation from white noise, consider the normalized PSD, $PSD^*(k)$, given in (Eqn. A.6). $PSD^*(k)$ is analogous to a probability density function (PDF), where the integral over the support (i.e. from k_0 to k_1) is 1.

$$PSD^*(k) = \frac{PSD(k)}{SV}. \tag{A.6}$$

White noise has a uniform spectrum (i.e. flat PSD), while the PSD of another signal may be distributed heterogeneously over the range of wavenumbers (Fig. A.2). We then consider the normalized cumulative power spectral density, $cPSD^*(k)$, where k can take on any value up to k_1:

$$cPSD^*(k) = \int_{k_0}^{k} PSD^*(u)du. \tag{A.7}$$

White noise has a linear $cPSD^*$, while the shoreline $cPSD^*$ is skewed towards relatively coarser scales for $k_0 = \frac{1}{1000}$ m^{-1} and $k_1 = \frac{1}{300}$ m^{-1} (Fig. A.2). For these skewed distributions, a natural measure of the deviation from a uniform distribution is the Gini Coefficient, g, which measures the area between the $cPSD^*(k)$ of white noise, $cPSD^*_{WN}(k)$, and the $cPSD^*(k)$ of the shoreline, normalized by the area under the curve of $cPSD^*_{WN}(k)$. As these distribution functions represent spectra this is a spectral Gini Coefficient.

$$g = \frac{\int_{k_0}^{k_1} (cPSD^*_{WN}(k) - cPSD^*(k))dk}{\int_{k_0}^{k_1} cPSD^*_{WN}(k)dk}. \tag{A.8}$$

The coefficient g increases towards a maximum value of 1 as the PSD is more heterogeneous and approaches zero as the PSD approximates white noise. This coefficient is used as a multiplier to the FSV, computed from $k_0 = \frac{1}{1000}$ m^{-1} to $k_1 = \frac{1}{300}$ m^{-1}, of the shoreline spectra, accounting for the heterogeneous distribution of variance among scales indicative of distinct scale-dependent features (Fig. A.2).

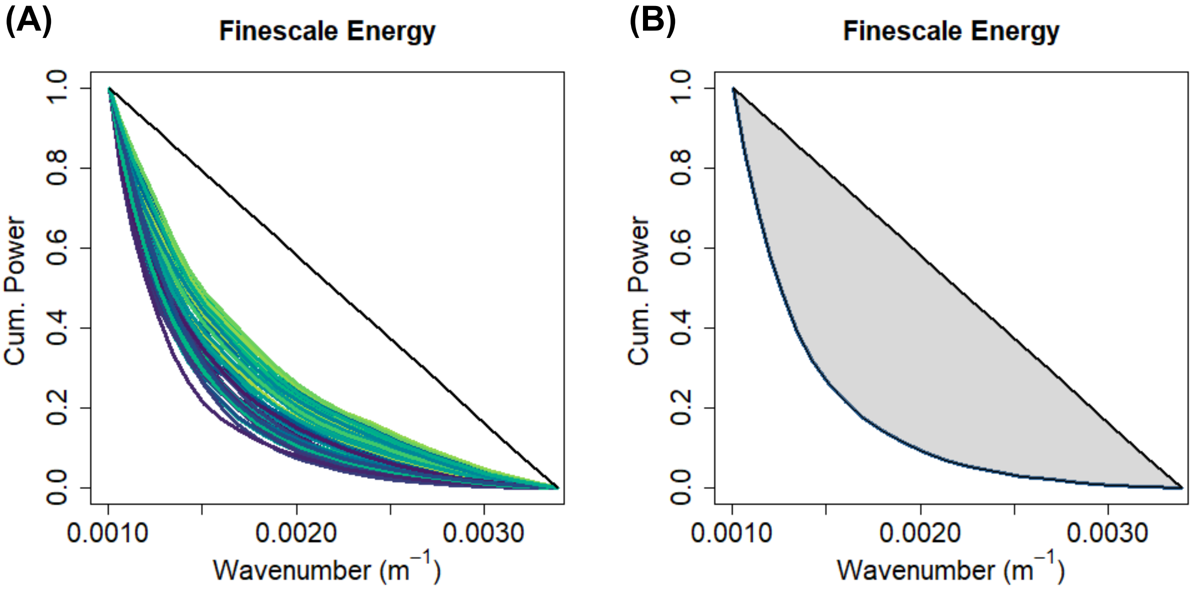

Figure A.2: **Cumulative Power Spectral Density ($cPSD^*$) of the shoreline signals.** (A) The $cPSD^*$ curves of the 54 analyzed delta shorelines, each normalized to have a value of one over the fine scales. The straight black line is $cPSD^*_{WN}$ and overlaps for each delta due to the normalization to have unit power. (B) Example of the deviation between an arbitrarily selected real shoreline and white noise with equivalent energy. The Gini Coefficient (g) is the area between the two curves normalized by the area under the white noise.

A.3 Unsuitability of curvature mapping for shoreline characterization

A common technique to quantitatively analyze meandering rivers is to map the 2D curve corresponding to the channel centerline to a 1D spatial-series represented by its curvature, e.g. (Schwenk et al., 2015), which could also be applied to delta shorelines to perform wavelet analysis. However, for the problem of shoreline characterization we found that the high-pass filter properties of the curvature operator make it unsuitable for extraction of large scale patterns such as channel mouths using spectral analysis. A synthetic example using sinusoids is given to demonstrate these high-pass filter properties. Consider two sinusoids of differing wavenumber with random additive error, $z_1(s) = 5\sin(s) + \mathcal{N}(0, .5)$ and $z_2(s) = 20\sin(\frac{s}{2\pi}) + \mathcal{N}(0,\ 2)$, along with their sum $z_3(s) = z_2(s) + z_1(s)$ (Fig. A.3). The sinusoids represent spatial-series with s being some distance along the shoreline, and are sampled with spatial step $\Delta s = 1$. To analyze the oscillations, the Fourier transform $\hat{z}(k)$ with wavenumber k is taken, with the power spectral density of each signal given in the right panel of (Fig. A.3). The additive signal z_3 has clearly defined peaks at $k = (2\pi)^{-1}$ and $k = (2\pi)^{-2}$.

In the case where the functional relationship between z and s is not known, we may want to map the set of coordinates of each $\{(s, z)_i\}$ to a univariate series to employ spectral analysis to characterize the curve. One such common mapping is defining the local curvature κ. For an ordered set of coordinates $\{(x, y)_i\}$ constituting a 2D planar curve, a stable and smooth estimator of the local curvature $\kappa = 1/R$ is given in Schwenk et al. (2015):

$$R = \frac{1}{2}\frac{\sqrt{(\mathbf{a_x^2} + \mathbf{a_y^2})(\mathbf{b_x^2} + \mathbf{b_y^2})(\mathbf{c_x^2} + \mathbf{c_y^2})}}{(\mathbf{a_y b_x} - \mathbf{a_x b_y})}, \tag{A.9}$$

where $\mathbf{a_x} = x_i - x_{i-1}$, $\mathbf{b_x} = x_{i+1} - x_{i-1}$,$\mathbf{c_x} = x_{i+1} - x_i$. This definition and related curvature operators given in Schwenk et al. (2015) clearly depend on the sampling resolution of the

2-D planar curve.

The curvature is computed for each curve given by the $\{(s, z)\}$ coordinate pairs to define a univariate series $\kappa(l)$, where l is the distance along the curve (Fig. A.4). The noise present in the original signals is amplified by taking local differences and results in the large variation seen in κ_2 and κ_3. The corresponding power spectral density shows that for the high wavenumber series, κ_1, the curvature mapping still captures the wavenumber observed in z_1, but κ_2 and κ_3 have no power near the real wavenumber of $(2\pi)^{-2}$. This is because taking finite differences to compute the curvature filters out the low wavenumber signal.

The sensitivity or ability to capture the low wavenumber signal likely depends on the ratio of the sampling wavenumber $k_s = \Delta s^{-1}$ to the wavenumber of interest k_u, k_s/k_u. By the Nyquist theorem, this ratio must be at least 2 to resolve k_u. When the ratio approaches 2 from a larger value, noise may not be amplified by the curvature transformation, but when it is much larger than 2 noise is amplified. Some value sufficiently optimal to capture k_u using the curvature transformation may exist. However, mouth widths are not constant on deltas and can vary at least by a factor of 2, therefore k_u can vary significantly, so a k_s optimal for the narrowest mouth will amplify noise in the remaining, larger mouths. Moreover, a sufficiently high k_s to capture mouths would filter out information at low wavenumbers, e.g. large scale features such as deltaic lobes. For these reasons the mapping of curvature is not suitable for the problem of shoreline characterization.

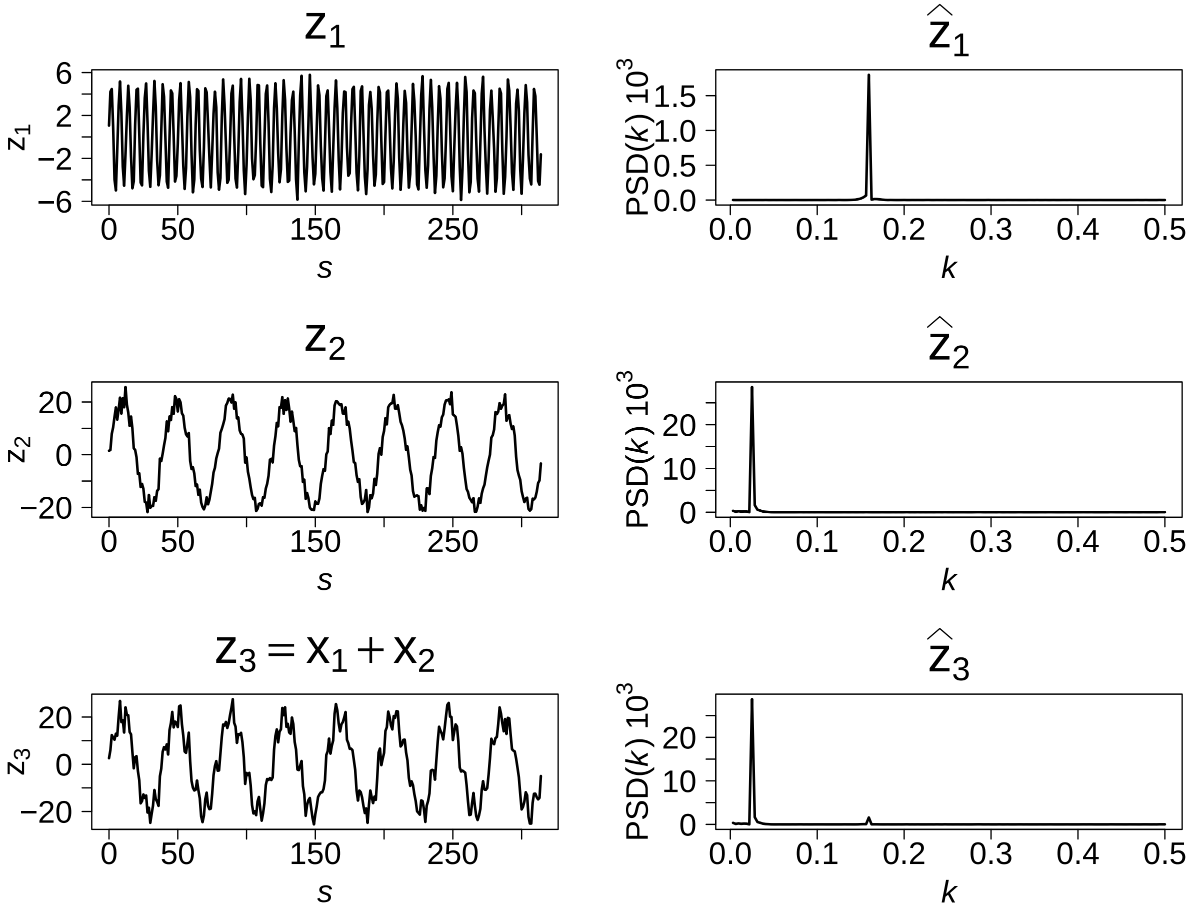

Figure A.3: **Synthetic sinusoids and their corresponding power spectral density.**

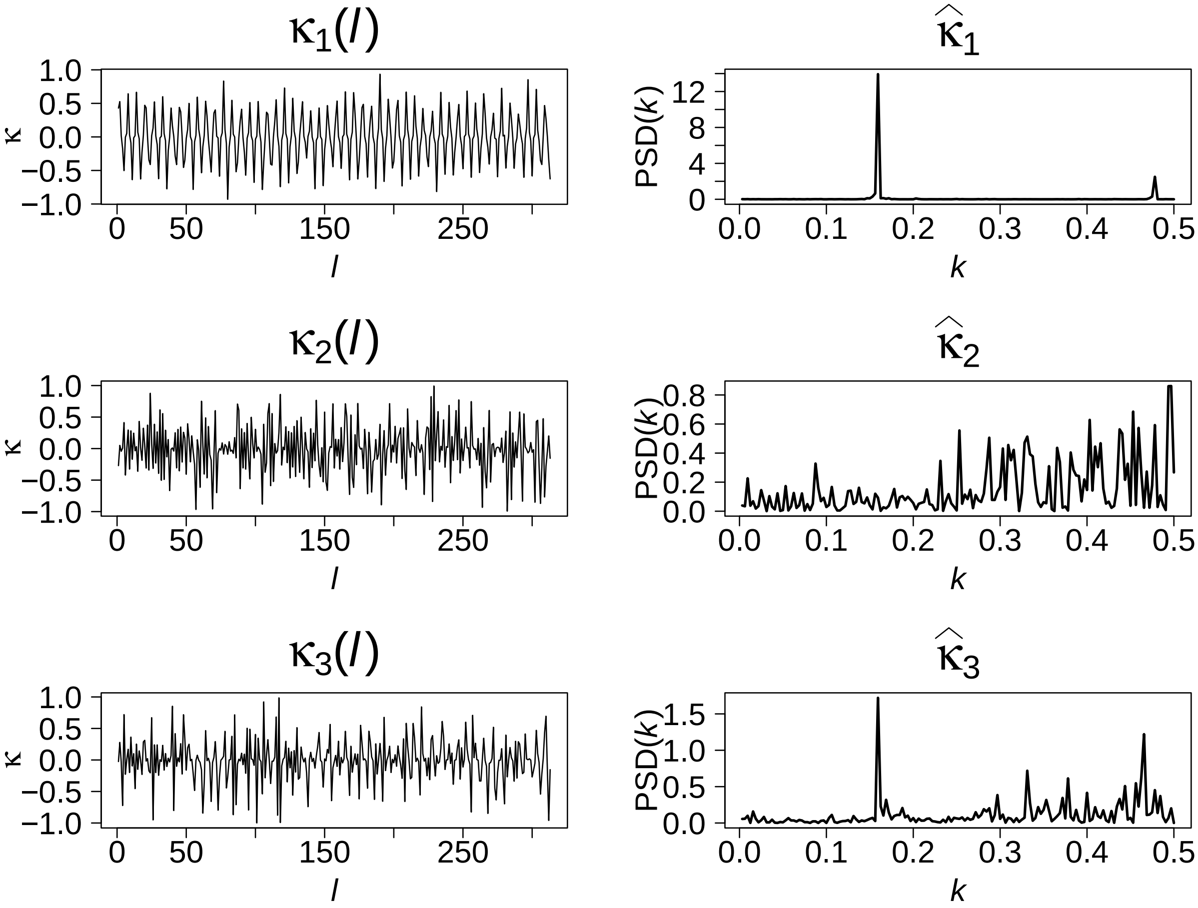

Figure A.4: **Result of the curvature operator on sinusoids.** The sinusoids from Fig. A.3 transformed to curvature spatial-series using Equation (A.9). Note that κ_2 and κ_3 fail to capture the low frequency signal present in z_2 and z_3.

APPENDIX B

Supplementary Material for Chapter 3

This appendix contains supplementary material for Chapter 3. This includes sample hydrographs of both deltas studied, discussion on channel network extraction and computation of shrinkage, distance to the nearest channel distribution, definition of the lake internal perimeter, lake area distribution conditional on distance to the nearest channel, and estimated near surface permafrost as a function of distance to the nearest channel.

B.1 Water Mask Description and Channel Network Extraction

Global Surface Water (GSW) masks are images whose pixels may take one of three values: water, land, and no data. No data pixels can arise from lack of imagery, snow and ice cover, cloud cover, and Landsat 7 striping (Pekel et al., 2016). From September to May, no water or land pixels were identified over the Colville (i.e. 100% no data) due to cloud, snow, and ice cover for any year over the period of record. In the Yukon, September to April are unresolved (no data) for all years over the period of record, while some May masks are partially resolved from 2000 to 2018. However, manual inspection of the Landsat scenes used to derive the masks indicate snow and ice cover being resolved as water in parts of the delta, indicating misclassification. Inspection of the summer June and July masks in both deltas indicated that the remaining snow and ice cover were classified as no data or land. We analyzed

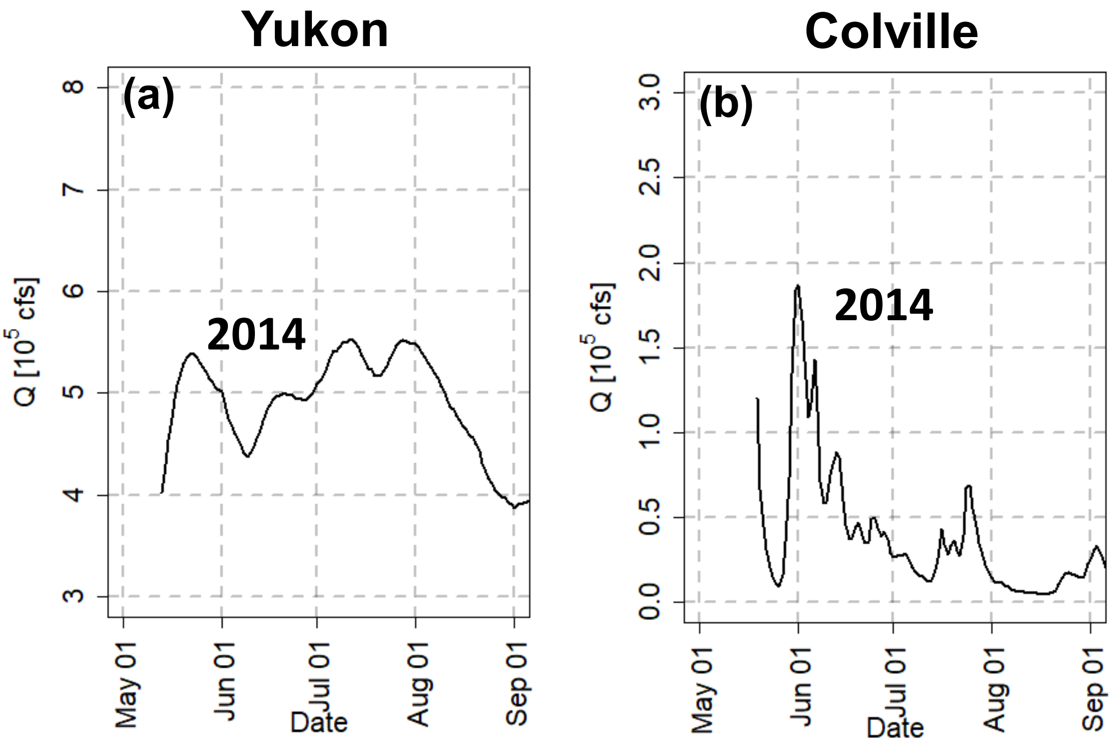

Figure B.1: **Hydrographs on the Yukon and Colville rivers.** (a) Streamflow at Pilot Station (USGS 15565447). The streamgage is downstream of any major confluences and is 75 km away from the apex of the Yukon Delta. (b) Streamflow at Umiat (USGS 15875000). The streamgage is upstream of confluences with the Chandler and Anaktuvuk rivers, and is 100 km away from the apex of the Colville Delta. The bankfull flow, defined as the two-year flow, was estimated on the Yukon from 35 years of data to be $655,000$ ft^3/s and on the Colville from 16 years of data to be $176,000$ ft^3/s.

summers where at least 60% of the delta, excluding the channel network, was resolved as water or land, which included 2002, 2004, 2005, 2007 – 2009, 2013, 2014, 2016, and 2017 on the Yukon and 2001, 2002, and 2005 – 2018 on the Colville (see Figs. B.2b and B.2d). Manual inspection of the 2018 June and July masks on the Yukon showed misclassification of large portions of the scene, and this year was not considered in the analysis.

To extract the channel network, we used the Python package RivGraph (Schwenk et al., 2020). RivGraph takes as inputs: (1) a binary mask of the channel network, (2) locations of inlets, and (3) a shoreline, and fully resolves the channel network topology as a set of georeferenced links and nodes. The inlet node was marked at the first major bifurcation of the deltas, and we defined the shorelines excluding the tidal zone, demarcated by lack of vegetation, as seen in Figures 3.1b and 3.1c (Dupre & Thompson, 1979; Jorgenson et al., 1997). We used a single water mask, extracted from a composite water mask, where a pixel is defined as water if it shows an 80% June water occurrence over the recorded period. Comparison of the composite DCN skeleton with channel skeletons extracted from individual years did not show significant difference on either delta. To account for the interannual variability in channel extent, for every year analyzed we extracted all waterbodies over the delta using connected component analysis (Haralick & Shapiro, 1992) for each of the two monthly water masks in the summer (June and July) and excluded from our analysis, for the year, any pixels corresponding to connected components (i.e. waterbodies) that overlapped with the DCN. Additionally, for each season, any pixel that was classified as no data in any given month was treated as no data for the entire summer, i.e. a pixel was valid only if it was classified as water or land for June and July in a given year. The remaining objects that were at least one pixel in size that were disconnected from the channel network were considered as individual waterbodies (i.e. lakes) for each season. Without waterbody bathymetry information, we were unable to systematically remove shallow wetlands during lake extraction, however the water surface temperature analysis shows that it is not more likely for waterbodies closer to the DCN to be shallow wetlands versus waterbodies farther away from channels.

To account for small channels below the Landsat resolution, we used all DigitalGlobe images available via Google Earth for the two deltas to manually identify the presence or absence of surface connections between lakes and the channel network. On the Yukon, the scenes available corresponded to July 16, 2003, June 1, 2005, August 19, 2006, July 9, 2007, September 10, 2008, June 30, 2009, June 5, 2010, July 30, 2010, September 26, 2010, May 25, 2011, August 17, 2011, June 13, 2012, August 9, 2012, September 11, 2012, and October 9, 2012. On the Colville, the scenes available corresponded to July 5, 2005, June 17, 2006, June 29, 2007, August 5, 2011, July 3, 2012, August 11, 2012, August 6, 2013, August 26, 2014, and July 13, 2016. The temporal mismatch between the June and July GSW masks used for extraction of waterbodies and the dates of these high resolution scenes may lead to some misclassification of connected lakes as disconnected, and introduce some uncertainty of our results.

B.2 Pixel-based Shrinkage Calculations

We estimated the monthly shrinkage rate S, as the pixel-based monthly water area loss fraction S_p using the following methodology. For all land and water pixels we computed the distance to the nearest channel, i.e. d_{nc}, and formed the probability density function (PDF) of d_{nc}, $f(d_{nc})$. We then partitioned the spatial extent of the delta in terms of d_{nc} into K regions where the limits of each region were selected according to equally spaced quantiles of d_{nc}, to ensure that the shrinkage rate was computed from samples of equal size and maintained similar regions from year to year. For every d_{nc} region k, we calculated the fraction of water area lost (i.e. water area that became land area) from time t to time $t+\tau$:

$$S_{p,k} = \frac{A_{w_{k,t} \to l_{k,t+\tau}}}{A_{w_{k,t}} * \tau} \tag{B.1}$$

where $A_{w_{k,t}}$ is the water area in region k at time t and $A_{w_{k,t} \to l_{k,t+\tau}}$ is the water area that became land area in region k at time $t+\tau$; here t corresponds to June and τ is one month. We consider $S_{p,k}$ as an estimate of the shrinkage rate S from June to July for lakes within region k, i.e. lakes located at distances from the DCN between the q_k and q_k+1 quantiles of the d_{nc}. As discussed in section 3.2, no major avulsions were observed for the studied deltas during the observational record. This allowed us for each delta to define a constant DCN and the same K regions through time. As the shrinkage pattern appeared robust from year to year and is modulated only in magnitude (Figs. 3.2a and 3.2c), we computed a weighted mean water area loss fraction, $\bar{S_p}$ for both deltas from June to July over the period of record (Equation 2; dotted black line in Figs. 3.2a and 3.2c), where weights $\lambda_{k,y}$ were calculated using Equation 3, where $n_{y,k}$ is the number of valid pixels (water or land) in region k for years y from 1 to Y:

$$\bar{S_{p,k}} = \sum_{y=1}^{Y} S_{p,k} \lambda_{y,k} \tag{B.2}$$

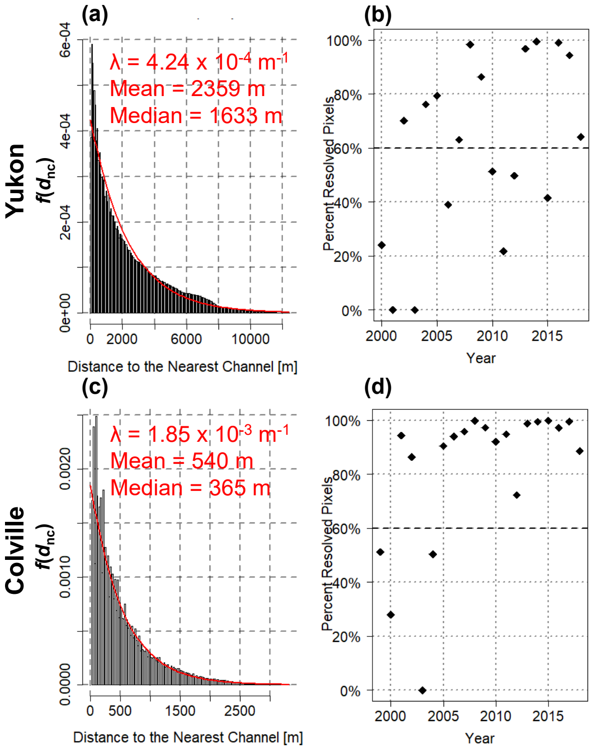

Figure B.2: **Distance to nearest channel distribution and percent of resolved pixels each year.** (a, c) The probability distribution function of nearest distance to the channel network, $f(d_{nc})$ for the Yukon (a) and Colville (c) deltas, with a fitted exponential distribution shown in red. (b, d) The fraction of the delta top resolved in the Global Surface Water dataset for both June and July in each year shown in Figures 3.2a and 3.2c, for the Yukon (b) and Colville (d) deltas, with shrinkage rates only calculated for years with at least 60% of the delta resolved.

$$\lambda_{k,y} = \frac{n_{y,k}}{\sum_{y=1}^{Y} n_{y,k}} \tag{B.3}$$

This method treats every water pixel independently of other water pixels, i.e. does not take into account the shape of the lake that the pixel is part of, and therefore has the advantage of not requiring lakes to be completely resolved during the season. Shrinkage rates may thus be estimated even in years with moderate data quality.

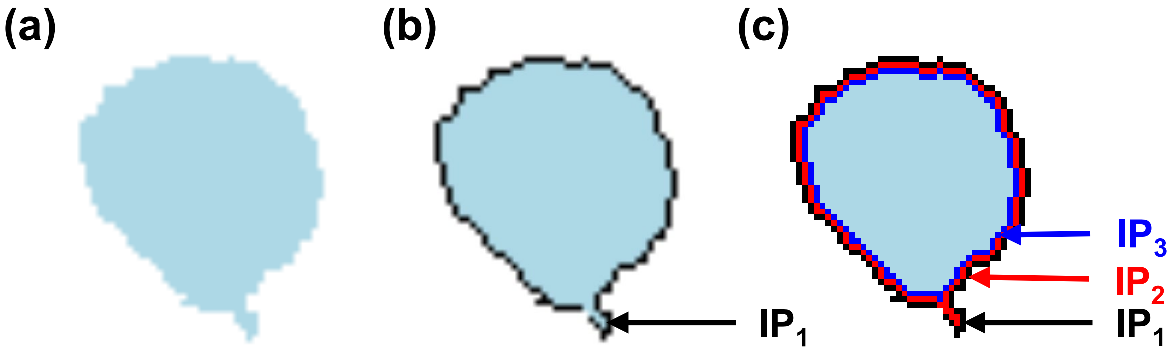

Figure B.3: **Lake Internal Perimeter Definition.** (a) Schematic of Internal Perimeter (IP) extraction using morphological erosion, where classified water pixels are in light blue. Each set of pixels removed by an erosion operation represents a subsequent lake shoreline, or IP. After a single erosion we obtain IP$_1$ (b). After three erosions we obtain IP$_1$ (c).

B.3 Lake Internal Perimeter Definition

To identify lake shorelines, we used iterative morphological erosion with a diamond-shaped structuring element, which removes a one-pixel thick shoreline, i.e. the i^{th} Internal Perimeter (IP$_\text{i}$), from every object. The eroded water mask is then used as input for the next iteration. The obtained IPs represent the subsequent shorelines of every lake on the delta top. To calculate monthly lake shoreline shrinkage rate at IP$_\text{i}$, S_{IP_i}, equation B.1 was used, but only water pixels in IP$_\text{i}$ were used in the calculation. For example, in Figure 3.3c the fraction of black pixels that shrank would give the monthly lake shoreline shrinkage rate.

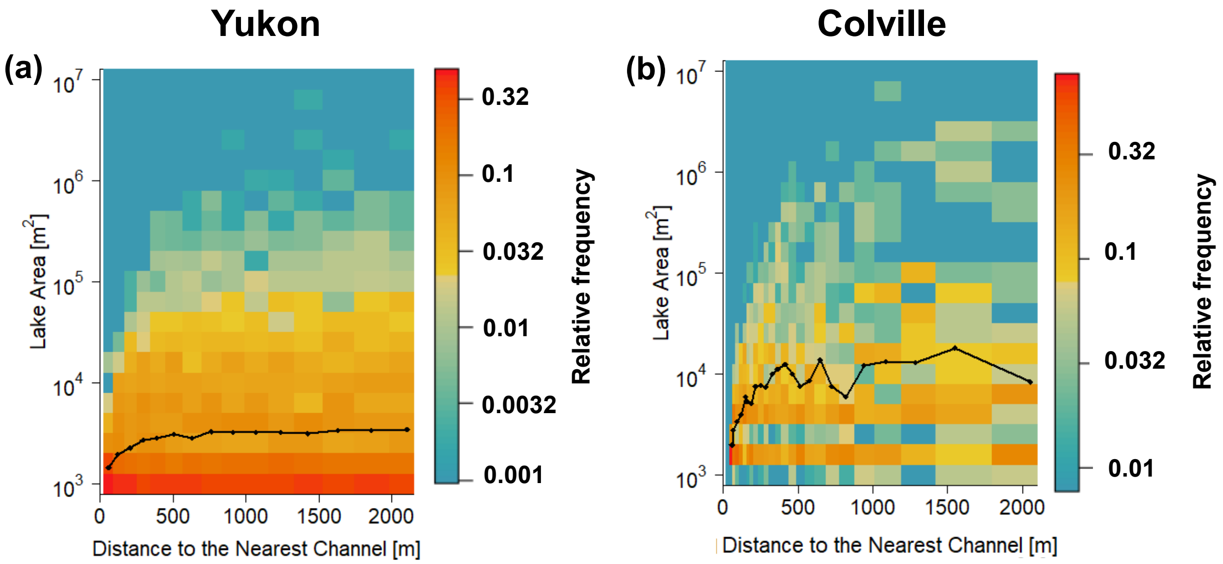

Figure B.4: **Lake Area Distributions within each distance to the nearest channel region.** (a, b) Conditional histograms of object-based lake area within each bin of distance to the nearest channel for the Yukon (a) and the Colville (b) from the Global Surface Water June 2014 water mask, with red-orange colors indicating higher relative frequency. The mean lake area at each distance is indicated by the black line.

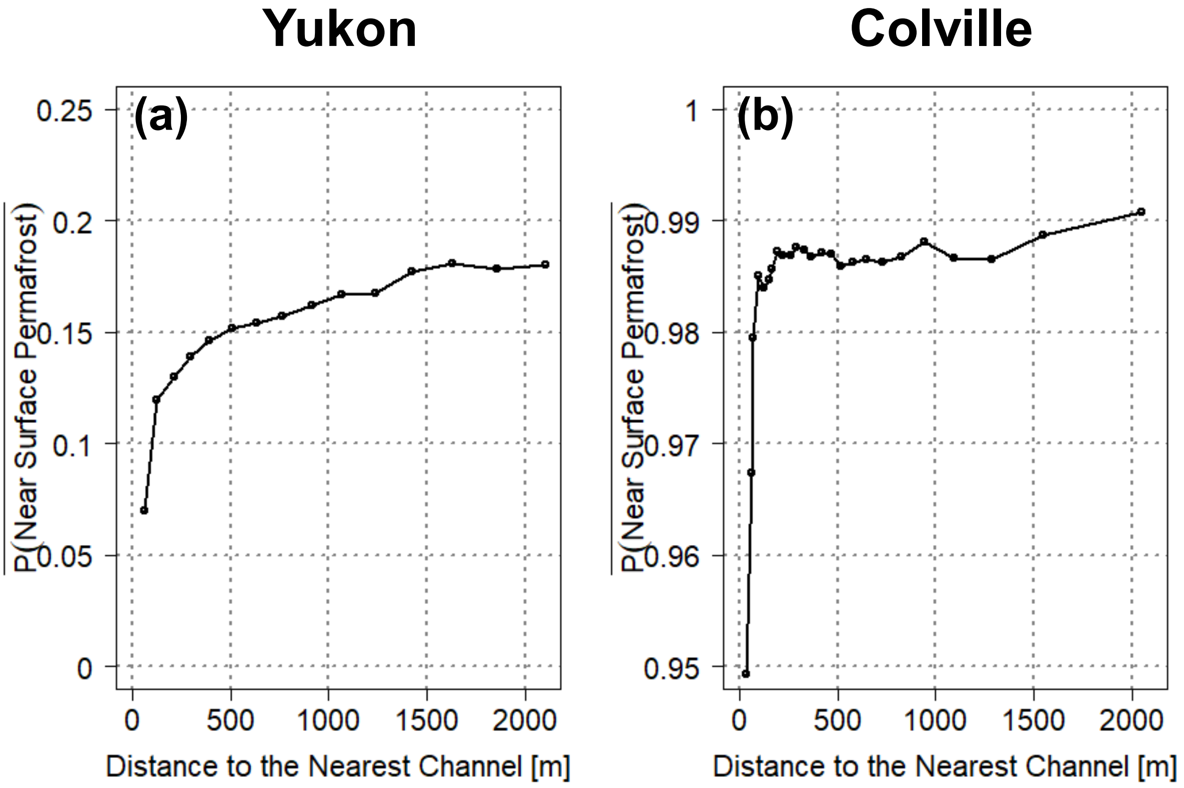

Figure B.5: **Delta channel network control on near surface permafrost.** (a, b) Bin-average probability of observing near surface permafrost, that is, depth to permafrost less than 1 meter extracted from the empirical model of Pastick et al. (2015), versus distance to the nearest channel for the Yukon (a) and the Colville (b). The Yukon shows steadily increasing probability, indicating active layer thickness decreases to less than 1 meter farther from the DCN, while the Colville shows a nearly constant probability, which is supported by observations of thaw depths being on average 30 to 75 cm on the delta (Jorgenson et al., 1998). It is expected that a process-based model of permafrost coverage on an arctic delta should produce similar curves.

APPENDIX C

Supplementary Material for Chapter 4

This appendix contains supplementary material for Chapter 4. This includes information on quality control of the Global Surface Water dataset (Pekel et al., 2016), hydrology of the deltas and choice of the year for waterbody mask extraction, a description of the proportionate growth model, the Fitted distribution parameters and climate trends for lakes, wetlands, and waterbodies, discussion on model identification for small samples of power-law distributed data, and relationships between the first three conditional moments.

C.1 Quality control of the Global Surface Water dataset

Thorough quality control of the water masks is necessary to reduce uncertainty in the estimated pixel water occurrence w_i and therefore the waterbody classification scheme. In particular, misclassified or poorly classified masks, e.g. where land pixels are classified as water or vice-versa, particularly in the presence of abundant unresolved pixels (i.e. pixels unable to be classified as land or water due to cloud cover, Landsat 7 striping, or other issues), introduce errors into the estimate of w_i, which lead to waterbody misclassification. To address this, we performed the following quality control procedure consisting of a combination of quantitative rules and visual inspection on the GSW monthly water masks for all 12 deltas. First, for every delta we discarded from the analysis any mask over the period of record that had less than 10% of the study region resolved, as we observed misclassification errors for such poor-quality data. Second, we performed a visual inspection for significant misclassification errors, e.g. stripes of pixels classified as land or water or large swaths of the region appearing to be land only for a single year, and found only July 2016 on the Lena delta had to be discarded. Third, we identified and estimated mis-collocation errors in the GSW dataset of at least 1 pixel (30 meters) over the Yana delta from 2016 to 2018 and Lena delta from 2017 to 2018 relative to the masks from 1999 to 2015. These years were discarded from the computation of the July water pixel occurrence, w_i, but were used to estimate the average water cover since mis-collocation does not imply features were misclassified, only that their locations were shifted. No miscollocation on the order of one pixel (30-m) was observed on the other 10 deltas from 1999 to 2018. Note that the Pechora delta has not been considered in this work because of a large collocation error even in GSW v1.0 (i.e. years prior to 2016). An example of the collocation errors is shown for the Yana delta, where waterbodies extracted from July 2018 are shifted to the north-west compared to waterbodies extracted from July 2011 (Figure C.1). Due to interannual variability in surface water extent and a lack of ground control points, we were not able to compute the exact collocation

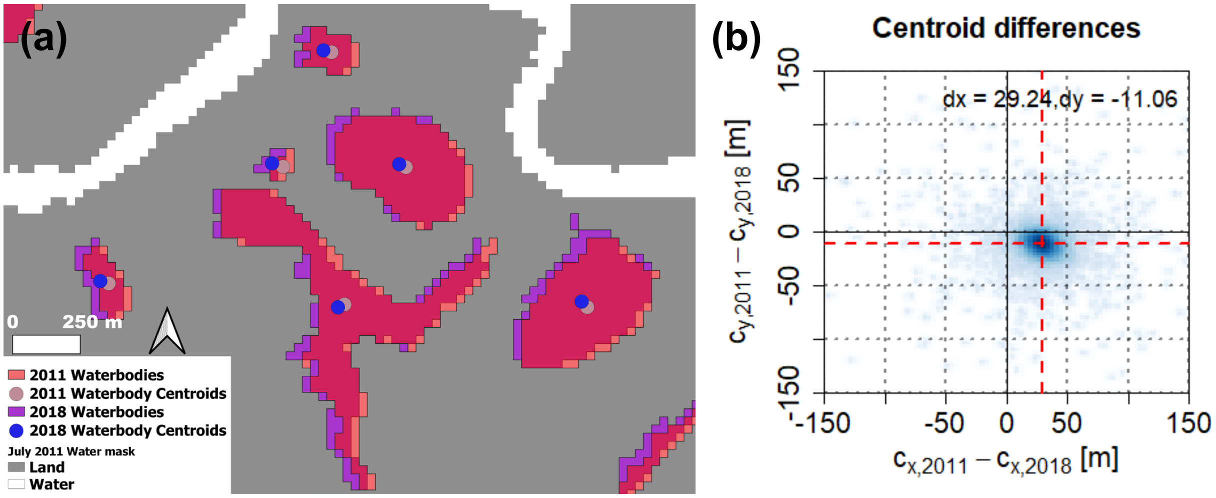

Figure C.1: **Collocation errors in the GSW dataset on the Yana delta.** (a) Waterbodies from 2011 (red) and 2018 (purple) overlaid over the July 2011 water mask, with a clear offset between the two. The corresponding waterbody centroids are shown in brown and blue, respectively. (b) The distribution of centroid differences is shown with the median difference in each direction given by the red dashed line.

error over the region and to correct the masks. Therefore, to estimate the magnitude of the miscollocation, we looked at the distribution of differences in waterbody centroids between different years, $(\Delta C_y, \Delta C_y)$. We found that the median of $(C_{x,2011} - C_{x,2018}, C_{y,2011} - C_{y,2018})$ was $(29.24, -11.06)$ m, i.e. the median centroid difference between the two masks was approximately one pixel in the horizontal direction and a third of a pixel in the vertical. By examining the whole distribution of differences in waterbody centroids, we quantified that over 88% percent of waterbodies in 2018 were shifted to the southwest relative to the position of the same waterbodies in 2011 (i.e. over 88% of the centroids lay within the lower right quadrant of Figure C.1b).

C.2 Hydrology of the deltas and choice of the year for waterbody mask extraction

To choose the reference year y^* in which to extract waterbody extents as objects and classify perennial lakes and ephemeral wetlands based on their year-to-year variability, we first computed for each delta and year the water cover, i.e. the fraction of valid (i.e. resolved as water or land) pixels that are classified as water over the subaerial delta, defining time series of July water cover from 1999 to 2018 (Figures C.2 and C.3). Then, we computed for each delta the average water cover over the period of record using the total number of valid pixels in each year as weights. Finally, y^* was chosen as the year with water cover closest to the average and at least 99% valid pixels. To test the robustness of the results, an alternative reference year, y^*_{alt} was also selected for each delta with a similar water cover to y^* and high data quality and the analysis repeated (Table S4 and Figures C.4 and C.5. To account for the heterogeneity in data quality across the range of analyzed systems, exceptions to these criteria had to be made for the Yukon, Lena, and Indigirka deltas. On the Yukon delta, the only two years satisfying the 99% valid pixel criterion were the 2008 and 2014, but these two are the wettest years on record, not years with typical hydrology. Therefore, 2017 and 2016 which had 98.7% and 98.9% valid pixels (slightly less than the 99% criterion), but close to average water cover were chosen as y^* and y^*_{alt}, respectively (Figure C.2). On the Lena and Indigirka deltas only 2013 and 2016, respectively, had at least 99% valid pixels for the period of record. To perform the replication analysis, we relaxed the 99% valid pixels criterion to identify an alternative reference year y^*_{alt}. We found that 2007 had 98.5% valid pixels over the Lena delta and 98.7% valid pixels over the Indigirka delta, and therefore chose 2007 as y^*_{alt} for both deltas.

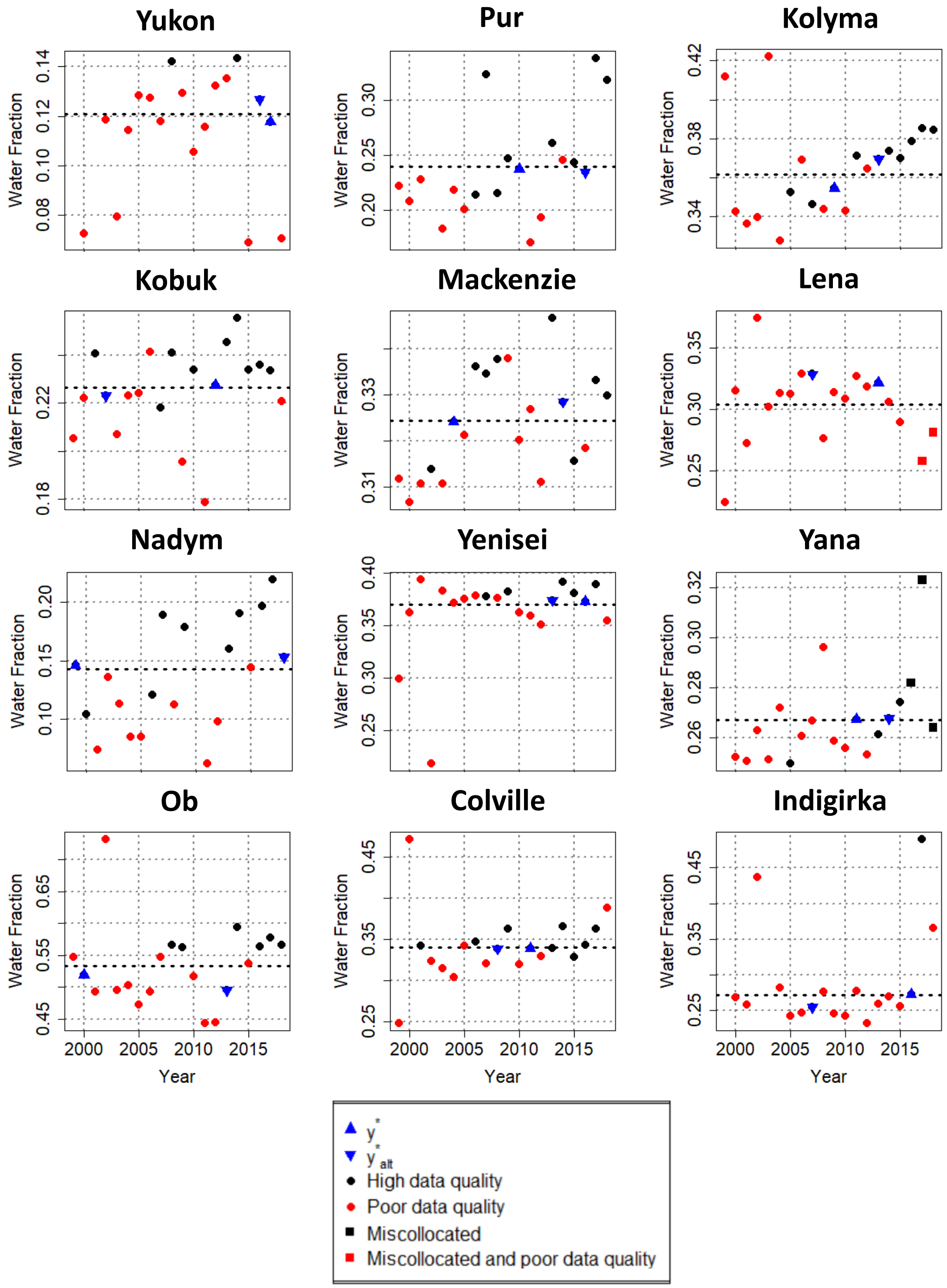

Figure C.2: **Surface water hydrology of arctic deltas.** Time series of July water cover for every delta from 1999 to 2018. Years with at least 99% valid pixels are marked in black and years with less than 99% valid pixels in red, while years chosen for waterbody extraction are in blue triangles. Miscollocated years are shown with squares. The time series of percent valid pixels for each delta is shown in Figure C.3.

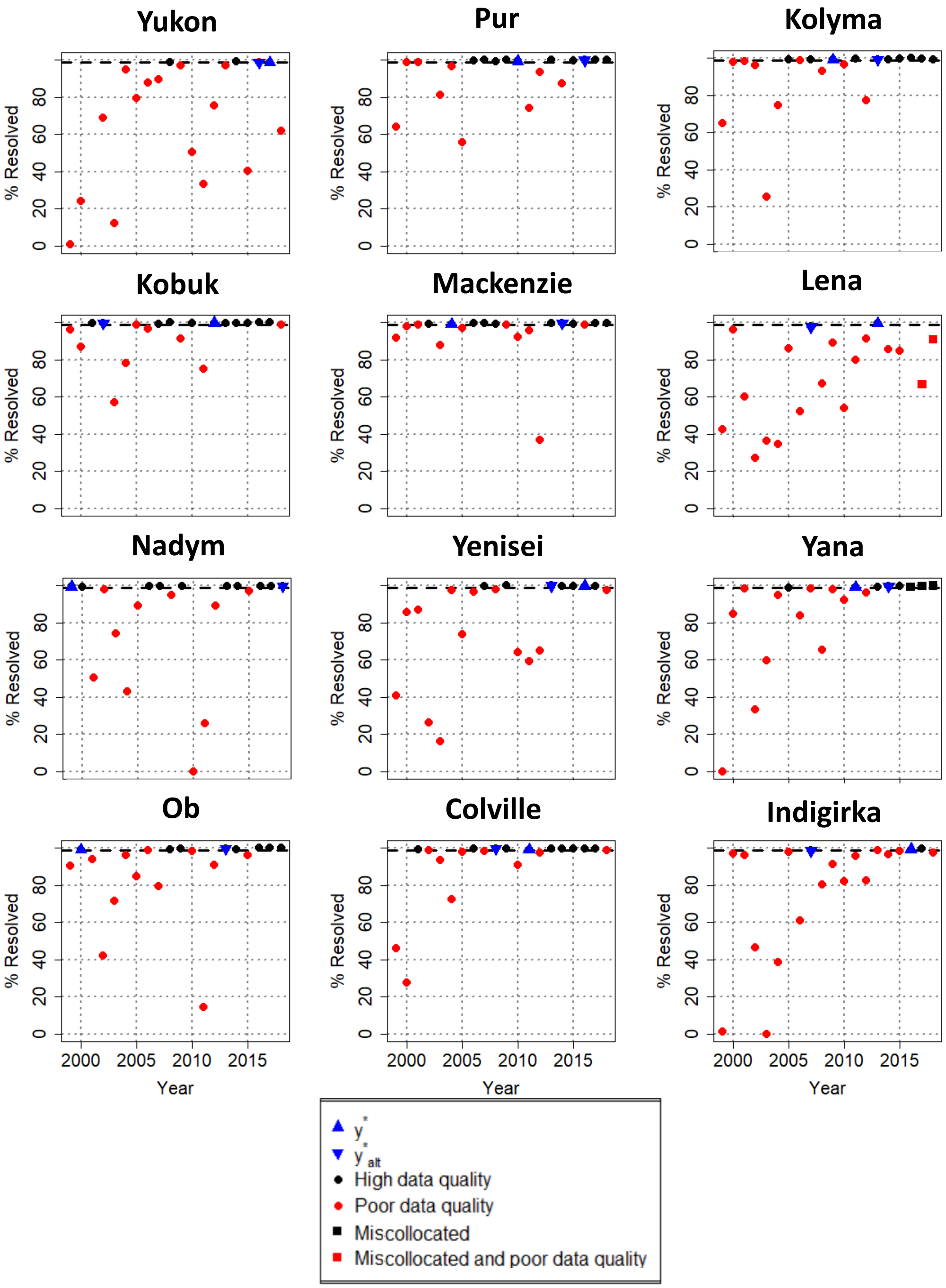

Figure C.3: **Observational data quality.** The percent of pixels resolved in every year on the period of record for the deltas, with symbology the same as in Figure C.2.

C.3 Proportionate Growth Model

Proportionate growth models, which describe processes where objects grow proportionally to their size with a stochastic growth rate, have seen widespread applications e.g. in modelling micro-organism sizes, income distribution, and city sizes (Crow & Shimizu, 1988; Mitzenmacher, 2004). An interesting property of the proportionate growth models is that they result in a lognormal distribution of the size of the objects, with the parameters related to the parameters of the stochastic growth rate. On the basis that the greater thermal inertia of larger lakes results in lake waters remaining unfrozen for longer and maintaining greater lake to soil temperature gradients, we assume that lake growth is proportional to the size of the lake, which has been observed in Alaska (Jones et al., 2011). Then for a lake with radius r_j at the beginning of a time period j of length Δt, its growth rate $\frac{\Delta r_j}{\Delta t}$ is given by Equation C.1.

$$\frac{\Delta r_j}{\Delta t} = r_j k_j. \tag{C.1}$$

We can assume that the growth rate k_j at each timestep is an independent and identically distributed random variable characterized by mean γ and variance φ^2, reflecting the variability in water and soil temperature, precipitation, and soil ice content and matrix properties all of which impact lateral heat fluxes. It is easy to show from Equation C.1 that the distribution of the lake radii after some time period t (arising as the sum of the initial lake radius and its subsequent incremental growths Δr_j over the cumulative period of time) will approach a lognormal distribution (Crow & Shimizu, 1988), i.e., $\ln r \sim N(\gamma t, \varphi^2 t)$ (see Equation 4.1 with no lower bound). Assuming a circular shape of the lake, it follows that $\ln A = \ln \pi r^2 \sim N(2\gamma t + \ln \pi, 4\varphi^2 t) = N(\nu, \beta^2)$, i.e. lake areas are also lognormally distributed with parameters, ν and β^2, and similarly for the volume. A similar model was proposed by (Victorov et al., 2019) for thermokarst lakes although empirical testing did not reveal ubiquity of the lognormal size distribution likely due to the mixing of lakes and wetlands in the studied domains.

C.4 Fitted distribution parameters and climate trends for lakes, wetlands, and waterbodies

This section contains tables and plots of the fitted distributions and climate trends for lakes, wetlands, and all waterbodies in the reference and alternative reference years. The fitted distribution parameters of lakes and wetlands for a range of waterbody occurrence index thresholds θused to classify waterbodies extracted in y^* are in Tables C.1, C.2, C.3, lake and wetland distribution properties for waterbodies extracted in an alternative reference year y^*_{alt} in Table C.4, the fitted lognormal distribution parameters for waterbody sizes extracted in y^* in Table C.5, the plots of fitted distributions and climate trends of lakes and wetlands extracted in y^*_{alt} (Figures C.4 and C.5), fitted distributions and climate trends of waterbody sizes extracted in y^* (Figure C.6) and boxplots of the waterbody, wetland, and lake size distributions extracted in y^* in Figure C.7.

Table C.1: **Properties of lake and wetland size distributions at occurrence index threshold $\theta = 0.85$.** For each delta, the fitted lognormal parameters ν and β, the number of lakes, N_{Lake}, the p-value (p_{lake}) from a Lilliefors-corrected Kolmogorov Smirnov test (KS test), and $\Delta AIC = AIC_{PL} - AIC_{LN}$ for the lakes, as well as the fitted power law exponent α, fitted minimum lake size x_0, observed maximum wetland size A_{max}, the number of wetlands $N_wetland$ in the range $[x_0, A_{max}]$, the p-value ($p_{Wetland}$) from a KS test, and the similarly defined ΔAIC for the wetlands. We report the parameters ν and β in $\log_{10}$ scale rather than in Napierian logarithmic scale (ln) as they are easier to interpret. The fitted distributions which cannot be rejected at the 5% significance level **($p > 0.05$) are bolded**.

Delta	N_{Lake}	ν [-]	β [-]	p_{Lake}	ΔAIC Lakes	$N_{wetland}$ (above x_0)	x_0 [10^5 m^2]	A_{max} [10^5 m^2]	α [-]	$p_{wetland}$	ΔAIC Wetlands
Yukon	1,511	3.87	0.80	**0.278**	187	401	0.135	2.835	2.55	**0.052**	5.44
Kobuk	1,272	4.40	0.82	**0.688**	328	196	0.09	3.924	2.30	**0.105**	2.88
Nadym	866	4.46	0.70	**0.404**	283	1,005	0.144	52.092	1.91	**0.143**	8.57
Ob	1,567	4.32	0.82	**0.843**	364	940	0.054	31.428	1.77	**0.306**	-1.69
Pur	2,407	4.24	0.75	0.008	537	556	0.117	21.411	1.81	**0.289**	0.48
Mackenzie	20,318	4.37	0.75	0.025	5,517	1,404	0.189	30.168	2.39	**0.636**	-1.70
Yenisei	4,058	4.62	0.60	0.038	2,099	1,028	0.153	10.620	2.47	0.049	6.72
Colville	338	4.57	0.79	**0.326**	111	105	0.162	7.731	2.30	**0.532**	-1.85
Kolyma	3,084	4.19	0.82	**0.283**	595	555	0.135	14.202	2.29	**0.576**	-2.01
Lena	11,265	4.49	0.74	0.008	,3674	1,353	0.477	27.783	2.63	**0.253**	-1.98
Yana	10,297	4.21	0.88	**0.403**	1,949	1,563	0.144	37.872	2.07	**0.511**	-0.77
Indigirka	4,875	3.91	1.08	**0.162**	593	1,830	0.099	42.930	1.91	**0.540**	0.96

Table C.2: **Properties of lake and wetland size distributions at occurrence index threshold $\theta = 0.80$.** Same as Table C.1 but with waterbody classification threshold $\theta = 0.80$. Bolded p-values refer to distributions which cannot be rejected at the 5% significance level.

Delta	N_{Lake}	ν [-]	β [-]	p_{Lake}	ΔAIC Lakes	$N_{wetland}$ (above x_0)	x_0 [10^5 m^2]	A_{max} [10^5 m^2]	α [-]	$p_{wetland}$	ΔAIC Wetlands
Yukon	1,829	3.80	0.79	b	205	252	0.126	1.863	2.74	**0.117**	-0.81
Kobuk	1,417	4.22	0.87	**0.663**	274	185	0.054	3.924	2.22	**0.709**	0.91
Nadym	1,311	4.31	0.73	**0.645**	328	1,452	0.063	42.876	1.89	0.019	10.61
Ob	1,773	4.17	0.88	**0.825**	318	734	0.054	21.483	1.82	**0.298**	-1.58
Pur	2,796	4.07	0.81	**0.168**	462	784	0.054	21.411	1.85	0.001	-1.88
Mackenzie	22,495	4.24	0.79	0.016	4816	1,019	0.153	19.620	2.37	**0.824**	-2.01
Yenisei	4,889	4.50	0.62	0.023	2001	765	0.126	9.090	2.65	**0.773**	-1.66
Colville	407	4.38	0.84	**0.215**	98	109	0.108	7.731	2.22	**0.720**	-1.99
Kolyma	3,613	3.98	0.87	**0.435**	508	692	0.072	14.202	2.31	**0.995**	-2.20
Lena	14,156	4.35	0.76	0.047	3644	637	0.540	19.008	2.63	**0.481**	-2.00
Yana	11,567	4.08	0.91	**0.756**	1827	2,015	0.072	12.789	2.10	**0.251**	-1.98
Indigirka	5,440	3.74	1.12	**0.062**	547	1,433	0.099	25.299	1.91	**0.879**	-0.70

Table C.3: **Properties of lake and wetland size distributions at occurrence index threshold** $\theta = 0.90$**.** Same as Table C.1 but with waterbody classification threshold $\theta = 0.90$. Bolded p-values refer to distributions which cannot be rejected at the 5% significance level.

Delta	N_{Lake}	ν [-]	β [-]	p_{Lake}	ΔAIC Lakes	$N_{wetland}$ (above x_0)	x_0 [10^5 m^2]	A_{max} [10^5 m^2]	α [-]	$p_{wetland}$	ΔAIC Wetlands
Yukon	1,118	3.95	0.81	**0.279**	152	185	0.369	15.993	2.69	**0.985**	-1.73
Kobuk	1,022	4.62	0.76	**0.827**	384	100	0.333	4.311	2.76	**0.597**	-2.00
Nadym	433	4.61	0.71	**0.395**	172	262	1.008	52.092	2.23	**0.610**	-0.15
Ob	1,275	4.50	0.75	**0.677**	410	1,232	0.054	43.704	1.75	**0.641**	2.14
Pur	1,753	4.47	0.69	0.025	600	1,356	0.081	23.697	1.85	**0.816**	2.13
Mackenzie	16,395	4.55	0.70	**0.091**	6,130	2,941	0.198	30.168	2.30	0.000	16.69
Yenisei	2,883	4.76	0.58	**0.625**	1,905	497	0.486	10.620	2.73	**0.281**	1.65
Colville	248	4.77	0.78	**0.382**	107	167	0.162	7.731	2.22	**0.255**	0.85
Kolyma	2,218	4.42	0.79	**0.730**	610	352	0.378	14.202	2.37	**0.946**	-1.91
Lena	7,438	4.67	0.73	0.000	3,151	2,369	0.495	27.783	2.43	**0.339**	6.64
Yana	8,286	4.34	0.86	0.016	1,884	2,806	0.144	37.872	1.96	0.000	34.68
Indigirka	3,973	4.06	1.08	**0.264**	564	1,113	0.270	73.431	1.93	**0.276**	1.19

Table C.4: **Properties of lake and wetland size distributions for waterbody extents identified in an alternative reference year.** Same as Table C.1 but for waterbody extent identified in an alternative reference year, y^*_{alt}, with close to average water cover, and using an occurrence index threshold $\theta = 0.85$. Bolded p-values refer to distributions which cannot be rejected at the 5% significance level.

Delta	N_{Lake}	ν [-]	β [-]	p_{Lake}	ΔAIC Lakes	$N_{wetland}$ (above x_0)	x_0 [10^5 m^2]	A_{max} [10^5 m^2]	α [-]	$p_{wetland}$	ΔAIC Wetlands
Yukon	1,340	3.90	0.81	**0.767**	171	961	0.081	3.357	2.10	0.003	36.06
Kobuk	1,421	4.28	0.83	**0.302**	305	196	0.054	2.025	2.25	**0.517**	2.13
Nadym	867	4.40	0.72	**0.396**	255	1,358	0.108	50.175	1.81	0.001	28.09
Ob	1,440	4.49	0.78	0.007	439	361	0.288	8.766	2.45	**0.238**	2.63
Pur	2,132	4.58	0.63	0.002	968	404	0.234	15.867	2.59	**0.106**	-1.03
Mackenzie	18,256	4.46	0.73	**0.080**	5,808	2,084	0.189	28.251	2.41	0.001	15.53
Yenisei	4,040	4.62	0.60	**0.072**	2,094	344	0.324	8.127	2.84	**0.385**	-0.80
Colville	441	4.25	0.88	**0.312**	86	140	0.072	2.934	2.20	**0.687**	-1.46
Kolyma	2,321	4.38	0.80	**0.511**	596	988	0.153	15.183	2.10	0.029	12.55
Lena	12,467	4.37	0.77	**0.059**	3,299	1,633	0.324	48.402	2.34	**0.360**	-1.99
Yana	10,145	4.31	0.84	**0.331**	2,267	2,011	0.126	16.470	2.21	**0.090**	7.12
Indigirka	5,892	3.90	1.05	**0.197**	714	866	0.117	23.193	2.31	**0.052**	-2.01

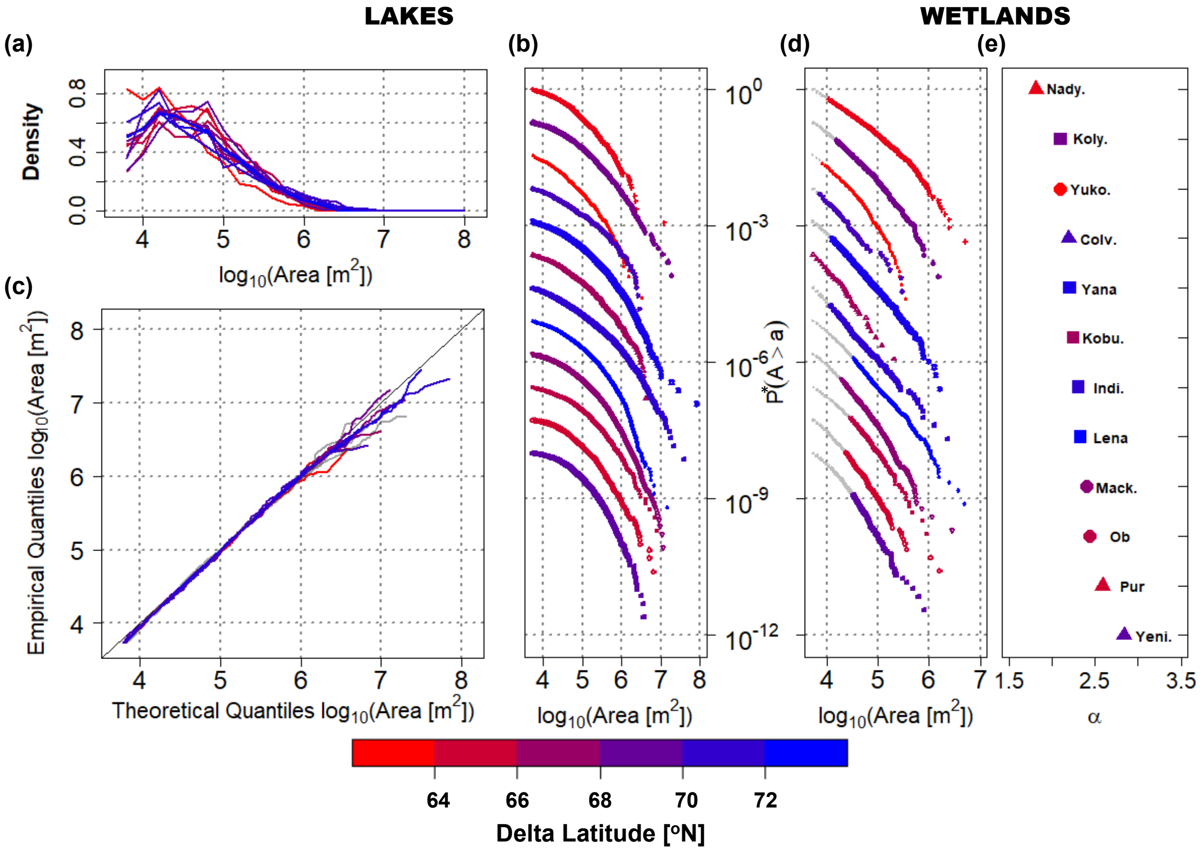

Figure C.4: **Lake and wetland size distributions extracted in an alternative reference year.** Same as Figure 3 but for waterbody extents identified in an alternative reference year, y^*_{alt}, for all 12 deltas. A truncated lognormal distribution is significant for the lake area distribution at the 5% significance level (KS test) for 10 deltas. The KS test does not reject a power law for the upper tails of the wetland size distributions in 8 out of 12 deltas at a 5% significance level.

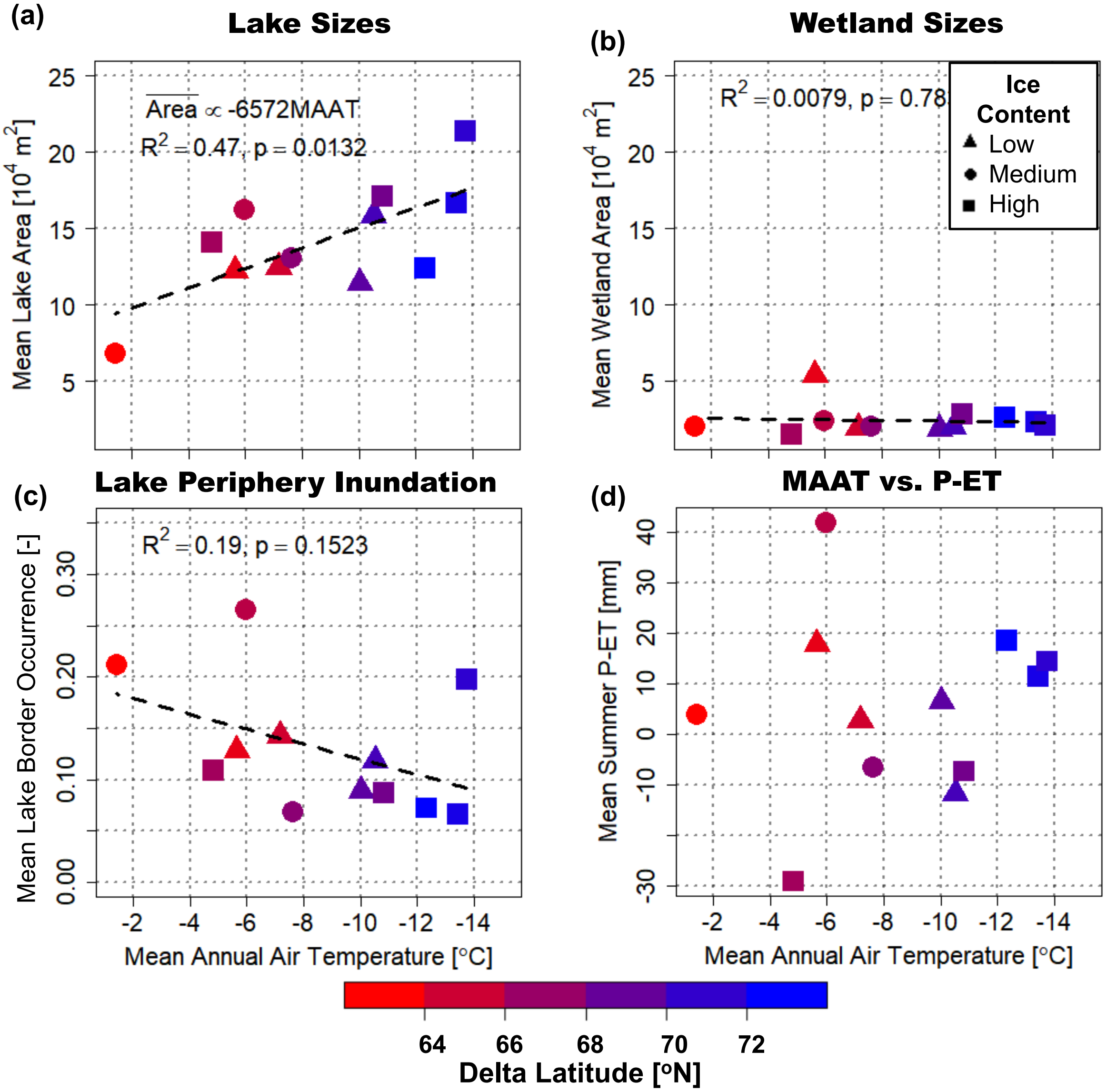

Figure C.5: **Climate trends for lakes and wetlands extracted in an alternative reference year.** (a-c) are the same as Figures 4.4a, 4.4b, and 4.4e, but for waterbody extents identified in an alternative reference year, y^*_{alt}, for all 12 deltas. In (a) the trend between MAAT and mean lake area has bootstrap $p = 0.0116$ and a Spearman rank correlation of -0.59 ($p = 0.0384$). In (c), the presence of two large outliers (Ob and Indigirka) renders the trend non-significant. Excluding them to evaluate the relationship among the rest of deltas yields a significant trend ($R^2 = 0.66$, p $= 0.005$), supporting a possible relationship. (d) Scatterplot of 2000 to 2016 mean June to July precipitation minus evapotranspiration ($P-ET$) over the deltas versus MAAT (Bromwich et al., 2018), indicating vertical hydrologic budget is unrelated to differences in MAAT ($R^2 = 0.013$) and therefore does not explain the relationship in (c) or in Figure 4e.

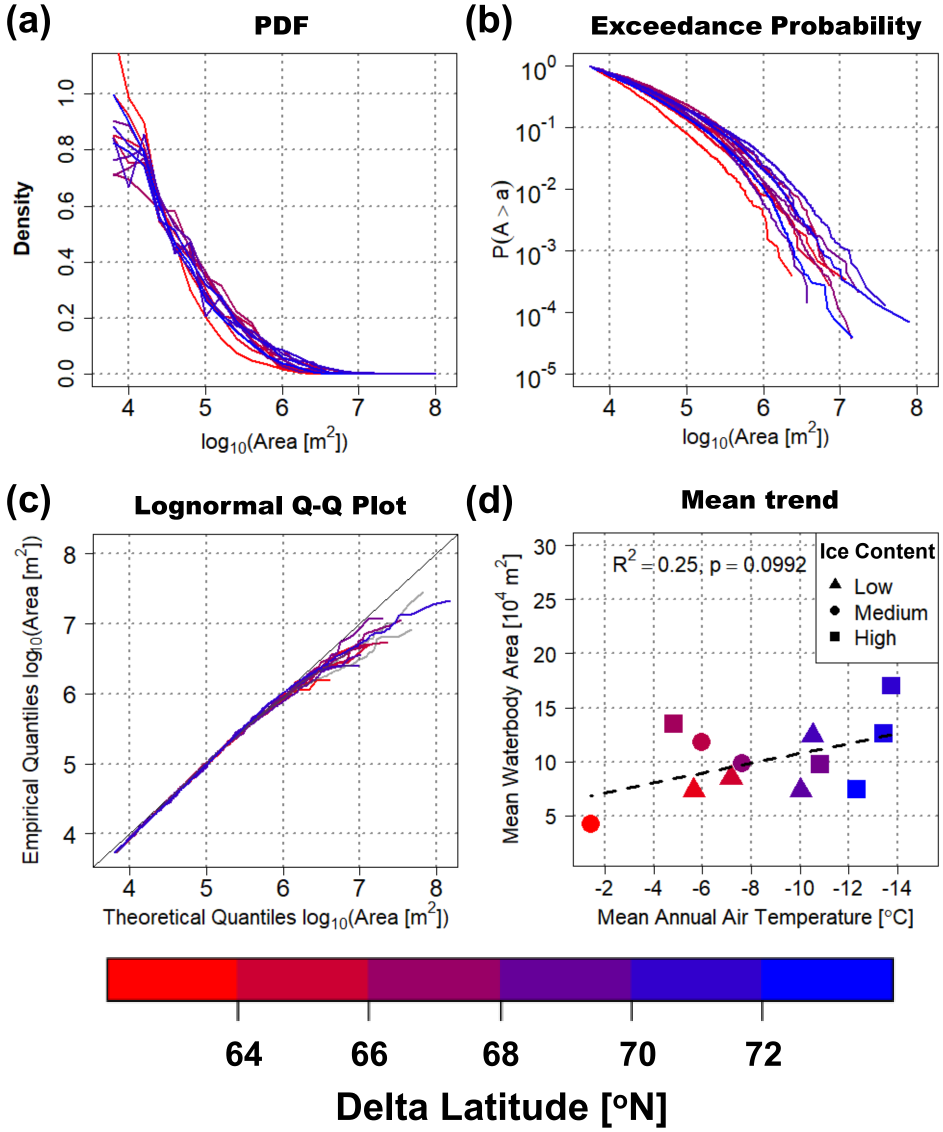

Figure C.6: **Waterbody size distributions and goodness of fit.** (a) The PDF and (b) exceedance probability curves of the waterbody (lake and wetlands combined) size distributions extracted in the reference year y^*, for all 12 deltas. (c) Q-Q plots of the lognormal distribution fit to the waterbody sizes, for all 12 deltas, with the fitted distributions which are not statistically significant at the 5% significance level (KS test) in grey. (d) Scatterplot of mean waterbody area and MAAT, with delta ice content indicated by point symbol, shows no statistically significant linear relationship between the two.

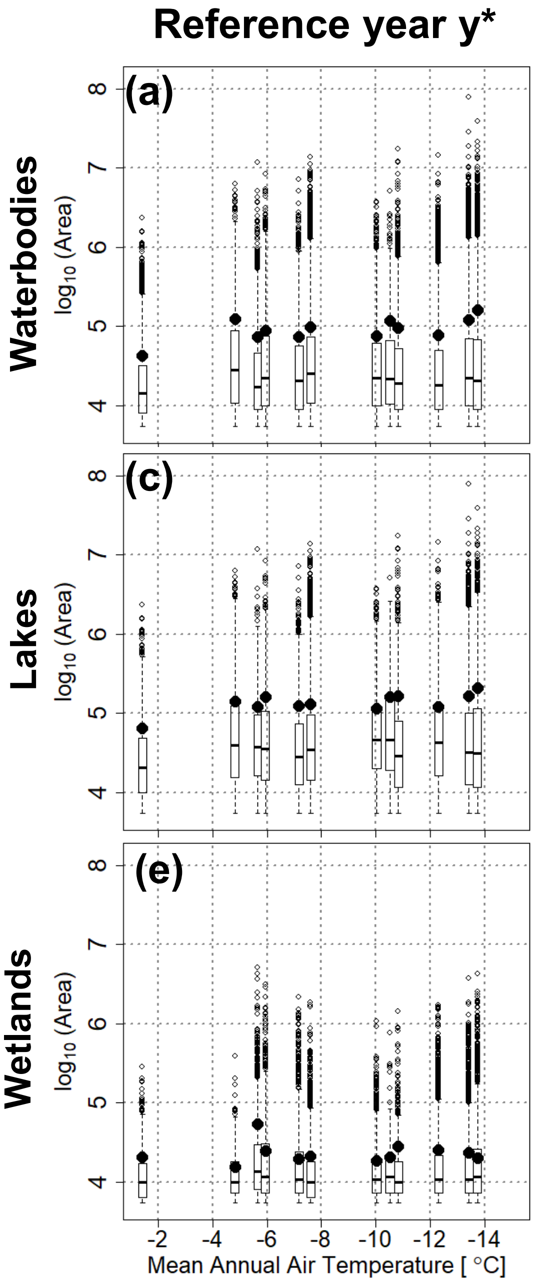

Figure C.7: **Waterbody, lake, and wetland size distribution boxplots.** (a-c) Boxplots of the size distribution for all waterbodies (a), lakes (b), and wetlands (c), with boxes representing the interquartile range, whiskers 1.5x the interquartile range, horizontal lines the sample median, and black dots the sample mean.

Table C.5: **Lognormal waterbody size distribution parameters.** Fitted lognormal parameters ν and β, for the waterbody size distribution in the reference year y^*, the number of waterbodies, $N_{waterbody}$, KS test p-values ($p_{waterbody}$) used to evaluate the goodness of fit, and the ΔAIC as defined above (see caption of Table C.1). Bolded p-values refer to distributions which cannot be rejected at the 5% significance level.

Delta	$N_{waterbody}$	ν [-]	β [-]	$p_{waterbody}$	ΔAIC Waterbodies
Yukon	2,610	2.97	0.97	**0.350**	103
Kobuk	1,602	3.92	0.97	**0.130**	201
Nadym	2,945	3.26	1.01	**0.417**	169
Ob	2,507	3.51	1.08	0.012	196
Pur	3,580	3.63	0.95	**0.251**	315
Mackenzie	25,995	3.96	0.88	0.000	3,543
Yenisei	6,981	3.97	0.81	0.005	991
Colville	606	3.50	1.09	**0.417**	45
Kolyma	4,557	3.35	1.04	**0.674**	296
Lena	25,604	3.20	1.06	0.000	1,421
Yana	14,283	3.53	1.06	0.000	1,151
Indigirka	7,807	2.70	1.36	0.043	319

C.5 Model identification for small samples of power-law distributed data

Although the hypothesis of a power law distribution for the wetland sizes could not be rejected in the majority of deltas (Tables C.1 to C.4), it is reasonable to ask whether the alternative hypothesis of a truncated lognormal (LN) distribution for wetland sizes could also be statistically acceptable, or even be a better fit in some cases for the wetland sizes. In principle, comparison of the fitted power law and LN distributions can be performed using the Akaike Information Criterion (AIC) test (Burnham & Anderson, 2004) or the likelihood ratio test (Clauset et al., 2009). However, the small sample size available for this testing (~ 200 to $2,000$ wetlands in our case) introduces challenges in robustly differentiating the power law distribution from the LN distribution. To gain quantitative insight into this problem, we performed a simulation of power law distributed data and used the AIC test to determine whether indeed the power law emerges as a better candidate distribution than the LN distribution. Specifically, we simulated synthetic power-law data using the procedure outlined in Clauset et al. (2009) with parameters $\alpha = 2.07$, $x_0 = 14,400$ m^2, and $N = 1,563$, i.e., the fitted parameters and sample length of the Yana wetland sizes extracted in y^* at a threshold of $\theta = 0.85$ (Table C.1) and repeated this exercise for a large number of simulations ($M = 1,000$). For each simulated data set i we used the same fitting procedures as for the observed wetland sizes, i.e., fitted a power-law distribution by estimating x_0^i and $\alpha^i$and then fitted a truncated lognormal with $x_{min} = x_0^i$ and estimating ν^i and β^i. We then computed the AIC difference $\Delta AIC^i = AIC_{PL}^i - AIC_{LN}^i$, where a positive ΔAIC^i indicates the lognormal is a better fit and a negative value indicates the power law is a better fit, and examined the PDF of ΔAIC^i over the $1,000$ simulations (Figure C.8a). We also examined the likelihood that the model rejected by the AIC test is a better candidate for the data by computing $\exp^{-} \frac{\Delta AIC^i}{2}$ (Figure C.8b; Burnham & Anderson (2004)).

The PDF of ΔAIC is centered at -2, indicating that the power law is a better fit overall, however this is not a large enough difference to reject the alternative hypothesis of the LN (Burnham & Anderson, 2004). Moreover, in approximately 9% of the cases ΔAIC is larger than zero, and therefore, the LN would be considered a better fit. It has also been shown that other statistical tests to compare competing hypotheses, such as the related likelihood ratio test, cannot distinguish between power-law and LN distributions for sample sizes below $2,000$ (Figure 6 in Clauset et al. (2009)). Based on these experiments, it is evident that we cannot solely rely on statistical tests to decide which distribution is better representing heavy-tailed data with sample sizes below $2,000$. Therefore, physical reasoning along with the interpretation of the fitted parameters are necessary to establish which distribution might be more suitable and interpretable for a given data set.

Looking back to the wetland size distributions which have statistically significant power law fits (Tables C.1 to C.4), $\Delta AIC = AIC_{PL} - AIC_{LN}$ tends to fall within the range of -2 to 2, which are values typically observed for truly power-law distributed data with the given sample sizes. Moreover, in other environments, wetlands identified by inundating rough topography show power-law slopes in a similar range (Le & Kumar, 2014; Bertassello et al., 2018) to what is reported herein (See Figure 4.3 and Tables C.1 to C.3), suggesting that ephemeral wetlands on arctic deltas may be governed by similar forming processes as wetlands elsewhere, giving rise to emergent power law size distributions. We also found that the parameters of the fitted LN distributions typically corresponded to $\nu \ll 0$ in the $\log_{10}$ scale and ended up fitting the data to a negligible (much smaller than 1%) fraction of the upper tail of an LN distribution. Therefore, we assert that the power law distribution is a more physically and statistically meaningful descriptor of the wetland size distribution compared with the LN. For completeness, we also tested the alternative hypothesis of a power law distribution with $x_0 = 5,400$ m^2 for the lake sizes (Tables C.1 to C.4) and waterbody sizes (Table C.5) and report the AIC test results with the same notation. We found that in all cases the LN distribution for lake sizes was a significantly better fit than a power law and therefore a better descriptor of the lake size distribution.

C.6 Relationships between the first three conditional moments of waterbody sizes

Muster et al. (2019) analyzed 30 regional size distributions of ponds and lakes from the circum-Arctic Permafrost Region Pond and Lake (PeRL) database, and found a linear relationship between the sample mean and the variance, and a hyperbolic relationship between the sample mean and the skewness coefficient of the empirical distributions when estimating these moments over a bounded range, e.g. a lower bound a and an upper bound b, also called the conditional sample moments. They also found that the statistical moments of waterbody sizes identified by inundating a digital elevation model exhibited similar relation-

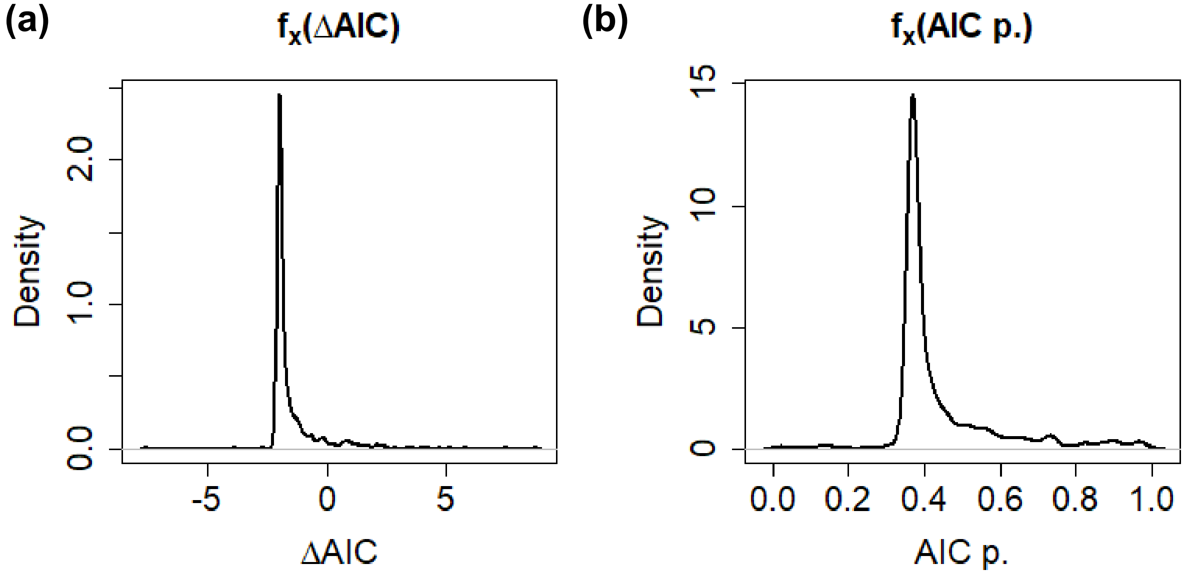

Figure C.8: **AIC test results to distinguish between power law and lognormal distributions fitted to simulated power law data.** (a, b) The probability distribution of $\Delta AIC^i = AIC^i_{PL} - AIC^i_{LN}$ for $1,000$ simulated power law distributions with $\alpha = 2.07$, $x_0 = 14,400\,\mathrm{m}^2$, and $N = 1,563$ (a) along with the likelihood, i.e. $\exp^{-\frac{\Delta AIC^i}{2}}$, that the model rejected by the AIC test is a better candidate for the data (b). Although the underlying data are truly power law distributed in every single case, both test statistic distributions are centered at values $\Delta AIC = -2, p = \exp^{-1}$ that preclude inferring that the data in all $1,000$ simulations are indeed power law distributed.

ships, and therefore determined that pond and lake sizes likely reflect landscape inundation level, rather than reflecting temperature driven growth due to climate. We compared the conditional sample moments of the 30 PeRL regional size distributions and the conditional moments of the fitted LN distributions to the lake sizes of the 12 arctic deltas to investigate if they displayed similar scaling relationships. In Muster et al. (2019) the bounds to compute the conditional sample moments used were $a = 100$ m^2, the minimum reliable lake size from PeRL, and $b = 10^6$ m^2 an upper bound to account for poor sample size for large lakes. We used for both the PeRL regions and the 12 deltas $a = 5.4 \cdot 10^3$ m^2, the minimum reliable lake size estimate in our study and $b = 10^6$ m^2, the same upper bound used in their study. As the relationships between the conditional sample moments computed from the fitted LN size distribution arising from proportionate growth are indistinguishable from the sample moments of the PeRL database (Figure C.9), we caution that such relationships cannot be used to differentiate between probability distributions and the different mechanisms underlying wetland (inundation) and lake (proportionate growth) formation.

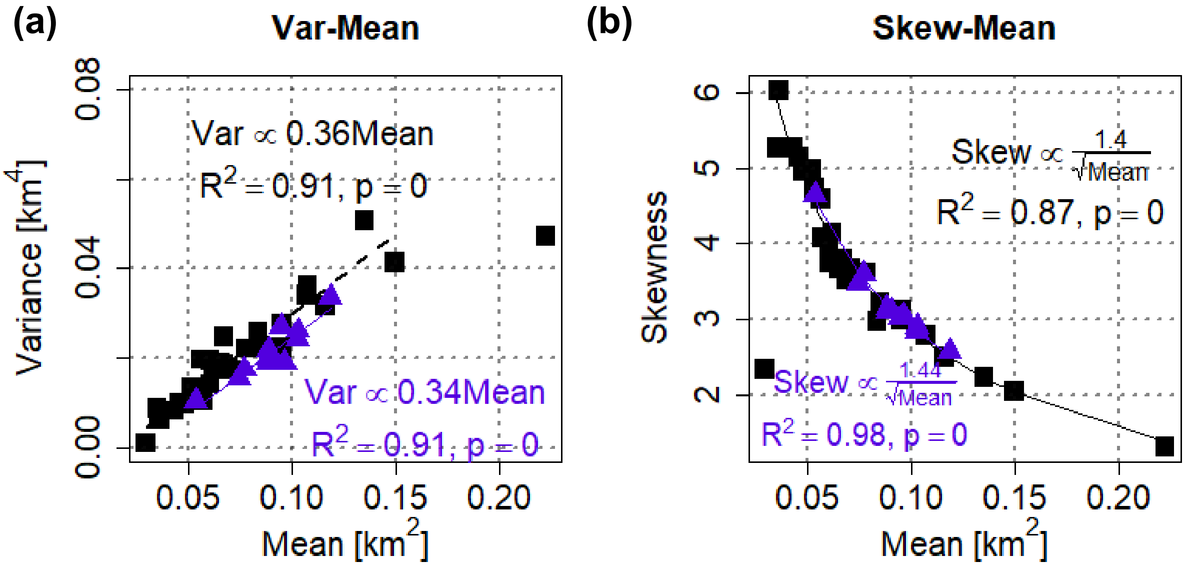

Figure C.9: **Lake size conditional moments of the fitted LN PDFs compared with PeRL lake and pond size sample conditional moment scaling relationships.** The conditional mean and conditional variance (a) and the conditional mean and the conditional skewness coefficient (b) of the lakes on our 12 arctic deltas (purple triangles) and lakes and ponds examined in Muster et al. (2019) (black squares). The outlier at (0.23 km^2, 0.05 km^4) was discarded to fit the mean and variance relationship (a) and the outlier at (0.01 km^2, 2.2) were discarded to fit the mean and skewness relationship (b) for the PeRL data.